Design of a magnetic coupling for reducing maintenance in long-term-autonomous bio-inspired underwater vehicles

Master Thesis

DELFT UNIVERSITY OF TECHNOLOGY

DEPARTMENT OF BIOMECHANICAL ENGINEERING

FACULTY MECHANICAL, MARITIME AND MATERIALS ENGINEERING

Author:
Steven KUIPERS

Supervisors:
Dr. Ir. Chris VERHOEVEN
Prof. Dr. Ir. Heike VALLERY
Ir. Tim VERCRUYSSEN

Abstract

Bio-inspired underwater vehicles are highly researched as a means for low-invasive monitoring. As a result, the performance of these vehicles has improved greatly. Research has thus far been directed towards the performances of the swimming motion. In order for the development of these bio-inspired underwater vehicles to continue, the increased reliability and durability should also be investigated.

This research is aimed at long-term-autonomous bio-inspired underwater vehicles, specifically vehicles based on Median/Paired Fin swimming, which could provide continuous, unassisted monitoring of an area. The goal is to investigate existing options for the propulsive mechanism and find the most suitable solution.

A suitable propulsive mechanism can cope with the pressure changes that the vehicle will face due to the varying depths while requiring no maintenance for extended periods of time. This expresses itself in a mechanism that has no dynamic contact between the internal mechanics of the vehicle and the external environment because the dynamic contact is prone to leakage.

One actuator and two transmissions are proposed as propulsive mechanisms in this research. The actuator is a reluctance actuator and the transmissions are a flexure joint and a magnetic coupling. The transmissions will be used in combination with an electric motor that is located inside the hull. The reluctance actuator has been found to lack torque generation. The flexure joint will be fused with both the hull and the fin and will be actuated from within the vehicle. It has the ability to either follow the large deflections that are required without encountering fatigue or to resist pressure differences, but both are required. The magnetic coupling does possess the torque, the range of motion, and the rigidity to resist the pressure, and is therefore chosen to be used as the propulsive mechanism that will be investigated further.

Existing designs of the magnetic coupling do not comply with the requirements of this swimming mode. Three types of designs are therefore proposed, the coaxial, the face-to-face, and the moment-arm design. To reduce the resultant noncontributing magnetic forces on the fin, the designs have been made symmetrical in the motion plane. To reduce the effect of unstable equilibriums that result from attractive forces on both sides, each type of design has a repulsive design as well as an attractive design. In addition, the designs have magnet orientations that are inspired by Halbach arrays to increase the magnetic field where desired and reduce it elsewhere. Simulations have been performed on the designs using the magnetic finite element method. These simulations indicated that the coaxial designs do not create enough coupling torque and the moment-arm designs create too much radial forces on the fin. The face-to-face coupling designs show promise, both in coupling torque and in resultant force directions.

Simulations of the double-sided, face-to-face coupling with Halbach-inspired magnet orientation have been validated and the results indicate that this new magnetic coupling could serve as a solution to reduce maintenance and increase reliability and durability in bio-inspired underwater vehicles. The use of repulsive forces in this design transfers the noncontributing resultant forces from occurring in the unpredictable external environment of the fin to the controlled internal environment of the vehicle.

Contents

Abbreviations

BCF Body/Caudal Fin

COT Cost Of Transport

emf electromotive force

mmf Magnetomotive Force

MPF Median/Paired Fin

RMSE Root Mean Square Error

ROV Remotely Operated Vehicle

UV Underwater Vehicle

Definitions

90-degree turn
Torque measurement of the face-to-face designs from peak torque to peak torque that covers 90^0.

Continuous hull
A hull without any dynamic contact for any cross-section.

Design
All proposed designs for the magnetic coupling including the attractive and the repulsive versions.

Design types
The three main working principles of the proposed designs for the magnetic coupling; coaxial, face-to-face, and moment arm.

Dynamic contact
Contact of two separate materials that are sliding past each other.

Field intensity
The strength of the magnetic field.

Flux
The magnitude of a magnetic field through a surface in the direction perpendicular to that surface.

Flux density
The magnitude of the magnetic field.

Halbach segment
Three magnets with one main magnet and two secondary magnets from which the internal parts of the face-to-face couplings are constructed.

Internal mechanics
All parts used for the propulsion and are located inside the vehicle.

Long-term-autonomous
Autonomy that does not require human intervention for months or years.

Main magnet
A magnet in a Halbach array or Halbach segment that is orientated outwards of the array or segment and from which the flux surfaces outwards.

Mechanics
Used in this report as the internal mechanics.

Mechanism
The combination of parts that are used to pass movement through the hull.

Mechanism type
The main working principles to pass movement through the hull.

Paramagnetic material
Material that is only magnetized in the presence of an external magnetic field in the direction of the magnetic field.

Secondary magnet
A magnet that is used to increase flux surfacing from the main magnets, these magnets are orientated in the direction of another magnet.

Section
A collection of data that is acquired in between the turn-direction change of the coupling.

Section types
Shows the difference in size, repulsive or attractive magnetic force use, and turning direction of the set-up.

Session
A collection of data that is acquired in between reassembly of the set-up.

Swimming mode
The basic principle that is used to create propulsion while swimming.

Test
A collection of data that is acquired using the same magnet position.

1 Introduction

Remotely Operated Vehicles (ROVs) are widely used for underwater inspections and observations. These vehicles are used to reduce both the danger and cost accompanying underwater exploration [10]. With the use of ROVs, the research on bio-inspired propulsion for Underwater Vehicles (UVs) has increased. Previous research has mainly been aimed at finding an alternative for the use of propellers on ROVs [14]. These UVs and ROVs are mostly controlled and maintained by humans, which increases the cost of operation. A technical solution for this would be to use autonomous vehicles which can be employed on a large scale, minimizing man-hours and periodical human intervention. This thesis will explore the possibility of creating a propulsion mechanism that allows a bio-inspired UV to be autonomous for long periods of time and the possibility of employing these vehicles using swarm robotics.

Swarm robotics uses a network of simple robots to create a combined intelligence. This allows for the robots in the swarm to be very basic, while the network of monitoring devices will increase the effectiveness of the total system [28]. The robots can be manufactured at low cost due to their simplicity, and the larger number of robots reduces the effect of small deviations that might result from environmental uncertainties on the monitoring results.

A long-term-autonomous UV will have different requirements compared to normal UVs. The difference lies in the required maintenance for continuously submerged vehicles. Regular resurfacing of current vehicles allows for drying the vehicles and cleaning or replacing seals for optimal functionality. This is not possible with the long-term-autonomous UVs due to their continuous submerged nature.

The design for long-term-autonomous UVs brings several difficulties and requirements for the propulsive mechanism. The first demand for obtaining long-term autonomy is eliminating the need for periodic maintenance, which involves taking a vehicle out of the water and out of service. A second requirement is continuous performance and robustness of the overall system while in service. The design should be pressure resistant, meaning that the system can work at various depths, and debris collection and marine growth should not limit its operation. For the vehicle to be commercially viable, the design should be energy efficient, ease of fabrication should be taken into account as well as the availability of technology that is used.

Previous literature research has determined that an electric motor is a suitable actuator choice [15]. One of the most important reasons for choosing the electric motor is its high reliability [21]. Optimization of this actuator for several decades has resulted in a high level of knowledge on the working principle and optimized design. In addition, the electric motor shows the best performance in existing bio-inspired UVs. This is likely the result of the electric-motor based bio-inspired UVs being designed to research swimming technique and efficiency, while the other actuators are used as proof of concept to show possible applications. Electric motors also have higher precision, resulting in a better swimming technique and performance [15]. From this research, it was concluded that the electric motor has the highest potential and is therefore selected for the design in this work.

The bio-inspired UVs, that are propelled using an electric motor, usually protect the internal electronics and the motor from the aquatic environment with dynamic seals dynamic seals (seals with dynamic contact). This is the conventional method to obstruct fluids from leaking into the vehicle, however, dynamic seals can only reduce the leaking to a minimum. Using dynamic seals, therefore, requires the choice to accept leaking or to force leaking in the desired direction [1]. This is an important reason for the need for maintenance in these vehicles. As long as an axle is connecting two separate compartments containing different fluids, one or both fluids will leak through the seal. For the long-term-autonomous vehicle, leaking in either direction is undesirable. Water leaking into the hull cannot escape and will create a damp environment, which is hazardous for the electric hardware. Forced leaking from the hull to the surroundings requires an actively varying pressure inside the hull to reduce the pressure difference over the seal. Additionally, forced leaking requires fluid to be leaked, which will have to be replenished over time. The use of dynamic seals in long-term-autonomous bio-inspired UVs is therefore not desirable. A more detailed description of dynamic seals can be found in Appendix A.

The solution in this case is to not use a dynamic seal but a continuous hull. A continuous hull is defined as a hull for which any cross-section of the vehicle shows a continuous hull without dynamic contact. With this, water ingress is eliminated completely making it the best option for long-term autonomous operations. Their application in long-term-autonomous bio-inspired UVs is mostly unexplored and is investigated in

this thesis. This is done by answering the following research question:

Research Question

How can a continuous hull be used to reduce maintenance and increase cycle life in long-term-autonomous bio-inspired underwater vehicles?

With a continuous hull defined as any cross-section of the vehicle shows a complete hull without dynamic contact.

The choice of swimming modes was based on literature research where different swimming modes were investigated [15]. The examined swimming modes were Body/Caudal Fin (BCF), Median/Paired Fin (MPF), Jellyfish, Flapping Foil, and Webbed Feet swimming. When dissecting the basic principles of the swimming modes, all biological modes can be reduced to an oscillating, pendulum-like motion. This means that when an actuation mechanism will work for one of these swimming modes, it could, with minor adaptations, be implemented for all swimming modes. A description of the swimming modes can be found in Appendix B.

Median/Paired Fin (MPF) swimming, which includes cuttlefish or ray motion, is selected because it allows for a steady, large platform to place mechanics, sensors, and batteries. The manoeuvrability of the MPF swimming mode is also higher than that of the other swimming modes. Additionally, expertise is present at the Delft University of Technology on the MPF swimming mode. A more detailed description of the swimming-mode selection can be found in Appendix B.

The aim of this thesis is to investigate the potential for a continuous hull in long-term-autonomous bio-inspired UVs, while keeping employment as swarm robotics in mind. The main objectives are to reduce maintenance and optimize durability.

This report will start with an overview of the research strategy in Chapter 2. An overview of literature and theory used as a basis in this research project is given in Chapters 3 and 4. Chapter 5 contains a parameter estimation for the magnets that are used in the magnetic coupling design. The magnetic coupling design selection is shown in Chapter 6. The validation set-up, method and results of the chosen design will be presented in Chapter 7 and 8, followed by the Discussion, Conclusion, and Appendix. The appendices contain background information on dynamic seals and swimming modes, explanations on the use of two propulsive mechanisms that are discarded beforehand, dimensions of the designs and test set-ups, Arduino code and connection diagram, and detailed results from the validation.

2 Research Strategy

This chapter gives an overview of the steps that will be made during the research.

2.1 Design Options

Figure 1 shows a block diagram of the powertrain of a swimming bio-inspired UV. This block diagram is used to find the different possible solutions as well as the different positions for the hull to cross the powertrain.

The power source and actuator will be an electric battery and electric motor respectively. The transmission transfers the motion of the actuator to the fin. The last block is the fin that is used for the propulsion.

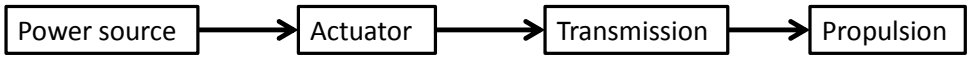

Figure 1: Block diagram of the powertrain of a bio-inspired UV.

A list of possible solutions for a continuous hull will be created. The hull position resulting from the solutions can be shown in the block diagram. This will give a clear view on how the solution is implemented in the design of the vehicle. It will also give an indication of the exposure of the mechanism to the environment. If the hull is positioned farther to the right in the block diagram the mechanism will be influenced less by the environment. The inside of the hull is a controlled environment, which suggest a lower chance of failure.

2.2 Objectives and Requirements

The objectives and requirements for the mechanism will be proposed. The *objectives* are a list of design criteria that are difficult to quantify, but are important for the vehicle to perform as a long-term-autonomous UV. The *requirements* are split into global requirements that consist of the requirements independent of the swimming mode and propulsive requirements that are dependent on the swimming mode. The global requirements will contain parameters like swimming depth and speed. The propulsive requirements will contain the motion defining parameters like torque, amplitude, frequency, and other propulsion specific requirements.

2.3 Mechanism Type Selection

The different types of mechanism that can be used to realize the oscillating motion while maintaining a continuous hull will be assessed. All mechanisms that will be assessed are electric motor based. Research will be done to find the strong and weak points of the different types of mechanisms and a general working principle will be quantified. The mechanisms will then be evaluated on their ability to perform the task by subjecting them to the objectives and the requirements from Chapter 3. The research will indicate a suitable mechanism type to be used in a long-term-autonomous bio-inspired UV.

2.4 Design Tests and Selection

The mechanism type that follows from the mechanism type selection will be used to create one or more designs. The designs will be assessed using the objectives and requirements. The chosen mechanism design will be validated using a method that will be defined when the design is chosen.

3 Objectives and Requirements

This chapter will determine the objectives and the requirements for the vehicle. The requirements are split into global and propulsive requirements.

3.1 Objectives

The objectives are used in the selection of the propulsive mechanism type. The propulsive mechanism types are the different mechanisms that will be used to create the propulsion of the fin.

Maintenance

The goal of the vehicle is to perform its tasks autonomously for long periods of time, which excludes maintenance acquired from humans. This means that there should not be a required monthly overhaul of the vehicles. The mechanism must be designed in a way that will not result in a fast degradation of the working mechanism.

Torque Production/Transference

The second important property that the mechanism should have is the amount of torque it can deliver. Without enough torque, the mechanism will be unable to actuate the swimming mode, resulting in low performance of the vehicle.

Robustness

The vehicle must be robust enough to survive for one year. This means that both the hull of the vehicle and the propulsive mechanism must be able to withstand minor impacts, and the chance of leaking as a result of an impact must be minimized.

Pressure Resistance

The vehicle is required to operate in various depths, meaning that it will dive and resurface multiple times. This will result in a highly variable external pressure acting on the hull and propulsive mechanism of the vehicle. The vehicle must be able to perform under all different external pressures.

Debris Collection

Debris collection must be kept to a minimum for the vehicle to perform optimal. Due to the lack of human intervention, debris removal will be difficult or impossible and build-up of debris could obstruct both fin motion and fluid dynamics. It is important to keep in mind that debris collection is only problematic when the debris is obstructing the vehicle to perform its tasks.

Ease of Fabrication

The new mechanism should be easy to produce. Highly complex designs will complicate fabrication and increase cost.

Energy Efficiency

The vehicle must be designed to be as efficient as possible, because a lower cost of transport will mean a larger radius of movement of the vehicle. Though this can be solved using larger batteries, this would still mean that the vehicle will not reach it's full potential.

Low Cost

The goal of this project is to find a suitable solution for a low price, to allow for larger swarms. Some of the vehicles might also disappear into the depths or get entangled. Recovery of a vehicle is a less urgent matter when the vehicle is low-cost and accompanied with multiple others to adopt its task. The result of this low cost objective is that the mechanism can not have a complicated mechanism for the propulsion, so this falls in line with a simplicity demand.

Availability

The working principle of the propulsive mechanism should be readily available and understood to reduce unknown parameters. Because this project is aimed at the propulsion mechanism, the propulsive mechanism should not complicate the design process.

Size and Weight

The size and weight of a vehicle are inseparable in a UV. The vehicle must be able to dive and resurface, meaning that the density of the vehicle has to be similar to that of the water. This means that if the size increases, the weight must also increase to correct the loss in density and vice versa.

3.2 Global Requirements

The global requirements are the requirements that are independent of the swimming mode of the vehicle.

The pressure that the vehicle must be able to resist is based on the depths of harbors. Since this is vehicle could be used to monitor harbors, the depth of the Port of Rotterdam is used for creating this requirement. The depth of the Eurogeul is maximum 26 m below NAP [6] and the depth of port of rotterdam has maximum 24 m [7], so the depth requirement is set to 30 m.

The life expectancy of the vehicle is the next requirement. This is set to one year with 3 hours of swimming per day. Assuming a swimming speed of 0.2 m/s (found to be representative of bio-inspired underwater vehicles [15]), this results in a 2 km swimming distance a day. Including diving and currents this will vary. The cycle life requirement of the mechanism will be derived from this using the frequency of the fin.

3.3 Propulsive Requirements

Next to the global requirements, the MPF propulsion results in extra requirements. Using the dimensions and data from the Galatea build within the TU Delft, requirements can be created for the mechanism.

Galatea Data

The fin rays, which are used to manipulate the fins of the Galatea (Fig. 2) make a sinusoidal motion. This is done using multiple fin rays that follow a sinusoidal pendulum motion perpendicular to the wave direction, with a phase difference between the separate fin rays. The requirements will be defined for one fin ray and will involve the amplitude, frequency, and torque.

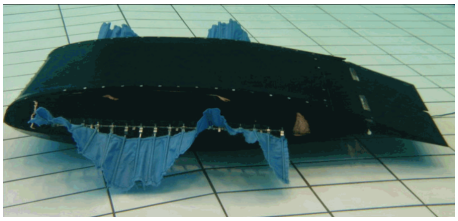

Figure 2: Galatea autonomous underwater vehicle [25] (with permission).

The amplitude and frequency is chosen by comparing the Cost Of Transport (COT), power use and swimming speed (Fig. 3). The COT is defined as

$$\mathrm{COT} = \frac{P}{m \cdot g \cdot U}, \tag{1}$$

with P the power use, m the mass, g the gravitational constant, and U the speed of the vehicle [31]. The wave length of the fin is chosen as 600 mm (k=1 in Figure 3) due to the higher swimming speed, and an

amplitude of 30° due to the lower COT and lower power use. The swimming speed is lower with a lower amplitude (approx 15 %), but the difference is less than the reduction in power (approx 30 %) (Fig. 3).

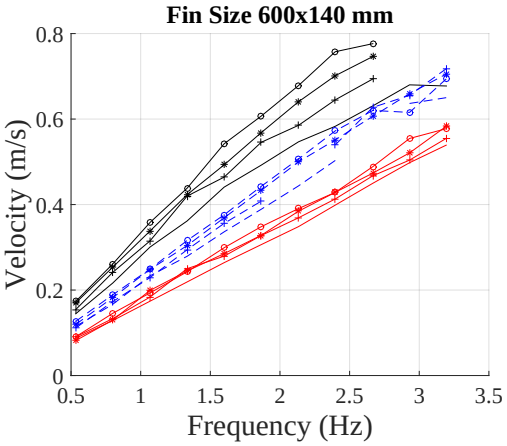

(a) Velocity as a function of frequency for different fin wavelengths and fin angle amplitude.

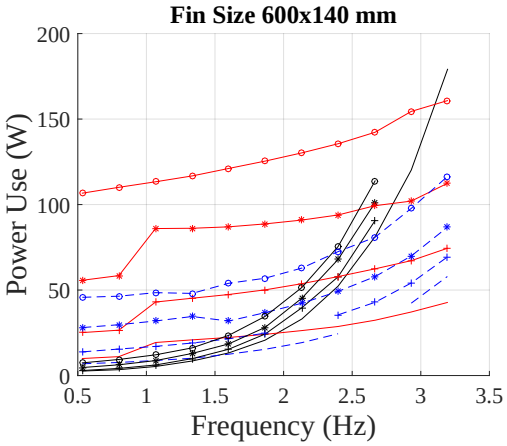

(b) Power use of whole fin as a function of frequency for different fin wavelengths and fin angle amplitude.

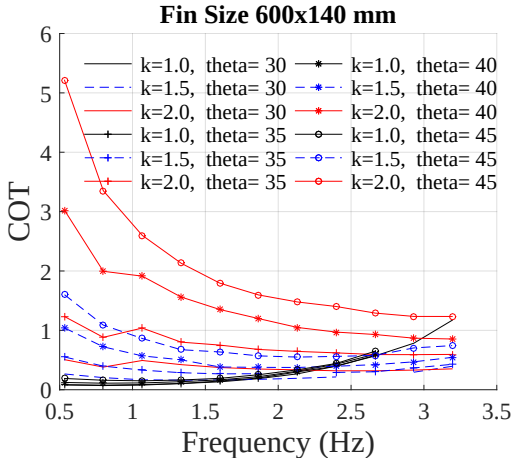

(c) Cost of transport as a function of frequency for different fin wavelengths and fin angle amplitude.

Figure 3: Data from the Galatea research [40]. Amplitude theta is measured as the angle from the neutral position. The value k is the wave number, wavelength of 300 mm on a fin with length 600 mm results in k=2.

A frequency of 2 Hz is chosen because that is the point after which the power use and COT increase drastically with respect to the other fin wavelengths. This results in a cycle life of the mechanism of around $7.9 \cdot 10^6$ cycles. This is rounded off to $1 \cdot 10^7$ cycles.

The distance between the fins is chosen to remain equal to that of the design of the Galatea, to assure the data is valid for this design.

To find the required torque of the fin rays, the power use of the different fin actuators with above mentioned swimming properties is used. An estimation of the required torque is created using the torque constant of the actuators [19], the efficiency of the gears, and the gear ratio [20]. Additional friction and possible back electromotive force (emf) are neglected. Both will increase power use, so the resulting requirements will be higher than the actual required torque. The torque production as a function of the fin ray angle can be found in Figure 4.

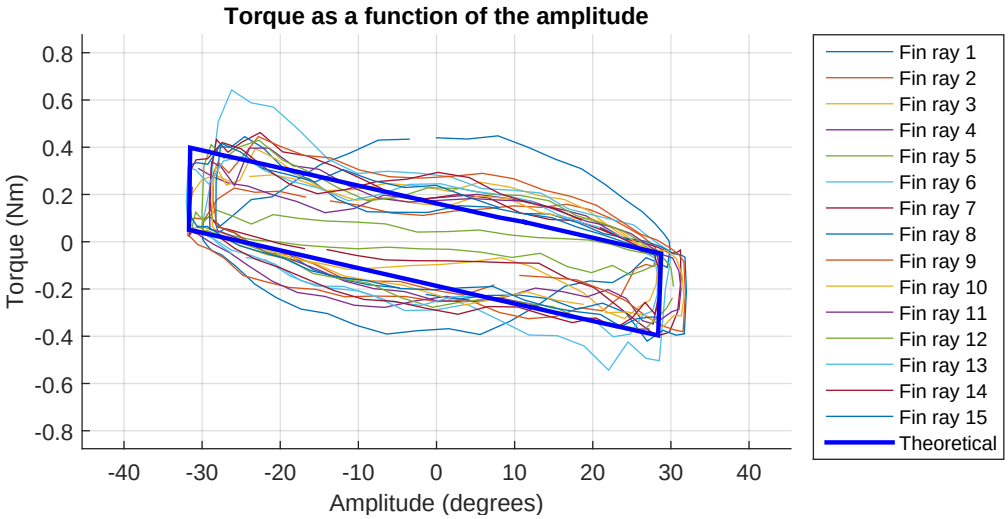

Figure 4: Torque during one full cycle of the separate fin rays of the Galatea during swimming, based on the data of the power use [40]. The direction of motion is clockwise, meaning positive force to move in positive amplitude direction. Fin 1 is the front fin ray and fin 15 is the rear fin ray.

In addition to the requirements, a maximum mass requirement will be added. As mentioned in Section 3.1 an increase in mass will create an increase in volume. A maximum volume for the propulsive mechanism will be set to 150 cm^3 which translates to 150 g to remain neutrally buoyant. This requirement will be valued the least since slight increases of the vehicle size will not reduce its performance significantly. The weight of the actuator and gear that is used in the Galatea robot is used to account for the difference when the propulsive mechanism does not require an actuator. This weight is 139 g.

All requirements are listed in Table 1.

	Requirements
Diving depth	30 m (3 bar)
Cycle life	$1 \cdot 10^7$ fin ray cycles
Torque	0.4 Nm (peak)
Amplitude	30° (neutral to peak)
Frequency	2 Hz
Wavelength of the fin	0.6 m
Distance between fin rays	30 mm
Maximum mass	150 g (289 g incl. actuator)

Table 1: All requirements for the mechanism.

These requirements will be used to select a mechanism type and later to select a final design.

4 Propulsive Mechanism Selection

This chapter investigates the application of a Reluctance Actuator and two transmissions, a Magnetic Coupling and a Flexure Joint, (Fig. 5) as propulsive mechanism. One mechanism will be selected based on the objectives and the requirements, the comparison can be found in the Discussion (Chapter 9). A short explanation on the use of soft hydraulics and stator-rotor design that are discarded beforehand can be found in Appendix C.

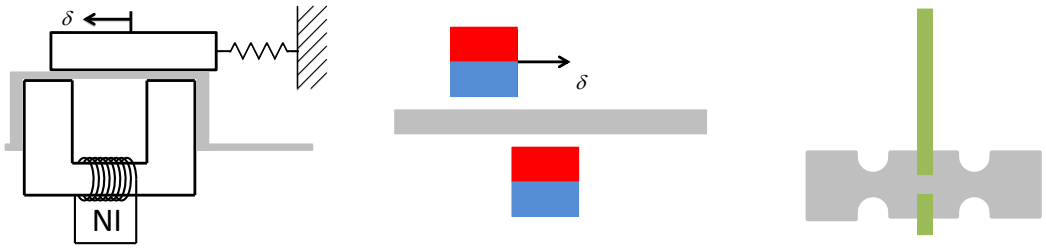

(a) Schematic representation of a reluctance actuator. If current runs through the electromagnet, the top bar will experience a force to the left.

(b) Schematic representation of the magnetic coupling solution. The external magnet will follow the actuated internal magnet.

(c) Schematic representation of the flexure joint solution. The compliant material of the flexure joint will follow the fin ray that is moved from the inside of the vehicle.

Figure 5: Simplified examples of the different mechanisms, the hull position is represented in gray.

4.1 Reluctance

The force of a reluctance actuator is the result of a reluctance difference due to the relative movement of the stator and rotor of the actuator [17] (Fig 5a).

4.1.1 Reluctance Properties

In order for a reluctance actuator to work, a gap is required, which would be ideal for the hull border to be inserted. The magnetizable material that is required to guide the magnetic field, can be used to support the hull to counter the pressure difference between the external and internal environment. This allows for a very thin hull.

The reluctance actuator does not require an additional electric motor. The weight of the additional electric motor and gear can therefore be subtracted of the total weight. This, however, also means that there is no possibility to create a main driving system that could reduce weight.

Because the reluctance actuator is directly connected to the fin ray, there are no losses caused by any transmission. In addition, the reluctance actuator can be easily controlled due to the electromagnet. By controlling the current through the coil, the generated forces can be regulated. Unfortunately, a standard reluctance actuator has only one direction in which forces can be generated. This means that for the oscillating fin ray a spring will be required [17].

The weakness of the reluctance actuator is the vulnerable external part of the mechanism. The spring that creates the reverse motion will be subjected to the environment. This will reduce the robustness of the propulsive mechanism. The small openings through which the mechanism will slide, will increase drag on the fin since water will be pushed through. The small openings could also result in obstruction to the fin ray due to debris entering.

The force that a reluctance actuator produces can be analytically estimated.

4.1.2 Analytical Force Estimation

Following the standard practice of reluctance actuators, the fin rays will be actuated in one direction using the reluctance actuator and the other way using a spring [17] (Fig. 5a). Assuming a linear rotational spring

that exerts a force of $0.0\,\mathrm{Nm}$ on one peak to $0.4\,\mathrm{Nm}$ at the other peak, the reluctance actuator should exert a constant torque of $0.4\,\mathrm{Nm}$ over the complete motion of the fin in order to create the position-torque found in the requirements (Section 3.3).

The force that a reluctance actuator generates is dependent on the *magnetomotive force* $\mathcal{F}$ and the change in reluctance $\mathcal{R}_\mathrm{t}$ of the total magnetic path [17]. The Magnetomotive Force (mmf) is used to quantify the strength of a magnetic field source. The force generated by a reluctance actuator is

$$F_\mathrm{r} = -\frac{\mathcal{F}^2}{\mathcal{R}_\mathrm{t}^2}\frac{\mathrm{d}\mathcal{R}_\mathrm{t}}{\mathrm{d}x}, \tag{2}$$

with F_r the force created by the reluctance, $\mathcal{F}$ the mmf, $\mathcal{R}_\mathrm{t}$ the reluctance of the total magnetic path, and x the distance traveled by the moving part of the reluctance actuator.

The reluctance of the gap is used for this estimation. For simplification it is assumed that the total reluctance of the actuator is equal to the reluctance of the gap, since the reluctance of the gap $\mathcal{R}_\mathrm{g}$ is much greater than the reluctance of the material $\mathcal{R}_\mathrm{m}$ ($\mathcal{R}_\mathrm{g} >> \mathcal{R}_\mathrm{m}$). The reluctance of the gap can be calculated using:

$$\mathcal{R}_\mathrm{g} = \frac{d_\mathrm{g}}{\mu_\mathrm{g} A_\mathrm{g}}, \tag{3}$$

with $\mathcal{R}_\mathrm{g}$ the reluctance of the gap, d_g the gap distance, μ_g the permeability of the gap, and A_g the surface of the gap.

These equations are used based on the assumption that the magnetic field will follow a straight path through the paramagnetic material following the path of lowest reluctance. In reality, the magnetic field will leak along the path that it is designed to follow, causing a lower actual force. The magnetic field will also not follow the a straight path through the gap, causing variations in the gap surface. These side effects are disregarded for this approximation.

The reluctance must be dependent on the fin ray angle θ_f. Without this dependency, the actuator would not create a force actuating the fin ray (Eq.(2)). For ease of control, the mmf will be constant, which means that the torque generated must be independent of the angle of the fin to create a constant torque of $0.4\,\mathrm{Nm}$.

The differential of the reluctance must have the same order of θ_f as the reluctance squared in order for the reluctance to be dependent and the force to be independent of the fin ray angle (Eq. (2)). If the gap of the actuator stays constant, the change in gap surface must be created in a way that the angle of the fin ray will disappear from the equation for the force (Eq. (2)). Assuming now that the surface is a function of some power n of fin ray angle θ_f: $A_\mathrm{g}(\theta_\mathrm{f}^n)$, the equation

$$\frac{1}{(\theta_\mathrm{f}^n)^2} = c\frac{\mathrm{d}}{\mathrm{d}\theta_\mathrm{f}}\left(\frac{1}{\theta_\mathrm{f}^n}\right) = c\left(-n\frac{1}{\theta_\mathrm{f}^{(n+1)}}\right) \tag{4}$$

must be solved for n with unknown constant c. Solving shows that $2n = n + 1$, so $n = 1$. Therefore the gap surface must have a linear relationship with the angle resulting in

$$A_\mathrm{g} = C\theta_\mathrm{f}, \tag{5}$$

where C is a constant depending on the design of the actuator and θ_f the fin ray angle. The reluctance of the gap therefore becomes

$$\mathcal{R}_\mathrm{g} = \frac{d_\mathrm{g}}{\mu_\mathrm{g} C\theta_\mathrm{f}}. \tag{6}$$

Applying this to Equation (2) results in the equation for the force production of the reluctance actuator:

$$F_\mathrm{r} = -\frac{\mathcal{F}^2}{\left(\frac{d_\mathrm{g}}{\mu_\mathrm{g} C\theta_\mathrm{f}}\right)^2}\frac{\mathrm{d}}{\mathrm{d}\theta}\left(\frac{d_\mathrm{g}}{\mu_\mathrm{g} C\theta_\mathrm{f}}\right), \tag{7}$$

$$F_\mathrm{r} = -\mathcal{F}^2\frac{\mu_\mathrm{g}^2 C^2\theta_\mathrm{f}^2}{d_\mathrm{g}^2}\left(-\frac{d_\mathrm{g}}{\mu_\mathrm{g} C\theta_\mathrm{f}^2}\right), \tag{8}$$

$$F_\mathrm{r} = \mathcal{F}^2\frac{\mu_\mathrm{g}}{d_\mathrm{g}}C. \tag{9}$$

Equation (9) shows the relationship between the reluctance force F_r, gap d_g, mmf $\mathcal{F}$, magnetic permeability of the gap μ_g, and parameter C. Parameter C is determined by the motion and design of the actuator. Note that the variable θ_f has disappeared from Equation (9), meaning the force is indeed independent of the fin ray angle.

4.1.3 Designs

Two designs are made that result in different constants C. The two choices are designing the moving surface *parallel* to the fin ray motion plane or *perpendicular* to the fin ray motion plane.

Parallel

The surface where the stationary and moving part of the reluctance actuator overlap will be the gap surface A_g. The function for the overlapping reluctance surface, $A_\mathrm{g} = C\theta_\mathrm{f}$, has high similarities with the function for the surface of a part circle under angle θ (Fig. 6a). In the case of the circle, the constant C is equal to $C = r^2/2$, where r is the radius. An obvious choice for the shape of the paramagnetic material connected to the fin will therefore be the shape of a part circle (Fig. 6b). In order to allow for an axle, an inner diameter is added, changing the surface of the reluctance to

$$A_\mathrm{g} = \frac{R_2^2 - R_1^2}{2}\theta_\mathrm{r} \tag{10}$$

Where θ_r is the angle of the overlapping moving part and the stationary part in radian, R_2 is the outer diameter of the reluctance surface and R_1 the inner diameter (Fig. 6b).

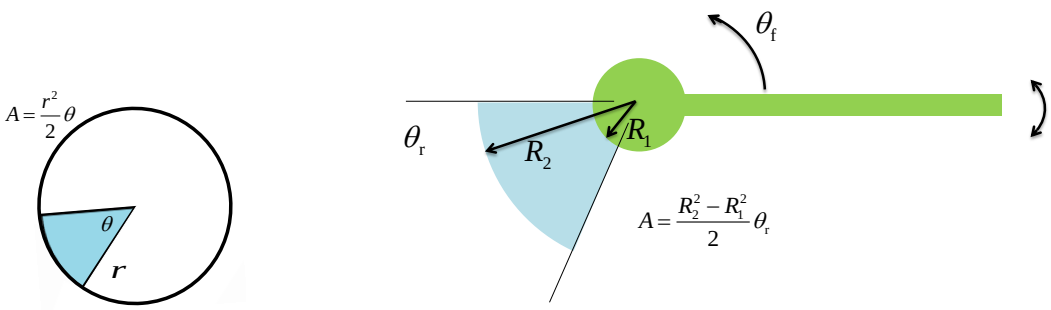

(a) Function for surface change of reluctance actuator is similar to surface of a part circle.

(b) Function for surface change of reluctance actuator is similar to surface of a part circle. Green represents the fin ray, blue represents the paramagnetic material.

Figure 6: Function for surface change of reluctance actuator is similar to surface of a part circle, which makes it an obvious choice.

On the inside of the hull, the electromagnet with two similar shaped parts are positioned on either side of the paramagnetic material of the fin (Fig. 7). When the electromagnet is activated a magnetic field is created in between these parts resulting in a force on the fin.

The double sided poles will reduce forces acting on the axle since there will be attractive forces on either side of the fin. Although this will create an unstable equilibrium, the forces are lower than when there would be a one-sided force. The reluctance will however also double, since there are now two gaps, resulting in half the force:

$$F_\mathrm{p} = \mathcal{F}^2 \frac{\mu_\mathrm{g}}{2d_\mathrm{g}} C, \tag{11}$$

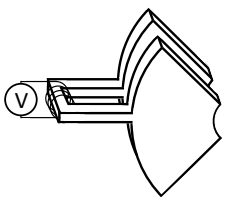

Figure 7: Stationary part of the parallel reluctance actuator that is positioned on the inside of the hull.

with F_p the force generated by the parallel reluctance actuator.

In order to create the torque τ_p that the parallel reluctance actuator produces, the function for the force must be integrated with respect to the radius:

$$\tau_\mathrm{p} = \int_{R_1}^{R_2} \frac{F_\mathrm{p}}{2}\,\mathrm{d}R \tag{12}$$

$$\tau_\mathrm{p} = \mathcal{F}^2 \frac{\mu_\mathrm{g}}{4d_\mathrm{g}} \int_{R_1}^{R_2} R^2 \mathrm{d}R \tag{13}$$

$$\tau_\mathrm{p} = \mathcal{F}^2 \frac{\mu_\mathrm{g}}{12d_\mathrm{g}} \left(R_2^3 - R_1^3\right). \tag{14}$$

The variable τ_p is the torque generated by the parallel design. The mmf is assumed to be constant.

Perpendicular

The perpendicular design will only use the outer radius of the rotational part of the actuator (Fig. 8). It is clear that the outer diameter R_2 of the parallel design has the highest impact on the torque of the reluctance (Eq. (14)). This is integrated into the design by using only the outside of the shape and extracting it to the side.

The perpendicular reluctance actuator has its changing surface perpendicular to the angular motion plane of the fin ray. The advantage of this is that all forces created by the actuator have an arm with the length of the outer diameter. This means that with the same amount of force, a larger torque can be created than when using the parallel reluctance actuator.

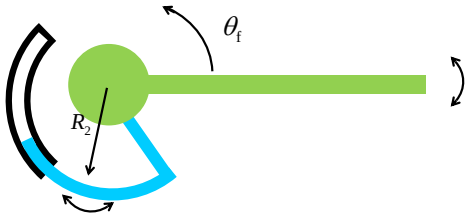

Figure 8: Schematic of the perpendicular style reluctance actuator, with green the fin ray, blue the paramagnetic material connected to the fin ray and black the magnetized paramagnetic material on the inside of the hull.

For the perpendicular actuator, C will become the radius R_2 of the fin-side moving reluctance part times the width w of the reluctance actuator. The torque will become the force times the radius of the moving reluctance part:

$$F_\mathrm{pe} = \mathcal{F}^2 \frac{\mu_\mathrm{g}}{2d_\mathrm{g}} w R_2, \tag{15}$$

$$\tau_\mathrm{pe} = \mathcal{F}^2 \frac{\mu_\mathrm{g}}{2d_\mathrm{g}} w R_2^2, \tag{16}$$

with F_pe the force generation of the perpendicular reluctance design and τ_pe the torque when using radius R_2.

4.1.4 Required magnetomotive force

Using the above Equations (14) and (16), it is possible to calculate a required mmf for the parallel and perpendicular design to be

$$\mathcal{F}_\mathrm{p} = \sqrt{\frac{12\tau}{\mu_\mathrm{g}} \frac{d_\mathrm{g}}{(R_2^3 - R_1^3)}}, \tag{17}$$

$$\mathcal{F}_\mathrm{pe} = \sqrt{\frac{\tau}{\mu_\mathrm{g} w} \frac{d_\mathrm{g}}{R_2^2}}, \tag{18}$$

with $\mathcal{F}_{\mathrm{p}}$ and $\mathcal{F}_{\mathrm{pe}}$ the required mmf for the parallel and the perpendicular design respectively.

In order to get an idea of the mmf that is required to actuate the fin rays, Equations (17) and (18) have been entered in Matlab. Both the gap size and the radius of the paramagnetic material influence the required mmf, so both have been entered as variables. For the perpendicular reluctance actuator, the width has been set at 2.0 cm, which means that the actuator has one centimeter clearance on each side to its neighboring actuator. The results are shown in Figure 9.

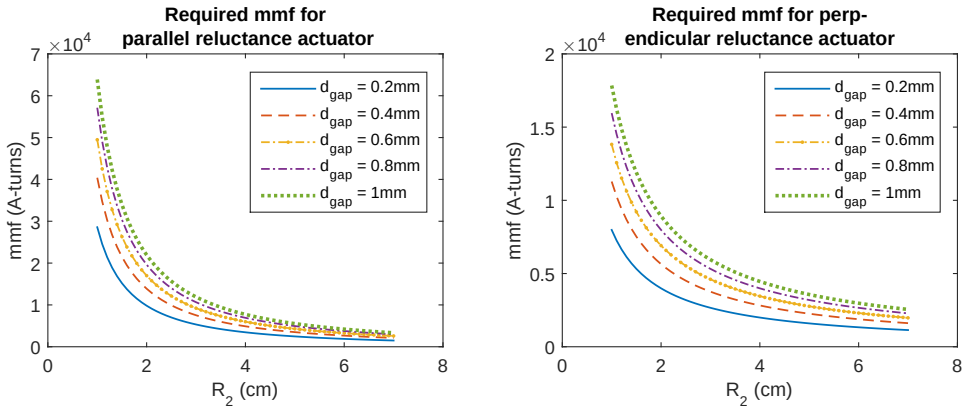

(a) Magnetomotive force as function of the radius R_2 for different gap sizes for the parallel reluctance actuator.

(b) Magnetomotive force as function of the radius R_2 for different gap sizes for the perpendicular reluctance actuator. Width of the actuator has been set at 2.0 cm to stay within the maximum set by the requirements.

Figure 9: Required mmf for both of the Reluctance actuator designs.

The mass of the paramagnetic material has been calculated for the different reluctance designs with an outer radius R_2 of 40 mm. The material that is used for this is Vacoflux 50, with a density of $8.12\,\mathrm{g/cm^3}$ [39]. This results in a mass of about 100 g for the parallel design and 50 g for the perpendicular design.

Forces in magnetic field direction

Because the paramagnetic material is positioned in a magnetic field, there are also forces acting on the material in the direction of the magnetic field. These forces will be in equilibrium when the mechanism is in the exact center, but this is an unstable equilibrium.

These forces are difficult to calculate without complex simulations. With the simplification that the magnetic field does not leak and follows the path of least reluctance, a deviation of the paramagnetic material from the center of the magnetic field would not change the reluctance of the total path. The reluctance decrease of one gap would be opposed by an equal reluctance increase of the other gap since the reluctance is linear with the gap. This means no force would be exerted on the fin in this direction. For now this force is neglected.

4.1.5 Coil Size

Figure 9 shows that the required mmf will be larger than 5000 A-turns. Assuming a wire can carry a maximum current density J_{m} without overheating and the actuator requires a certain $\mathcal{F}_{\mathrm{s}}$, the coil will need n turns. This means the wire will require a cross-sectional surface of

$$A_{\mathrm{w}} = \frac{\mathcal{F}_{\mathrm{s}}}{nJ_{\mathrm{m}}}, \tag{19}$$

with A_{w} the cross-sectional surface of the coil wire, J_{m} the maximum current density, and $\mathcal{F}_{\mathrm{s}}$ the mmf of the source. The resulting cross-sectional surface of the current carrying bundle will be

$$A_{\mathrm{c}} = A_{\mathrm{w}}\, n = \frac{\mathcal{F}_{\mathrm{s}}}{J_{\mathrm{m}}}, \tag{20}$$

with A_{c} the cross-sectional surface of the coil.

Taking the values as shown in Figure 9 of 5000 A-turns and $5\,\mathrm{A}/\mathrm{mm}^2$ as maximum current density [4], the cross sectional surface of the coil bundle will be $1000\,\mathrm{mm}^2$, not including the fill factor of the coil. Assuming a circular coil with length 100 mm results in a mass of 400 to 500 g per coil.

The coil that will be required for this type of actuation is too large and has too much mass to be applied. Though the weight of the actuator and gears that are required for the transmissions are saved, the mass is still double the requirements while assuming perfect conditions. The reluctance actuator is therefore not a possible solution and is rejected. A more detailed justification can be found in the discussion.

4.1.6 Summary

Reluctance actuators generate force using the change in reluctance of the path that the magnetic field follows. Using paramagnetic material the path can be directed. Since the magnetic field will mainly follow the path of least reluctance, a force will be created on the paramagnetic material that reduces the reluctance. An electromagnet is the source of the magnetic field.

Two designs of the reluctance actuator are proposed, a parallel and perpendicular reluctance actuator. For both designs a function is created that estimates the force based on the geometry of the actuator and the mmf from the actuator.

Using the force functions an estimate of the required mmf is made for different radii and gaps between the internal and external part of the mechanism. These estimates result in a minimum required mmf of 5000 A-turns. This translate to a coil bundle with a cross sectional surface of $1000\,\mathrm{mm}^2$ and a mass of 400 to 500 g to ensure continuous operation without overheating.The resulting mechanism is too large and heavy to be used as a propulsive mechanism.

4.2 Magnetic Coupling

Magnetic couplings use permanent magnets to transfer a force through a material (Fig. 5b). Since the coupling is only a transmission, it requires an electric motor inside the hull for actuation.

4.2.1 Magnetic Coupling Properties

The use of permanent magnets means that the coupling does not require a power source. The magnetic field that the magnets produce is also much stronger than that of an electromagnet of similar size. Since the magnets have no contact, there is no added friction in the mechanism due to the coupling and no wear of the mechanism [3, 32]. The connection between the coupling and the electric motor will cause energy loss.

Another useful property of magnetic couplings is their maximum torque [3]. If the movement of a finray is obstructed, the coupling will disconnect without damaging the internal mechanics of the vehicle.

The problem with this type of mechanism is that the mechanism is large due to the size of the magnets or the radius that the magnets require to generate enough torque. The low mechanism size that the vehicle requires could create difficulty.

The magnetic coupling can be actuated by using an inner permanent magnet that either oscillates or continuous full rotations. When using an oscillating inner magnet, both up and down movement can be actuated, but this could reduce the efficiency of the actuation due to back emf in the actuator [26]. If a rotating inner magnet is used, a magnetic actuation would actuate one direction while a spring would actuate the other direction, similar to the reluctance actuator. The actuator that excites the magnet can rotate continuously, increasing the efficiency of the system. For both systems the magnet must be able to create a torque of 0.4 Nm.

4.2.2 Magnetic Force

The force calculation on the permanent magnet is done similar to the electromagnet. The source of the magnetic field is the permanent magnet from which the mmf can be calculated using [17]

$$\mathcal{F}_{\mathrm{pm}} = \frac{B_{\mathrm{r}}}{\mu_{\mathrm{pm}}} l_{\mathrm{pm}}, \tag{21}$$

with $\mathcal{F}_{\mathrm{pm}}$ the mmf produced by the permanent magnet, B_{r} the magnetic remanence, μ_{pm} the magnetic permeability of the permanent magnet, and l_{pm} the length of the permanent magnet in the direction of the poles.

The force calculations will use the same equations as used for the reluctance actuator (Eq. 2) and (3). The gap surface A_{g} will be dependent on the design of the mechanism. These calculations are again based on the assumption that all field lines will follow a straight path through the paramagnetic material following the path of lowest reluctance.

4.2.3 Simple Design

To see whether the use of magnetic coupling is possible a simple design is created, shown in Figure 10a. The side with the magnet can rotate continuously or oscillatory and has an arm of R_{a} with a gap s_{a}. A cylinder of paramagnetic material with radius r at a distance R_{p} from the fin ray axle will create the reduction in reluctance needed for the force creation.

The reluctance will be differentiated to the change in gap surface. This gap surface will be the part of the circle that overlaps the arms of the driving part (Fig. 10b). A circle is chosen so the angle that the inner and outer part make with each other is not influencing the overlapping surface. The surface of the circle still in the magnetic field will be

$$A_{\mathrm{g}} = \pi r^2 - r^2 \cos^{-1}\left(\frac{r-h}{r}\right) + (r-h)\sqrt{2rh - h^2}, \tag{22}$$

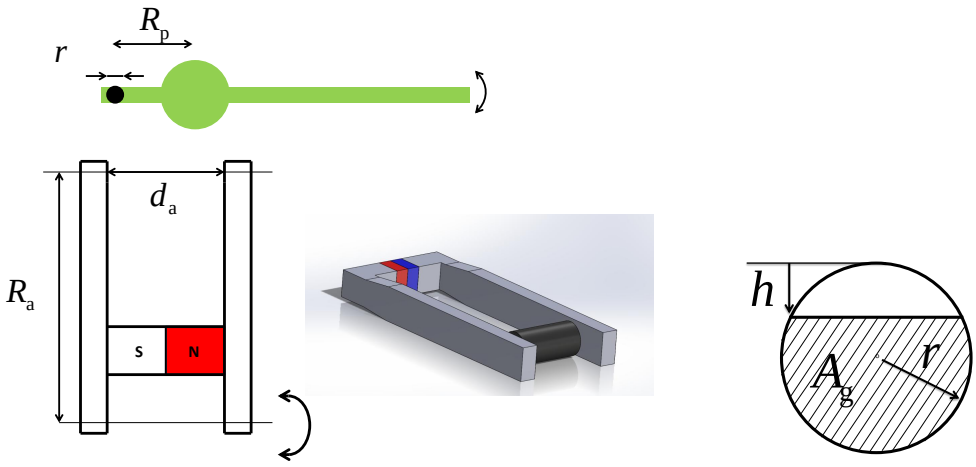

(a) Simple magnetic coupling design. Dimensions can be found in Appendix D.1.

(b) Surface of the overlapping paramagnetic material in the mechanism.

Figure 10: Schematic representation of the simple magnetic coupling design.

with A_g the gap surface, h the height of the paramagnetic material in the fin ray that does not overlap, and r the radius of the reluctance material in the fin ray. Since the reluctance surface is dependent on the height h, the derivative of the reluctance will be

$$\frac{\mathrm{d}\mathcal{R}}{\mathrm{d}h} = \frac{\mathrm{d}\mathcal{R}}{\mathrm{d}A_g}\frac{\mathrm{d}A_g}{\mathrm{d}h}, \tag{23}$$

with

$$\frac{\mathrm{d}\mathcal{R}}{\mathrm{d}h} = -\frac{d_g}{\mu A_g^2}\frac{\mathrm{d}A_g}{\mathrm{d}h}, \tag{24}$$

$$\frac{\mathrm{d}A_g}{\mathrm{d}h} = \frac{-r}{\sqrt{1-\left(\frac{r-h}{r}\right)^2}} + \frac{(r-h)^2}{\sqrt{2rh-h^2}} - \sqrt{2rh-h^2}. \tag{25}$$

The torques are calculated with Matlab and shown in the graph in Figure 11. For these calculations a cubic neodymium magnet with sides of 4 mm is used with a magnetic remanence of 1.32 T [34]. This results in an mmf of 7576 A-turns. To calculate the torque on the fin ray, an arm of 30 mm is used. The paramagnetic cylinder in the fin ray has a radius of 5 mm.

The forces in the flux direction are not taken into account due to the assumption that the field lines follow a straight path. These forces can be calculated using simulation programs like ANSYS or FEMM.

The simulation shows that the torque of the magnetic coupling is 10 % of the required torque. This torque can, however, be increased using more magnets. As Equation (21) shows is the mmf of a permanent magnet increased by increasing the length of the magnet. Another possibility of increasing the torque is with the use of Halbach arrays.

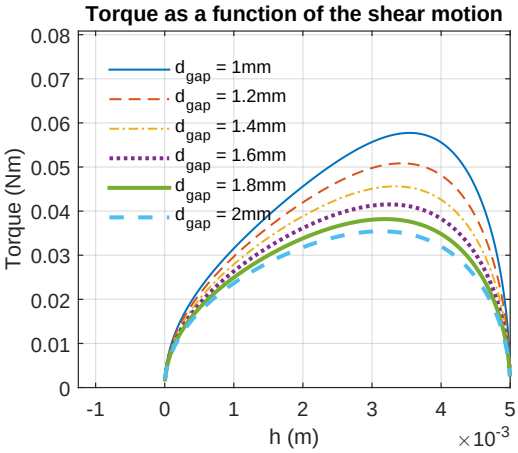

Figure 11: Disconnection torque of the fin for the magnetic coupling mechanism as shown in Figure 10a, calculated using Matlab. The arm of the paramagnetic material in the fin ray R_{p} = 30 mm from the external axle.

4.2.4 Halbach Array

Halbach arrays can be used to increase the field strength of permanent magnets. This increase is one-sided and can create a magnetic field that is 1.4 times [38] stronger and reaches farther than a normal up-down alternating magnet array . It can therefore increase the effective distance of the gap between the coupling. The magnetic field of magnets normally do not extend far from the magnet and the field strength reduces quickly with distance. Since the coupling has to bridge a relatively large gap (including the hull), an extended magnetic field will be required to increase torque.

A Halbach array is an array of magnets, orientated to guide the magnetic field. By orientating the poles of the magnets as shown by the arrows in Figure 12, the field strength on one side of the array is drastically increased and on the other side reduced. This also results in an increased reach of the magnetic field [9, 38, 42] (Fig.12). Two orientation types will be defined here, the *main magnets* shown in black (②, ④, ⑥, ⑧) and the *secondary magnets* shown in gray (①, ③, ⑤, ⑦). The main magnets are the magnets from which the flux extends out of the array, the vertically positioned magnets in Figure 12. The flux from main magnets is guided by the secondary magnets, the horizontally positioned in Figure 12.

The secondary magnets channel or reinforce the flux coming from the main magnets, depending on the side of the array. On one side of the array (lower side in Figure 12) the main and secondary poles that are touching have opposite poles. On this side the magnetic field from the main magnets is channeled through the secondary magnets. This results in a reduced magnetic field outside of the array (weak side). On the other side (upper side in Figure 12) the main and secondary poles that are touching have like poles. On this side the magnetic field from the main magnets is funneled together outwards by the secondary magnets. This results in an increased flux outside of the array (strong side).

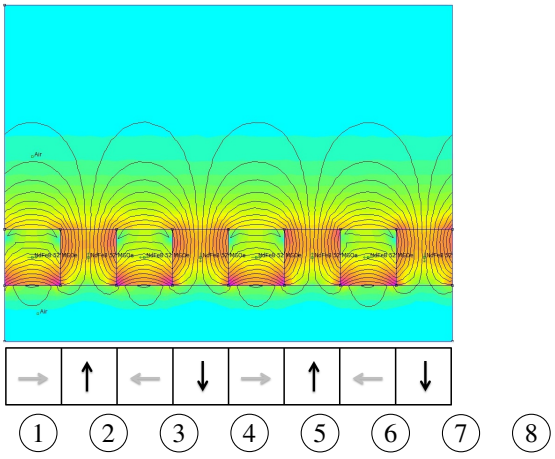

Figure 12: Magnetic field lines in a Halbach array [36](adapted, free to share). The blocks below show the orientation of the magnetic poles in the separate magnets. The poles of the main magnets is shown in black, the poles of the secondary magnets is shown in gray.

The opposing poles on the strong side of the array could create a difficulty for assembly of the array. The natural position of the secondary magnets is towards the weak side since the magnets oppose each other on the strong side. This means that for an effective Halbach array, the magnets have to be forced in position.

The use of Halbach arrays can increase the strength and the reach of the magnetic field enough to create a strong coupling. The magnetic coupling is therefore seen as a possibility to be used as a propulsive mechanism.

4.2.5 Summary

Magnetic couplings use the attractive forces of magnets to create a connection between two parts without a physical connection. This allows magnetic couplings to be used through other material or to reduce friction.

The generated force of a magnetic coupling can be estimated similar to that of the reluctance actuator. The difference is the source of the magnetic field, which is a permanent magnet. The mmf that is created using a permanent magnet is dependent on the material and the size of the magnet.

A simple design is created that holds a magnet in the internal part of the coupling and a cylinder of paramagnetic material in the external part of the coupling. The torque that is generated is estimated for different gap sizes between the internal and external part of the coupling.

The use of Halbach arrays could increase torque transfer. A Halbach array is an array of magnets orientated to guide the magnetic field creating an increase in magnetic field on one side of the array. The other side of the array will have a reduced magnetic field.

When the magnetic fields are increased using multiple magnets in a Halbach-inspired configuration, the magnetic coupling has potential to be used as the propulsive mechanism.

4.3 Flexure Joint

The Flexure Joint uses a flexible material at the joint of the fin ray (Fig. 5c). This flexure joint is fused with both the hull and the fin ray to create a continuous hull. The fin ray will be actuated using an electric motor that is located inside of the hull.

4.3.1 Flexure Properties

The main difficulty of this design will be combining the required flexibility to reduce the fatigue effects and the rigidity to counter pressure difference.

A flexure joint can be used to allow an oscillating motion of the fin ray while maintaining a continuous hull. Though it is not a standard application for the flexure joint, it does propose an option to function as a hull since the flexure consists of a single material. The flexure only provides the continuous hull, it therefore has little influence on the design of the internal mechanism allowing for wide application.

This solution has the benefit of a smooth surface. Contrary to the other propulsive mechanism designs, there are no crevices or gaps which could trap debris and block the movement of the fin rays.

Fatigue of the material will be the main subject of this section since flexure joints are prone to fatigue [11, 37]. Fatigue is the result of a combination of the stress in the material and the number of cycles of the fin ray movement. The large strain combined with the high cycle number could cause fast fatigue of the flexure joint.

The estimations will be based on leaf springs. Machekposhti et al. 2015 shows that several compliant joints have the range of motion that meets the requirements, however, these are not suitable as a hull. These designs do all show the use of long leaf springs, so that is the flexure type that will be investigated (Fig. 13a).

The size of the flexure will depend on the material that is used and the type of flexure that is used. Because each material has a maximum strain that is allowed for the material to survive a certain number of cycles, and the movement is determined by the movement of the fin, a minimal ratio between thickness and length of the flexure can be determined. Due to the low thickness and the flexures replacing the hull, the weight of the flexures is neglected.

In order for a flexure to be designed further, rules for the flexure are created.

- The flexure may not show gaps or cross itself or the fin in any cross section. Because the flexure must be fused with the hull at all sides, it can be seen as a sheet. A loop in the cross section would mean the sheet has to cross itself, which is only possible if it is cut. This would create a hull breach unless it is fused together at the position the sheet crosses. This results in the crossing paths not moving relative to each other and therefore not contributing to the strain or compliance of the flexure (Fig. 13b).

- The length of the flexure does not have to be from one flexure but can be created using flexures in series. Important to remember is that the connection between flexures can add extra length to the minimal length ($\theta_\mathrm{f} = \Sigma_{i=1}^{n}\theta_i$ or $d_\mathrm{f} = \Sigma_{i=1}^{n} d_i$).

For simplicity, the calculations will be done on straight flexure that holds the fin. Because the calculations are based on maximum strain of the material in the direction of the fin movement and not on the total forces on the flexures this is possible. The flexure has dimensions length l_f, height h_f and width w_f (Fig.14).

The following assumptions are made regarding the estimation of the maximum strain:

- The bending of the flexure is homogeneous as a result of the attached fin ray bending

- The thickness of the plate does not change during the bending

Euler Bernoulli beam theory is used. Since the goal of this estimation is to find the maximum strain and the bending is homogeneous, the shear strain will not be taken into account at first. The maximum strain difference will likely occur on the surface of the flexure due to the flexure bending in both directions. If this strain is too low to cause fatigue, further calculations using a finite element method will be performed.

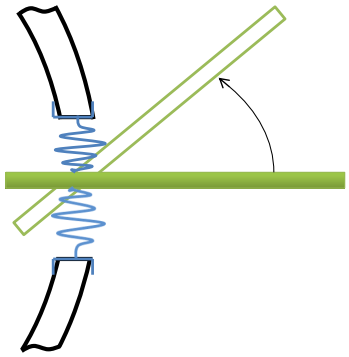

(a) Simple representation of how a flexure could be used as a hull. Black is the solid hull of the vehicle, green the fin and blue the flexure.

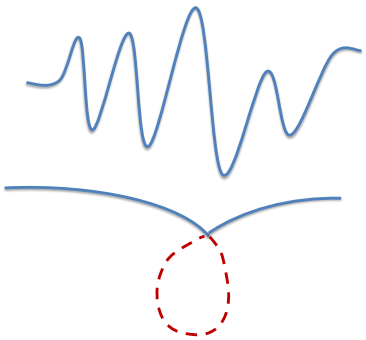

(b) Cross-section of two flexures. When crossing itself in the cross-section, the loop that is created (dotted red) does not add to the compliance properties of the flexure.

Figure 13: Schematic representation of the positioning of the flexure and visualization of a flexure crossing itself.

4.3.2 Designs

Two types of flexure joint designs will be investigated, a rotational and a translational. The rotational flexure joint allows the pendulum motion as shown in Figure 13a. The translational flexure joint allows a translational motion of the fin ray without any rotational motion as shown in Figure 15.

The maximum bending a flexure can tolerate for a certain number of cycles is determined by the stress-cycle-curve of the flexure material and the dimensions of the flexure. The maximum strain that materials can endure for 10^7 cycles can be found using CES Edupack.

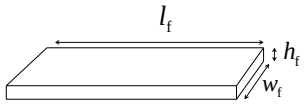

Figure 14: Dimensions of the simplified flexure.

Rotational Flexure Joint

When the rotational flexure is bend, the flexure will create an arc. The radius of this arc can be used to create an equation that combines the dimensions of the flexure to the fin ray angle and the maximum strain of the flexure. Assuming a flexure with thickness h_f of a material with maximum allowable strain ϵ_m, the maximum radius of the flexure will be

$$R_\mathrm{m} = 2\frac{\frac{1}{2}h_\mathrm{f}}{\epsilon_\mathrm{m}} = \frac{h_\mathrm{f}}{\epsilon_\mathrm{m}}, \tag{26}$$

with R_m the radius of the bended flexure, h_f the thickness of the flexure, and ϵ_m the maximum allowable strain. The product of two is the result of the flexure bending both directions with θ_f.

This means that knowing the required range of the fin movement, rotation θ_f, a ratio of minimal required length (l_f) to thickness of the flexure can be determined:

$$l_\mathrm{f} = R_\mathrm{m}\theta_\mathrm{f}, \tag{27}$$

$$\frac{l_\mathrm{f}}{h_\mathrm{f}} = \frac{\theta_\mathrm{f}}{\epsilon_\mathrm{m}}, \tag{28}$$

with l_f the flexure length and θ_f the fin ray angle. This ratio will be used in combination with the pressure difference equation and material data to find whether the rotational flexure is a suitable solution.

Translational Flexure Joint

The translational flexure joint uses a different type of flexure that does not bend into an angle but into an s-curve and moves the fin ray laterally (Fig. 15). This means that a deflection is needed instead of an angle. To find a deflection that is comparable to the maximum fin ray amplitude, the surface that the fin ray covers in the motion plane is chosen to be equal:

$$\frac{1}{2}l^2\theta_{\mathrm{f}} = ld_{\mathrm{f}}, \tag{29}$$

with l the length of the fin ray and d_{f} the deflection of the fin from the neutral point. This means that if the fin length of the rotational and translational fins are equal, the deflection of the translational fin will be

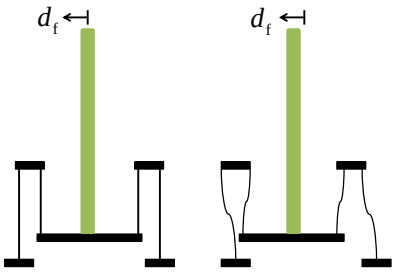

Figure 15: Representation of the workings of a translational flexure.

$$d_{\mathrm{f}} = \frac{1}{2}l\theta_{\mathrm{f}}. \tag{30}$$

The deflection of a translational flexure for a maximal allowable stress σ_{m} is expressed using the following equation [37]

$$\Delta x = \frac{2}{3}\frac{l_{\mathrm{f}}^2}{h_{\mathrm{f}}}\frac{\sigma_{\mathrm{m}}}{E} = \frac{2}{3}\frac{l_{\mathrm{f}}^2}{h_{\mathrm{f}}}\epsilon_{\mathrm{m}}, \tag{31}$$

with Δx the deflection of the flexure, σ_{m} the maximal allowable stress, and E the Young's Modulus.

4.3.3 Pressure Difference

The equation for the deflection due to the pressure difference will now be derived.

The pressure difference is simulated as distributed load on the flexure. The flexure is seen as a beam that is fixed at both ends (fused with the hull and the fin in neutral position) with a uniform load as a result of the pressure difference (Fig. 16). This means that the deflection of the flexure will be:

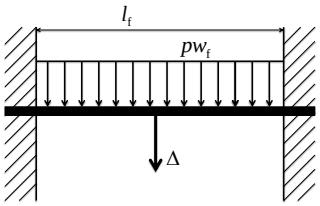

Figure 16: Simplified model of the pressure difference in on the flexure. Variable p is the pressure difference acting on the flexure, w_{f} the theoretical width of the flexure, l_{f} the length of the flexure and Δ the deflection.

$$\Delta = \frac{pw_{\mathrm{f}}l_{\mathrm{f}}^4}{384EI}, \tag{32}$$

with Δ the deflection, p the pressure difference in Pascal, and I the inertia of a beam:

$$I = \frac{1}{12}w_{\mathrm{f}}h_{\mathrm{f}}^3. \tag{33}$$

The deflection due to the pressure difference then becomes

$$\Delta = \frac{pl_{\mathrm{f}}^4}{32Eh_{\mathrm{f}}^3}. \tag{34}$$

This equation for the deflection due to the pressure difference is used for both the rotational and the translational flexures.

4.3.4 Motion and Pressure

The remainder of this chapter combines the deflection due to pressure difference with the equations found for the rotational and translational flexures. This will result in equations predicting the behavior of the flexures when subjected to the pressure difference and actuation.

Rotational

The ratio of Equation (28) is inserted in the function for the deflection of Equation (34) to find the minimum length to height ratio of the rotational flexure. The function will become

$$\Delta = \frac{12pl_\mathrm{f}}{384E}\left(\frac{\theta_\mathrm{f}}{\epsilon_\mathrm{m}}\right)^3 = \frac{pl_\mathrm{f}}{32E}\left(\frac{\theta_\mathrm{f}}{\epsilon_\mathrm{m}}\right)^3. \tag{35}$$

Note that the displacement is a linear function of the length of the flexure. Second, the thickness of the flexure contributes via the ratio of Equation (28), which means that the thickness has the maximal amount of thickness within the maximal allowable strain. The only allowable change in thickness will be thinner which would mean that the deflection increases.

Entering the requirements and a maximum deflection of 10 % of the flexure length results in a maximum ratio of the flexure material properties. This maximum property ratio will be

$$\frac{E^2}{\sigma_\mathrm{m}^3} = \frac{0.10l_\mathrm{f}}{l_\mathrm{f}}\frac{32}{p\theta_\mathrm{m}^3} \approx 7.4 \cdot 10^{-5}\mathrm{MPa}^{-1}, \tag{36}$$

with σ_m the maximum stress in the flexure and θ_m the maximum amplitude of the fin. The inserted values are $p = 0.3\,\mathrm{MPa}$ and $\theta_\mathrm{m} = 30^\mathrm{o} \approx 0.5236\,\mathrm{rad}$, as stated in the requirements (Table 1).

This ratio can then be used with CES Edupack, creating a graph which easily shows which materials can be used as materials for the flexure (Fig. 17). The horizontal axis shows the maximum strain that the materials can withstand for 10^7 cycles. The vertical axis shows the values that result from Equation (36) for the different materials.

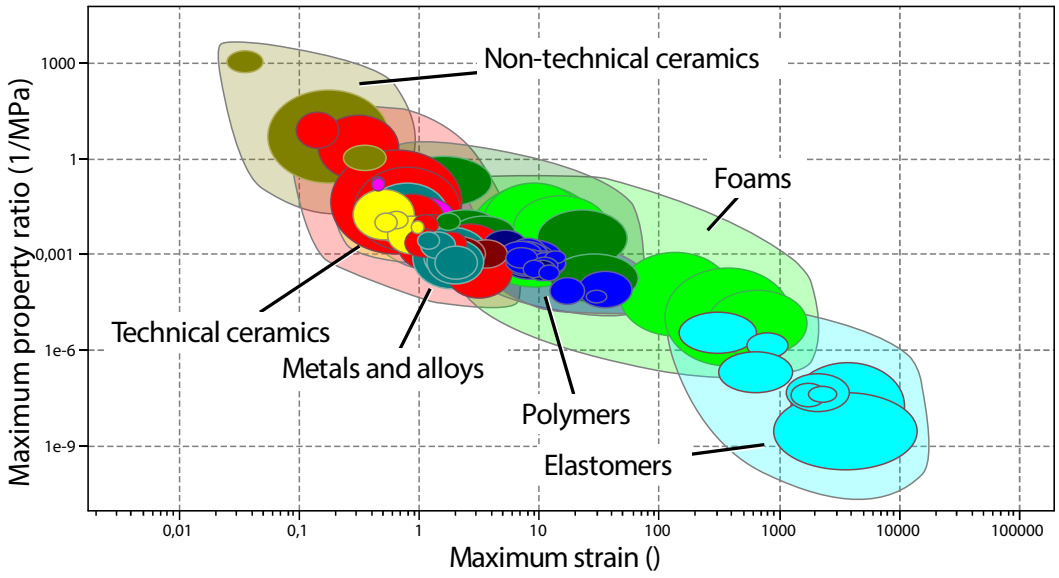

Figure 17: Different material properties with on the x-axis the maximum allowable strain without fatigue for 10^7 cycles. The y-axis shows the maximum property ratio E^2/σ_m^3 from Equation (36). Figure created using CES Edupack.

Figure 17 shows that the materials that comply with Equation (36) have a maximum strain ϵ_m of about 10 to 10000 before fatigue occurs at 10^7 cycles. Using Equation (28) it is clear that this ratio is not a realistic solution. In order for the flexure deflection to be lower than 10 % of the length, the flexure thickness h_f should be 20 to 20000 times larger than the flexure length l_f.

These unrealistic dimensions of the rotational flexure are the result of the flexure not being able to both resist the pressure difference and have the compliance for the large deflection without causing fatigue. The

flexure will deflect into the hull of the vehicle due to the compliance. Because of this, the rotational flexure is rejected as a possible solution.

Translational

The displacement of the translational joint that is shown in Equation (31) is rewritten and combined with Equation (34). This will result in an equation for the deflection due to pressure difference as a function of the possible fin ray deflection. The displacement due to pressure will be

$$\Delta = \frac{9p}{128Eh_{\mathrm{f}}\epsilon_{\mathrm{m}}^2}\Delta x^2, \tag{37}$$

with the fracture ranging from approximately 10 to $1 \cdot 10^{10}$ for a flexure with thickness 1 mm, depending on the material. The equation shows that the displacement of the fin ray Δx is quadratically related to the displacement due to the pressure difference Δ. If the allowed displacement of the translational flexure would be increased by a factor two, the displacement due to the pressure difference would increase by a factor four. This will cause the flexure to collapse on itself, resulting in contact between the flexures. This contact can cause failures to the mechanism. The translational flexure joint is therefore not a possible solution and is rejected.

4.3.5 Summary

The flexure joint uses the compliance of a material as a joint that has little to no friction. In this section the flexures are used as a means to obstruct water from entering the hull. The compliance allows the flexure to be statically connected to both the hull and fin ray, while allowing the fin ray to oscillate.

A rotational flexure and a translational flexure are investigated. An analytical estimation is made for both designs that couples the length and thickness to the strain of the material at the maximum fin amplitude. These functions are combined with another analytical estimation for the deflection due to the pressure difference.

Using the amplitude of the fin ray and a deflection that is a percentage of the length of the flexure, a ratio is determined for the rotational flexure based on the Young's Modulus and the stress. This ratio is then used to find a suitable material. The material properties of the possible materials will in turn result in a length to height ratio. This ratio indicates that the thickness must be 20 to 20000 times larger than the length. This is an unrealistic dimension that results from the combination of compliance and stiffness that is required to find a material. A homogeneous material will not be able to resist the pressure while allowing the required fin rotation. For that reason the rotational flexure is rejected as a possible propulsive mechanism.

For the translational flexure an analytical equation is made to combine the flexure displacement with the pressure difference induced displacement. This equation shows that the fin displacement is quadratically related to the pressure difference. The translational flexure joint is therefore not a possible solution and is rejected.

5 Magnetic Parameter Estimation

Both the reluctance actuator and the flexure joint failed to meet the requirements, the magnetic coupling still shows potential. Therefore the magnetic coupling is chosen as the propulsive mechanism. Further simulations will be done using ANSYS. This will require parameters that are specific to the magnets. This chapter will estimate these parameters using an experimental set-up.

5.1 Parameter Estimation Set-up

The magnets that are used are simple cubic and block neodymium magnets with magnetization N42, acquired from www.magnetenkopen.nl. The cubic magnets have sides of 5 mm and block magnets have dimensions 5x5x15 mm. The neodymium magnets are chosen due to their high strength and low cost. A holder for the magnets has been fabricated from Polymethylmethacrylaat (PMMA), the design is shown in Figure 18. The parts are cut from plates of PMMA and assembled using bolts and nuts. All parts have low permeability as to not influence the magnetic fields.

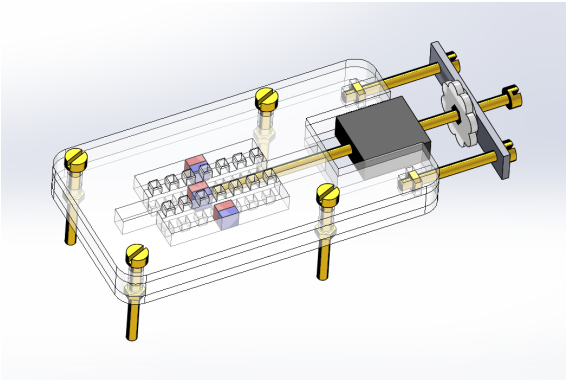

Figure 18: Experimental set-up to measure forces resulting from lateral magnet motion. Dimensions can be found in Appendix D.2.

The test will be conducted by moving a magnet through a magnetic field and measuring the magnetic forces at multiple positions. The magnet is pushed via a Futek LSB200 load cell using an M3 bolt with a pushing nut. The lead of M3 is 0.5 mm, meaning one full turn of the pushing nut results in 0.5 mm movement after which a static measurement is made.

The static force is measured during motion in both directions. Friction force is assumed to be equal in both directions, therefore the mean of the push and release forces is the magnetic force exerted by the magnets.

Different magnet placement combinations will be tested so different pitfalls will be assessed (Fig. 19). Outer magnets will be kept stationary and middle magnet will be moved using the load cell.

- *Single Magnet* (Fig. 19a) has a single stationary magnet on each side and a single moving magnet with the same pole orientation resulting in an attractive force.
- *Single Magnet inverted* (Fig. 19b) has the same set-up as the single magnet,only the pole of the moving magnet is inverted resulting in a repulsive force instead of an attractive force.
- *Halbach Short* (Fig. 19c) has a Halbach array on each side of the moving magnet that increases the field intensity between the two arrays and reduce the field intensity outside of the two arrays. The moving magnet has the same orientation as the magnets in the middle of the Halbach arrays.
- *Halbach Long* (Fig. 19d) has the same magnet placement as the *Halbach short*, only a longer magnet of 15 mm is used as the moving magnet so attractive and repulsive forces are combined.

The force from the magnet is measured in the motion direction using Labview 16.

The same tests will be simulated to find the correct magnetic properties for the simulation program. The variables that are used in ANSYS to simulate a force are the intrinsic coercive force and the relative permeability of the material.

ANSYS AIM 18.2 is used to simulate the static forces and compared to the physical data from the tests. ANSYS is chosen for its ability to import Solidworks designs and its capability of simulating magnetic fields in three dimensions which will be required later in the design simulation.

Only the intrinsic coercive force will be variated in the simulations. The relative permeability of neodymium magnets is 1.05 for all different types, but the intrinsic coercive force has a range of 875 kA/m

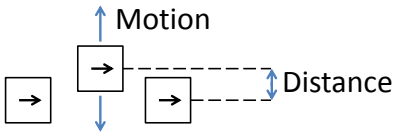

(a) Single magnet with like polarization.

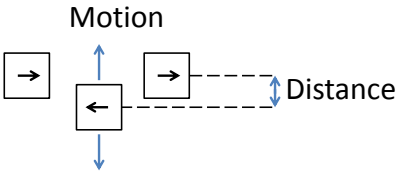

(b) Single magnet with inverted polarization.

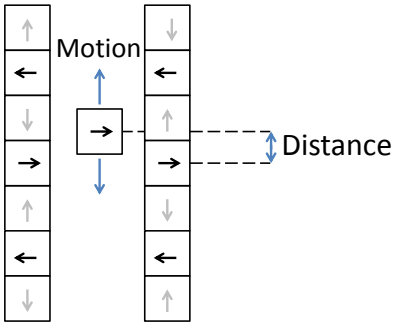

(c) Halbach array on both sides of moving magnet.

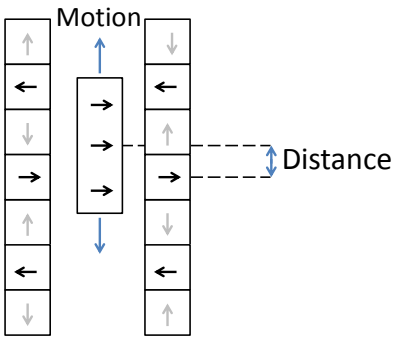

(d) Halbach array on both sides of magnet with 15 mm length.

Figure 19: Different test set-ups that will be tested in order to validate the ANSYS simulations. Main magnets are shown in black, secondary magnets in gray. The magnets are cubic with sides of 5 mm.

up to 2.65 MA/m [5, p. 628] [35]. The intrinsic coercive force will be varied in the simulation to find the correct values for the magnets that are used. The physical data and the simulation data will be compared using the sum of the normalized squared difference.

5.2 Magnetic Parameter Estimation Results

Simulations with various intrinsic coercive force values are run for the different test. An interpolation has been done on the simulation results to increase the precision of the solution. The simulation data is compared with the measured data to find the intrinsic coercive force with the best correlation to the measured data. This is done using the normalized squared difference between the measured data and the different simulations.

Figure 20 shows the sum of the normalized squared difference between the physical tests and the simulations. The sum is taken over all different tests. Only the peaks in force have been used, due to their importance in the final design and the relative lower influence of the friction force on the magnet. The normalized least squares solution gives an intrinsic coercive force of 892870 A/m.

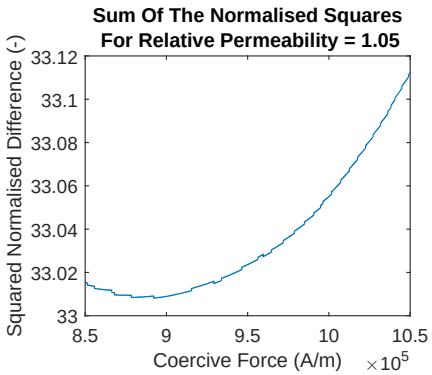

Figure 20: Sum of the squared difference between the physical tests and simulations of all tests as a function of the coercive force. Relative permeability is set to 1.05.

The normalized least squares solution is used to simulate the test once more and the new simulation data is compared with new physical data. Figure 21 shows the physical data and the simulated data together. The average absolute difference between the physical and simulated data is 0.036 N which translates to an average percentage difference of 3.3 %.

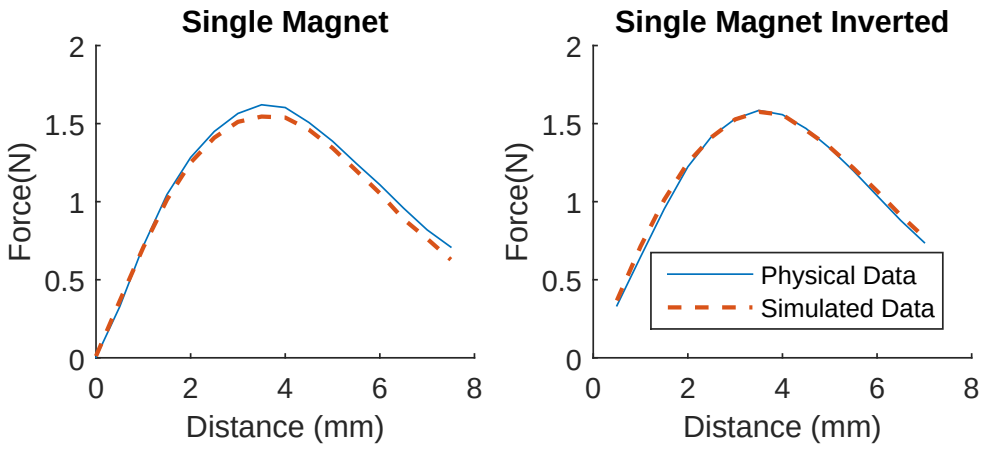

Figure 21: New physical and simulation data comparing the parameter estimates to physical data.

6 Magnetic Coupling Design Selection

This chapter introduces six magnetic coupling designs. Next, five comparison criteria are created and the designs are simulated using the parameters found in Chapter 5. Using the forces found in the simulation a selection will be made which design will be used further.

6.1 Magnetic Coupling Designs

Three design types have been simulated; a coaxial design, a face-to-face design, and a moment-arm design. Each design has an attractive and a repulsive version. Dimensions of the designs can be found in Appendix D.3 and the mass of the designs can be found in the caption of the figures in this chapter. The repulsive versions have the benefit of centering the external part of the mechanism during peak torques due to the symmetry of all the designs, which will reduce friction forces.

The coaxial coupling design would be used by inserting the coupling in the axle of the fin ray with the internal part of the coupling inside of the hull and the external part of the coupling integrated in the fin ray. This restricts the dimensions of the coupling since there will only be 30 mm in axial direction to generate enough torque. It does on the other hand reduce the internal volume use of the mechanism.

The face-to-face coupling design will use a face-to-face configuration with an adaption so that on either side of the driven face a driving face is positioned resulting in a total of three faces. This is possible since the driven face is not connected to an output shaft but to an oscillating fin ray which is perpendicular to the rotation axis. This has two benefits with regard to a standard face-to-face coupling. First, the axial forces on the driven part will be reduced since the attractive or repulsive forces are symmetric in this direction. Second, the magnetic field experienced by the driven face is higher as a result of the continuïty of the flux.

The moment arm is a adaption to the face-to-face magnetic coupling and uses an internal and external arm to rotate the fin ray. The internal arm is symmetric in the motion plane so the forces in perpendicular direction to the rotation are symmetrical and create an unstable equilibrium. This reduces undesired forces on the fin axle. The double arm is used by the internal arm since the internal arm has no fluid drag.

All designs are created symmetrical to reduce noncontributing forces. The interactive forces of the magnets are much higher in directions other than the rotational direction. This is due to the rotational forces being a result of the magnetic forces being angled. These forces cannot be used for applying torque, so the symmetrical magnet placement is used to reduce the impact of these forces (Fig. 22).

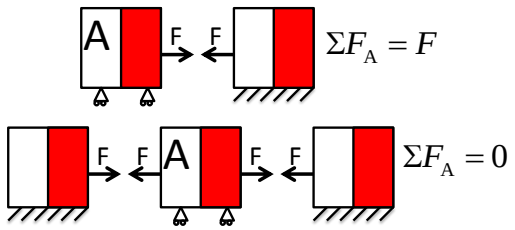

Figure 22: Two magnets create a resulting force F_A on magnet A. Three magnets create an unstable equilibrium for magnet A that reduces forces in noncontributing directions.

All coupling designs have Halbach-inspired magnet orientation, which increases the field strength of the couplings. The orientations are mostly not complete Halbach arrays, but are additional magnets positioned in a way that the magnetic field of the main magnets is increased. All repulsive versions lack the attractive main magnet to reduce the unstable equilibrium in the neutral position.

Magnetic pole directions in the following figures are shown using arrows pointing south to north.

Coaxial Attractive

The attractive coaxial design uses 12 cubical magnets in the external part and two cubical magnets in the internal part with 5 mm edges (Fig.23). The magnets in the external part are arranged in a Halbach-array configuration that directs the magnetic field inwards, increasing the torque capabilities of the coupling. The internal part holds two magnets with like poles facing each other.

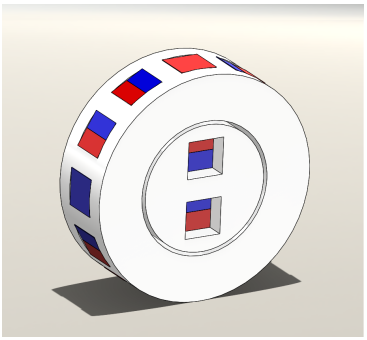

(a) Positioning of the inner and outer ring of the coupling. The inner ring will be the driving part on the inside of the hull, the outer ring will be the driven part on the outside of the hull.

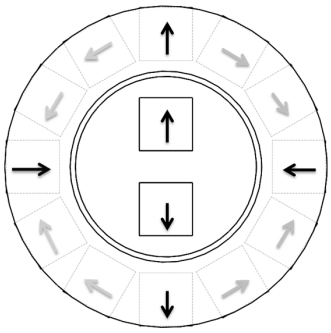

(b) Schematic drawing of the magnet orientation, arrows show pole direction from south to north.

Figure 23: Coaxial Attractive. Main magnets are shown in black, secondary magnets in gray. Dimensions can be found in Appendix D.3, the mass is approximately 20 g.

Coaxial Repulsive

As mentioned, the attractive coaxial design creates an unstable equilibrium which can increase force on the bearing resulting in higher friction forces. To reduce these forces the ring is used in a matter that creates a repulsive connection between the internal and external parts of the mechanism (Fig.24). The magnet orientation is not a complete Halbach array, but still allows for minor Halbach effects that increase the torque of the coupling. The internal part of the mechanism is equal to that of the attractive coaxial design.

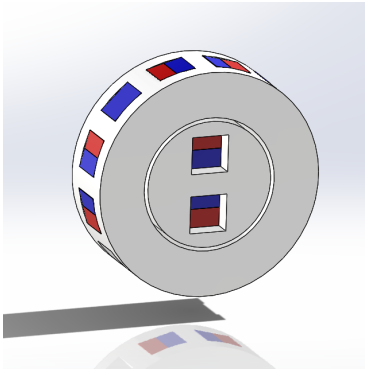

(a) Positioning of the inner and outer ring of the coupling. The inner ring will be the driving part on the inside of the hull, the outer ring will be the driven part on the outside of the hull.

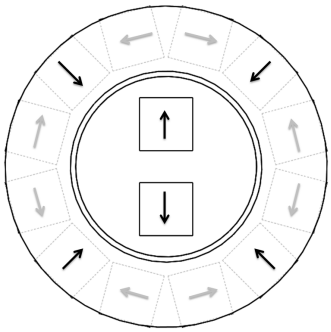

(b) Schematic drawing of the magnet orientation, arrows show pole direction from south to north.

Figure 24: Coaxial Repulsive. Main magnets are shown in black, secondary magnets in gray. Dimensions can be found in Appendix D.3, the mass is approximately 20 g.

Face-to-Face Attractive

The attractive face-to-face coupling uses a 12 cubic 5 mm magnets in each driving face in Halbach-inspired orientation (Fig. 25). The orientation is such that the flux increase of both driving faces is created towards the driven face in between. Four main magnets per face will direct the magnetic fields towards the driven face.

The driven face has four cubic 5 mm magnets that are orientated with their poles in the same direction as the main magnets of the driving faces. This will result in an attractive force when a relative angle is created.

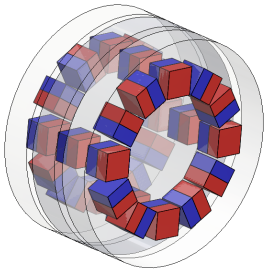

(a) Positioning of the faces of the coupling with the magnets shown. The two outer faces are the internal parts, the middle face is the external part of the coupling. Red is north pole and blue is south pole.

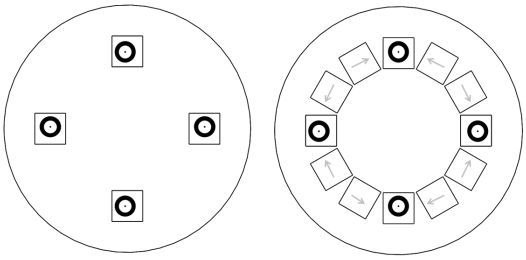

(b) Schematic drawing of the magnet orientation with left the face outside of the hull and right the face inside of the hull.

Figure 25: Face-to-Face Attractive. Main magnets are shown in black, secondary magnets in gray. Dimensions can be found in Appendix D.3.

Face-to-Face Repulsive

The repulsive face-to-face coupling has the same magnet orientation as the attractive face-to-face coupling with the adaptation that the magnet in the driven face has its polarization in the opposite direction resulting in a repulsive force (Fig.26). This also means the driven face has a stable equilibrium position that has a 45^{o} difference with the attractive face-to-face design.

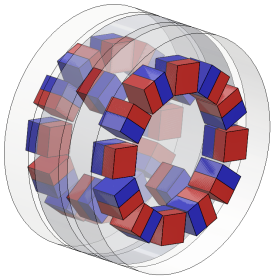

(a) Positioning of the faces of the coupling with the magnets shown. The two outer faces are the internal parts, the middle face is the external part of the coupling. Red is north pole and blue is south pole.

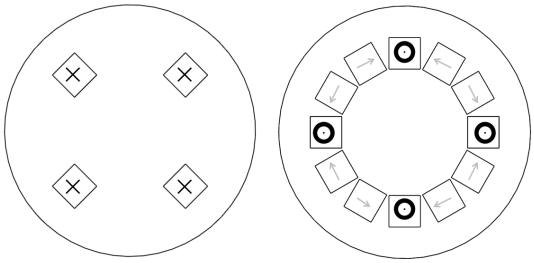

(b) Schematic drawing of the magnet orientation with left the face outside of the hull and right the face inside of the hull.

Figure 26: Face-to-Face Repulsive. Main magnets are shown in black, secondary magnets in gray. Dimensions can be found in Appendix D.3, the mass is approximately 50 g.

Moment Arm Attractive

The Moment Arm Attractive has magnets in the internal arm positioned in a Halbach array to increase the forces exerted on the external arm (Fig.27). The array is curved to increase the forces in the maximum amplitude of the fin. This also reduces the forces that the neighboring mechanisms have on each other. The internal arm is used in combination with magnets with dimensions 5x5x15 mm to compensate for the difference in trajectory of the internal and external magnets. The external moment arm has a magnet of 5x5x15 mm which is positioned under 90°, resulting in added repulsive forces.

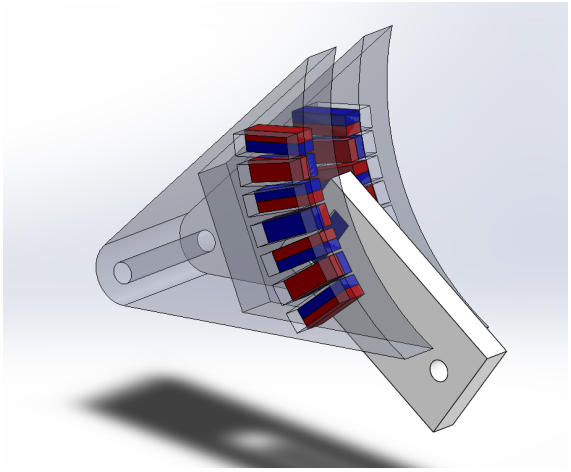

(a) Design of the magnets for the attractive Moment-Arm design. The external arm is shown in white, the internal arm is shown transparent.

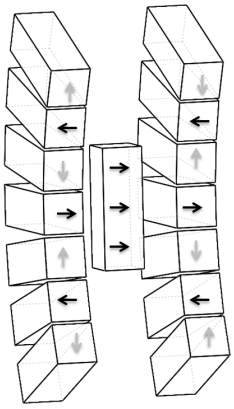

(b) Positioning of the magnets for the attractive Moment-Arm design. Arrows show the direction of the internal flux of the magnet.

Figure 27: Moment Arm Attractive. Main magnets are shown in black, secondary magnets in gray. Dimensions can be found in Appendix D.3, the mass is approximately 125 g.

Moment Arm Repulsive

Because the highest forces are required at the maximum amplitude of the fin, the magnets in the internal arm of the mechanism are angled to line up with the magnet on the external arm when the external arm is rotated to 30° (Fig. 28). The repulsive moment arm uses repulsive forces for its torque coupling in order to reduce the noncontributing forces. The direction of the magnets is shown in Figure 28b. There are no magnets in the internal arm with the same pole orientation as the magnet in the external magnet to reduce the noncontributing forces.

The external moment arm is has a length of 40 mm from the center of the magnet to the center of the axle.

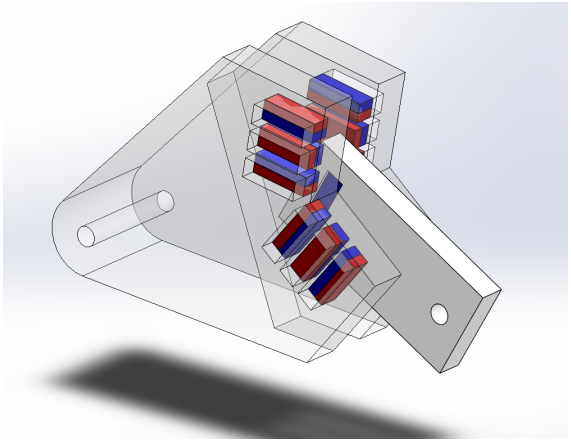

(a) Design and positioning of the magnets for the repulsive moment-arm design. The external arm is shown in white, the internal arm is shown transparent.

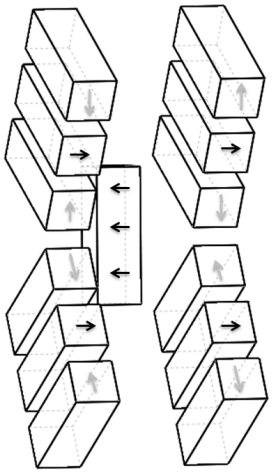

(b) Design and positioning of the magnets for the repulsive moment-arm design. Arrows show the direction of the internal flux of the magnet.

Figure 28: Moment Arm Repulsive. Main magnets are shown in black, secondary magnets in gray. Dimensions can be found in Appendix D.3, the mass is approximately 168 g.

6.2 Comparison Criteria

To compare the different designs comparison criteria are required. These criteria will be used to find a suitable design for the coupling.

The most important criterion for the coupling will be its ability to transfer the required torque. Without enough transferable torque the propulsion will lose performance or functionality. Maximal torque will be compared while keeping scaling of the mechanism in mind.

The different designs will also result in a different angle of play between the torque peaks, affecting the controllability. Since the distance between the magnets is the cause of the torque transfer, the relative angle between the internal and external part of the coupling will determine the torque. This results in different torque-angle characteristics for different couplings.

The friction force that the coupling experiences as a result of noncontributing forces is also important. The friction is difficult to estimate, but by simulating the noncontributing forces, a comparison of friction between the different couplings can be made. This friction could be increased when the coupling is misaligned or damaged, so the consequences of misalignment will also be taken into account. If contact between the coupling and the hull results of the misalignment, it could result in wear and ultimately a breach of the hull.

The magnetic influence of one coupling on its adjacent couplings must be taken into account. Since the couplings will be positioned in close proximity to each other, the magnetic fields of the different designs might interfere. The interference can work either on the external- or the internal part depending on the design of the coupling. Interference on the internal part will most likely only result in a different power use of the actuator. Interference of the external part could result in the loss of coupling. The use of Halbach orientations reduces interference due to the redirection of the magnetic fields.

The drag on the external part of the mechanism is disregarded. The drag that the external part experiences will be lowest at the maximum amplitude, where the fin ray has no velocity. This position requires the peak torque for the propulsion. It is therefore unlikely that the peak torque requirement will change due to the drag of the mechanism. The drag is therefore disregarded at this moment.

Weight will not be used in the comparison criteria since only the repulsive moment arm exceeds the requirements slightly. Trimming 15 % of the volume would allow the design to reach the requirement.

Figure 28 shows that there is a lot of material that could be trimmed.

The comparison criteria for the design selection, listed from most important to less important, are:

- Maximum transferable torque
- Noncontributing forces resulting in friction
- Misalignment consequences
- Angular play of peak to peak torque
- Influence on adjacent coupling

The different designs will be rated using the forces resulting from the simulations done in ANSYS based on the comparison criteria. This includes the torque that is transferred but also the forces and torques in noncontributing directions and forces as a result of the misalignment of parts. The results of the simulations can be found in the next section and the design choice based on the comparison criteria will be discussed in Section 9.3.

All designs will be simulated using the intrinsic coercive force found in the parameter estimation. The designs will be compared using the comparison criteria.

6.3 Design Type Simulations

The designs presented in Section 6.1 are simulated in ANSYS 18.2 to acquire the torques transferred by the magnets using the intrinsic coercive force of 892870 A/m as estimated in previous chapter. The magnet housings are simulated as PVC, the solver level is set to 7/8 to achieve the required error convergence and the mesh level is set to 1/9 since increased mesh does not increase precision of the results in these simulations.

Table 2 shows the maximum transferable torque of the different designs tested using ANSYS. The lowest play of the designs is also shown in the table. Play is defined as the angular difference between a peak and a trough with the angular difference measured on the internal part of the mechanism. For both moment-arm designs, simulation is done at the maximum amplitude (30^{o}) of the fin ray, which is the position where maximum torque is required. The internal arm is rotated.

For the face-to-face and the moment-arm designs, the distance between the internal and external magnets is simulated equal for the comparison.

Design	Max Torque (Nm)	Max Radial Force (N)	Play (degrees)
Coaxial Attractive	0.0186	~ 0	90
Coaxial Repulsive	0.0146	~ 0	45
Face-to-Face Attractive	0.1447	~ 0	40
Face-to-Face Repulsive	0.1438	~ 0	40
Moment Arm Attractive	0.2597	9.88	15
Moment Arm Repulsive	0.2905	11.8	15

Table 2: Peak torques, peak radial forces on the external axle, and angular play between the peak torques of the different designs.

Both coaxial designs show a clear lack in transferable torque. Increasing this torque to the requirement would include a substantial increase in the diameter of the coupling. The play in these designs is also higher than in the other designs.

The face-to-face and the moment-arm designs both have significant maximum torques, with the moment arm capable of slightly larger torques. This is partly due to the larger radius of the internal and external parts of the coupling. This larger arm is necessary due to the geometry of the moment arm, a smaller arm would not allow for a full actuation of the fin ray.

The maximal radial forces on the external axle show that the moment-arm design will create a large friction force between the external part of the coupling and the axle. The radial forces can get up to 11 N

radially on the axle of the moment arm. These radial forces will be very small for the face-to-face and the coaxial designs due to the combined axle of the internal and external part of the coupling (given that the parts are aligned correctly).

The play of the moment-arm design is much lower than that of the other designs due to the geometry of the mechanisms. The large internal arm of moment-arm design allow for a large relative movement of the internal magnets with a small angular difference.

Play of the face-to-face is dependent on the which equilibrium point is passed. This can clearly be seen in Figure 29 when looking at the difference in peak position between the attractive and repulsive versions of the coupling.

When the coupling is misaligned a resulting force will act on the external magnets, depending on the position the coupling is in. If the position of the coupling is in a stable equilibrium (repulsive force between internal and external parts), a correcting force will occur. If this position is in an unstable equilibrium, the resulting force is linearly dependent on the distance from the center:

$$F_{\mathrm{m}} = k_{\mathrm{m}} \cdot d, \tag{38}$$

with F_{m} the force due to misalignment, d the distance of the external magnets in mm to the center of the coupling and k_{m} a magnetic force constant in N/mm depending on the coupling design (Table 3). This force constant can be seen as a spring constant.

Design	k_{m} (N/mm)
Face-to-Face Attractive	8.0
Face-to-Face Repulsive	6.7
Moment Arm Attractive	3.8
Moment Arm Repulsive	3.0

Table 3: "Spring" constant for the misalignment of the external magnet along the rotation angle.

Note that though the k_{m} of the face-to-face designs are 2-3 times higher than those of the moment arm, the resulting friction will be greater on the moment arm. Because the arm of the moment-arm design is 3.2 times the length of the face-to-face, noncontributing forces will create a moment which will be larger in the case of the moment arm.

The forces of the repulsive designs show a slight decrease compared to the attractive versions. This is expected due to the repulsive forces of a magnet being lower than the attractive forces [23]. For the moment-arm design the repulsive version has a higher torque due to the geometry of the coupling.

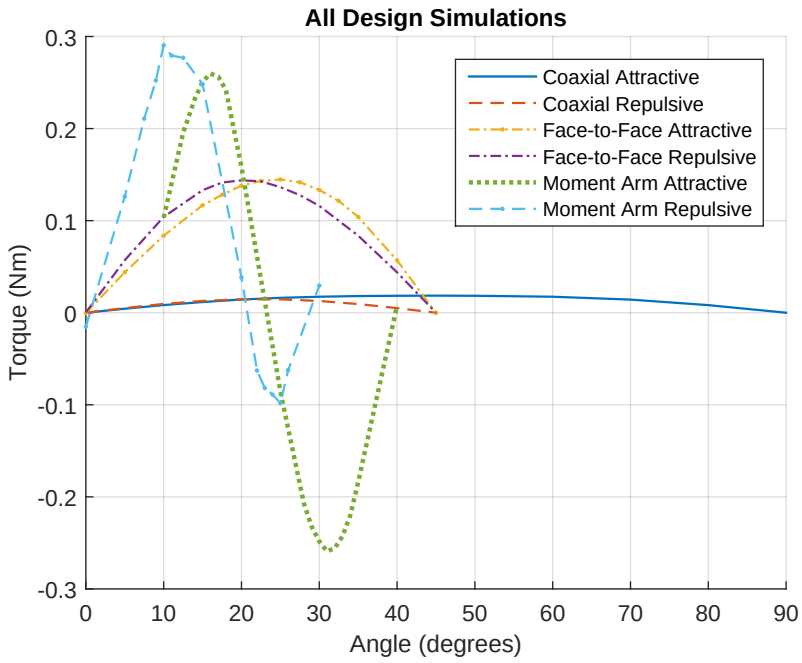

Figure 29: For the moment-arm designs, the positive torque is in the direction the peak torque is required. Other designs are point symmetric in the origin.

Due to the lower noncontributing forces and the lower misalignment consequences, the face-to-face design will be used for the validation testing. Both the attractive and the repulsive designs will be tested. The choices are discussed in Chapter 9.3.

7 Design Validation

The face-to-face design is chosen to be validated. This chapter will show the parts that are used in the validation, how the set-up of the validation is assembled, and how the testing is performed. Section 7.2 will include definitions which will be important to understand how the results are shown.

7.1 Parts and Assembly

The design validation is done using the face-to-face design, using the design of the previous chapter (Fig. 30a) as well as an adapted design with a larger diameter. The larger diameter is created by splitting the different Halbach-inspired segments (Halbach segments) apart and increasing the distance to the axle (Fig. 30b). This can be used to find the influence between sections on the original design and show the effect of scaling by radial increase only. The dimensions of the parts can be found in Appendix D.4.

The driving gear shown in Figure 30c is used to actuate the internal part of the mechanism using a stepper motor.

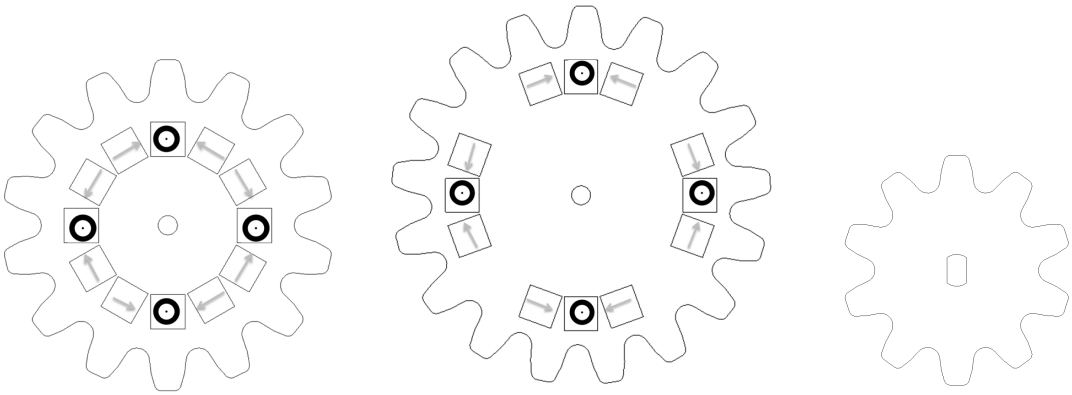

(a) Small internal part of the coupling.

(b) Large internal part of the coupling.

(c) Driving gear of the internal part of the coupling.

Figure 30: Internal magnet holders, both small and large, and driving gear. Pole directions of the magnets are shown using arrows. See Appendix D.4 for design drawings with dimensions.

By flipping the external part of the mechanism (Fig.31), the type of actuation can be changed between attractive and repulsive force actuation. This results in four different mechanism designs (design types) that will be tested:

- small repulsive (sr)
- small attractive (sa)
- large repulsive (lr)
- large attractive (la)

The tests are done using the same block magnets used for the magnetic parameter estimation (Chapter 5). The parts are laser-cut from PMMA and the magnets are held in using thin plastic on both sides glued to the PMMA parts.

The internal part will be actuated and the torque measurement will be performed on the external part of the coupling. The actuation will be continuous, however slow enough to not induce eddy currents. The torque measurement on the external part (Fig. 31) will also be done continuously.

The internal part of the coupling is actuated using two stepper motors type 28byj-48 5V. The steppers are driven by A4988 stepper drivers controlled by an Arduino UNO. More details can be found in Appendix

Figure 31: External part of the coupling. See Appendix D.4 for design drawings with dimensions.

E. Spur gears with 10 teeth (Fig. 30c) are connected to the stepper motors which turn the internal magnet holders. The internal magnet holders are rigidly connected to the axle, while the external magnet holder can rotate freely around the axle. This allows the internal and external part to rotate relative to each other (Fig. 32, 33). The end of the rod on the external part is connected rigidly to the test set-up through a Futek LSB200 load cell that measures the transferred torque of the coupling (Fig. 34). The load cell accumulates data continuously, the set-up is assembled using brass and stainless steel bolts and nuts to not interfere with the magnetic flux of the magnets.

The continuous rotation results in an continuously increasing relative angle. The resulting data will follow a sinusoid like motion with a period of 90^o, due to the symmetry of the mechanism.

A 90^o turn of both the small and the large coupling is simulated using ANSYS 18.2 with the parameters in during the parameter estimation. Around the peaks of the torque curves, the simulation points are increased for precision.

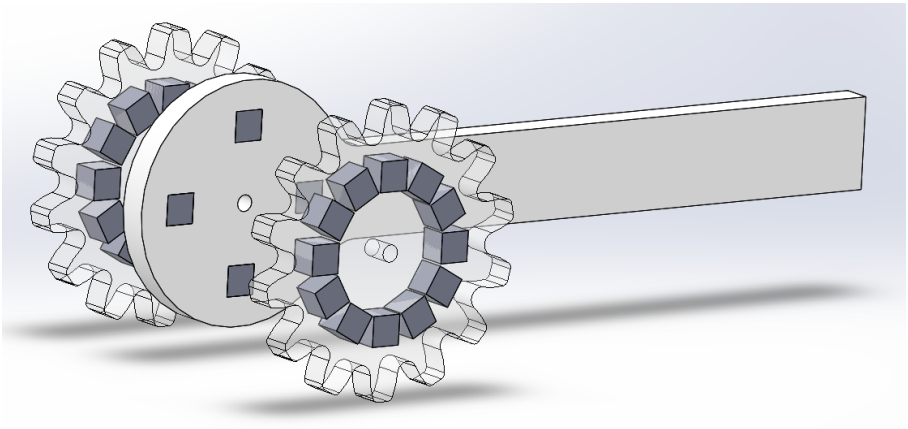

Figure 32: External and internal parts of the small coupling as used in the validation.

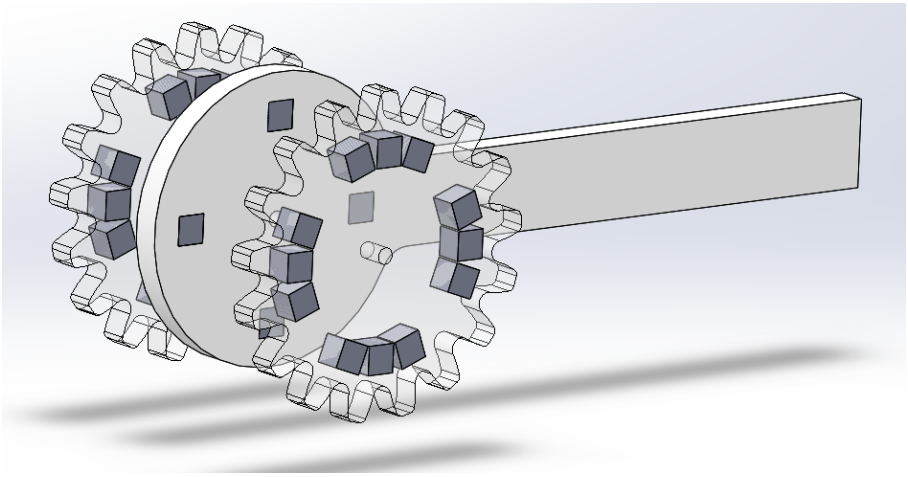

Figure 33: External and internal parts of the large coupling as used in the validation.

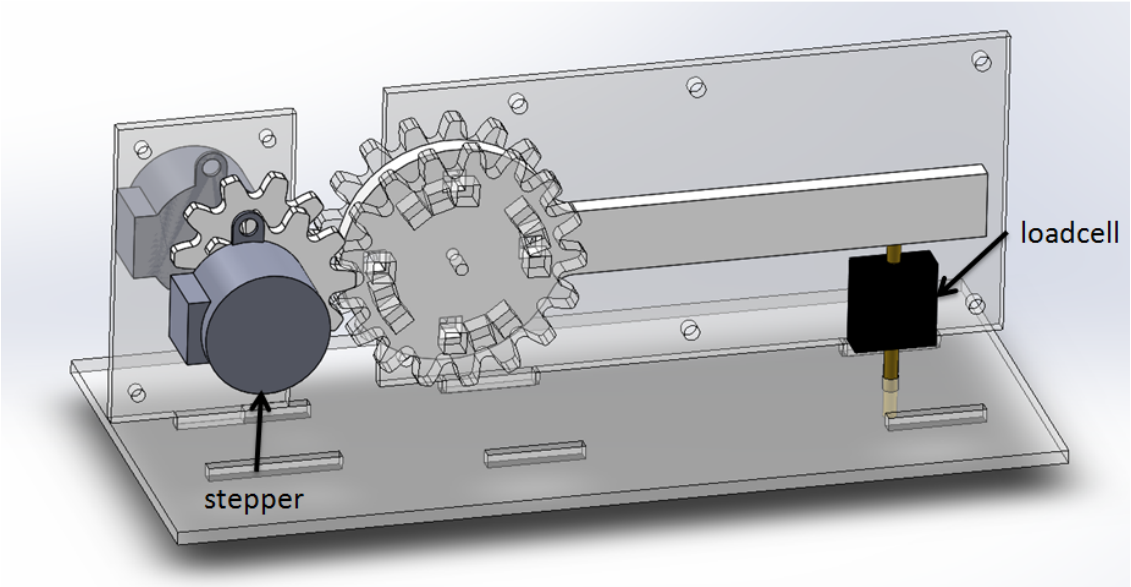

Figure 34: Test set-up of validation. The front panels have been left out for clarity. The black box is the load cell that measures the force, the gray cylinders are the stepper motors. Dimensions can be found in Appendix D.4

7.2 Data Acquisition

This section will expand on the way data is acquired and divided to allow for data analyses.

Size and Polarity

As mentioned, the validation of the simulation is done using two different face-to-face coupling sizes, with magnet positioning radius 12.5 mm (small) and 17.5 mm (large) (Figs 30a, 30b).

The polarity of the external part of the coupling is reversed during the tests, resulting in both attractive and repulsive style couplings. Note that the external part of the coupling is positioned in between the internal part of the coupling.

Measurements

Testing will be done in multiple sessions. First, a measurement will be done with one of the designs (sr, sa, lr, or la). A measurement is done by rotating the internal parts multiple full rotations clockwise, then counter-clockwise, then clockwise again, alternating multiple times. The clockwise direction is named *positive direction* and the counter-clockwise direction is named *negative direction*.

Each continuous positive or negative directional measurement is named a *section*. The measurements are always starting with a positive rotation. An example of the data resulting from the measurement is shown in Figure 35.

In order to compare the tests, sections are split into 90^{o} data segments which will be named *90-degree turns*. This is done by determining the peak torques in the data and separate the data in between the peaks using Matlab. The peaks are chosen to be used as indication for the data separation because the relative angle that the peak occurs is not influenced by the friction or sensor bias.

After multiple negative and positive rotation switches, the set-up is disassembled and one *session* is completed. Another design (sr, sa, lr, or la) is assembled and measured. Each design will be measured three times (multiple sessions of each design), to measure the error that results from the reassembly of the set-up.

When multiple sessions have been recorded, the magnets are removed from the designs and randomly repositioned. More sessions are measured using the new magnet configuration.

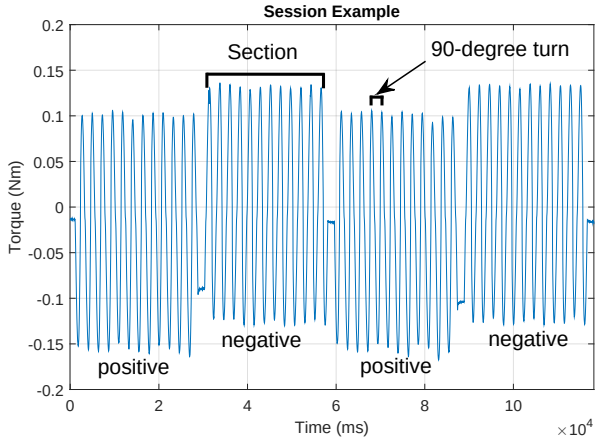

Figure 35: Example of one session composed of sections composed of 90-degree turns. The difference between the positive and negative turning direction is clearly seen in this example due to the shift in mean Torque.

Definition Recap

Test Each *test* is the collection of data that has been acquired using the same positioning of the magnets. In between the different tests, the magnets in the holders have been mixed to account for possible variation in the intrinsic coercive force between the individual magnets.

Session Each test is made up of *sessions* for both attractive and repulsive orientation of the external part of the coupling. Between the sessions, the magnet holders are taken from the axle and the external part of the coupling is reversed. This reversal changes the mechanism type between the repulsive and the attractive coupling type. The disassembly of the test set-up also accounts for possible variations resulting from the assembly of the test set-up, which could influence the friction and magnet distance during testing.

Section Each session is split into *sections*, resulting from a change of direction of actuation to account for the friction that is present between the axle and the magnet holders. The data between to direction switches are positive or negative direction sections.

90-degree turn Since the magnet holders are symmetrical, the sections are cut into *90-degree turns*. This is done because of the symmetry over 90°. These 90-degree turns are measured from peak to peak.

Section Types Difference has been made between the small and the large design, repulsive or attractive coupling, and positive and negative turn direction. This distinction result in eight groups which will be referred to as *Section Types*. The section types are Small Repulsive Positive (srp), Small Repulsive Negative (srn), Large Repulsive Positive (lrp), etc.

7.3 Data Processing

Specific points on the measured data are identified to aid in the validation of the data. The start and end of each section is determined and the sections are isolated. From the isolated sections the peaks and troughs are determined and using the peaks as a cut-off, 90-degree turns are separated (Fig. 36). The data sets that span 90 degrees will be used for the validation.

Friction in the set-up and bias of the load cell will create a bias in the section data, as can be seen in Figure 35 and 36a , that has to be corrected. The bias is corrected separate for the positive and negative turning directions. Based on the assumption that the forces are symmetric, the sections have been shifted such, that the mean torque of the peaks is equal to the absolute mean torque of the troughs. The offset is calculated using the mean of the peaks and troughs, and calculating the mean value of these means. The offset for the positive and negative turning directions is calculated separately.

The mean of the peaks and troughs is chosen for the bias correction rather than the signal mean, because these values are an accurate representation of the amplitude and thus the bias of the measurement. Actuation errors caused by the play in the set-up or stepper error would impact the symmetrical properties of the angle-torque correlation. If the signal mean is used, this could result in a bias of the data as a result of the set-up.

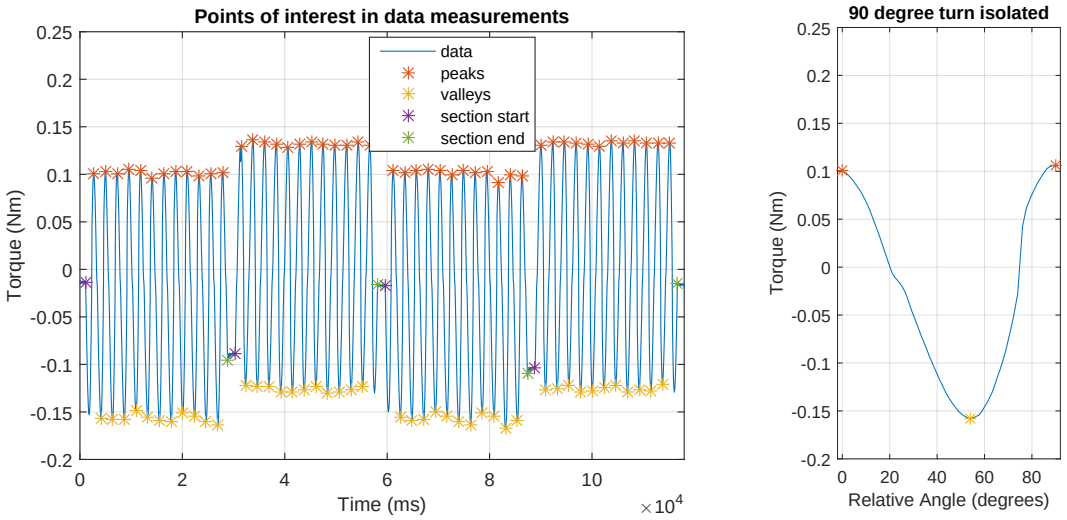

(a) Points of interest in the measured data. Section start and stop is used to isolated sections, peaks are used to isolate 90-degree turns.

(b) Isolated 90-degree turn.

Figure 36: Points of interest in the data that are used to isolate the data of different section types and one isolated 90-degree turn.

7.4 Data Analysis Method

Three steps are taken to show consistency within the measured data. The first step is to check the reliability of the sessions separately by calculating an intraclass correlation coefficient. The second step is to find a reassembly error that gives an indication of the variation in the torques as a result of the reassembly of the set-up. The last step is compare the different tests with a Pearson correlation coefficient, a regression line, and the maximum difference between tests. Potential variation in the last step can be compared using the reassembly error.

An Intraclass Correlation Coefficient (ICC) is calculated to check the reliability of the tests. It is a measure of the consistency of the repeated measurement. An ICC is calculated for each session with the positive and negative turning directions combined. The complete 90-degree turn data is used for the calculation using Matlab function `ICC.m` [29] based on single measures, absolute agreement, and 2-way mixed effects model.

The reassembly error is the error that can result from the reassembly of the set-up and will be calculated using the peak and trough values. The reassembly error will be based on the 95 % confidence interval of the mean. The different sessions within one test and design only differentiate as a result of the reassembly of the set-up. The largest difference between the lower and upper bounds of the confidence interval therefore gives a range in which the mean difference could be the result of a reassembly of the set-up.

The only variable between the sessions within one test is the reassembly of the set-up. The peaks and troughs are chosen for this calculation to exclude possible errors in the relative angle which could shift the data. This will result in the reassembly error, which will be used to compare the different tests with one-another and with the simulation done in ANSYS.

Three values are determined to find whether the tests are equal. First a Pearson correlation coefficient is determined to find whether linear correlation occurs between the two tests. Second a regression line is defined which indicates overall torque differences. Last the peak difference between the tests is calculated as a percentage of the peak value.

The Pearson correlation coefficient is determined between the mean of the different measurement tests, to find if the tests are linearly correlated. The correlation coefficient should have a value of approximately one if the tests have a linear correlation. If the data is linear correlated, a linear regression line can be determined (Fig 37).

The regression line tells us about the overall torque ratio and is defined as

$$t_{\mathrm{a}} = a_1 t_{\mathrm{b}} + a_0, \tag{39}$$

with t_{a} and t_{b} two tests that are compared and a_1 and a_0 the first order and zeroth order polynomial of the regression line respectively. If the overall torque is equal,

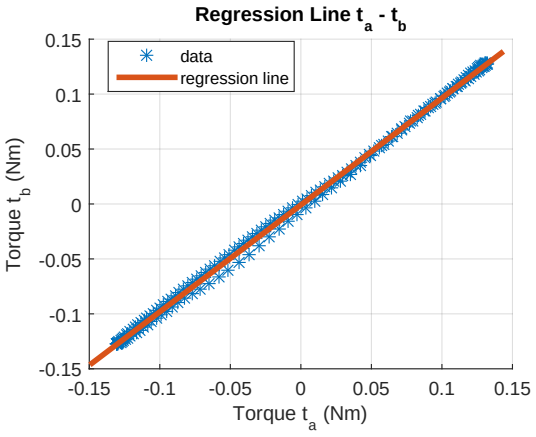

Figure 37: Example of the regression line for test a and test b.

$$t_{\mathrm{a}} = t_{\mathrm{b}}, \tag{40}$$

the first polynomial a_1 of the regression line must be one and the zeroth order polynomial a_0 must be zero. The zeroth order polynomial will be approximately zero due to the bias correction that is done on the data sets (Section 7.3).

The maximum torque difference is calculated in percentage of the peak torque value.

To compare the ANSYS simulation with the measured data, the Root Mean Square Error (RMSE) is calculated. The RMSE will be calculated using the mean of all tests and compared to the reassembly error.

8 Validation Results

This chapter displays the results following the method described in the previous chapter.

8.1 Intraclass Correlation Coefficient

The two lowest lower bounds of the 95 % confidence interval of all ICC's found are 0.79515 and 0.79736, all other lower bounds are above 0.9. A table containing all ICC's can be found in Appendix F.1.

8.2 Reassembly Error

Appendix F.2 shows the 95 % confidence interval of the mean of the peaks and troughs per session of the separate tests. The only variable within these tests is the reassembly of the set-up. This shows the difference due to reassembly. The reassembly of the set-up can influence the distance between the internal and the external magnets and influence the amount of play of the external part of the mechanism.

The reassembly of the set-up introduces an error of up to 11 % for small, and up to 14 % for large designs based on the torque peaks. This error is an indication of the error that arises, and is not an exact number. This difference can be used when comparing the different tests. If the difference between the confidence intervals of the different tests is within this difference, the error could be the result of the set-up reassembly.

8.3 Test Correlation

Tables 4 and 5 show the results of the correlation between the different tests. The tables show the Pearson correlation coefficient, the first order polynomial of the regression line, and the maximum difference between the means in percentage. The percentage is measured from the maximum value of the test depicted in the row label.

The Pearson correlation coefficients shown in Tables 4 and 5 show a minimum correlation coefficient of 0.994. This is the lowest coefficient of the small repulsive design. The lowest values of all other designs is 0.996.

The first order polynomials of the regression line are all within the reassembly errors found in the previous section. The biggest errors of each design are 10 %, 7 %, 7 %, and 6 % for small repulsive, small attractive, large repulsive, and large attractive respectively. All these maximum overall differences involve test 1.

	t1	**t2**	**t3**	**t4**
t1	1.0, 1.0, 0.0 %	0.999, 0.933, 12.6 %	0.994, 0.925, 16.0 %	0.998, 0.909, 13.3 %
t2	0.999, 1.07, 13.4 %	1.0, 1.0, 0.0 %	0.996, 0.991, 11.5 %	0.999, 0.973, 8.5 %
t3	0.994, 1.07, 17.0 %	0.996, 1.0, 11.5 %	1.0, 1.0, 0.0 %	0.999, 0.98, 5.12 %
t4	0.998, 1.1, 14.5 %	0.999, 1.02, 8.76 %	0.999, 1.02, 5.27 %	1.0, 1.0, 0.0 %

(a) Correlation results of the means of the tests for small repulsive design.

	t1	**t2**	**t3**	**t4**
t1	1.0, 1.0, 0.0 %	1.0, 0.957, 7.91 %	0.999, 0.982, 9.67 %	0.998, 0.929, 13.9 %
t2	1.0, 1.05, 8.25 %	1.0, 1.0, 0.0 %	0.999, 1.03, 7.03 %	0.998, 0.971, 6.77 %
t3	0.999, 1.02, 9.8 %	0.999, 0.973, 6.83 %	1.0, 1.0, 0.0 %	0.996, 0.943, 12.3 %
t4	0.998, 1.07, 14.8 %	0.998, 1.03, 6.93 %	0.996, 1.05, 13.0 %	1.0, 1.0, 0.0 %

(b) Correlation results of the means of the tests for small attractive design.

Table 4: Correlation results of the means of the small tests. The first number is the correlation coefficient. The second is the first order polynomial of the regression line with the row labels as x-value, and the column labels as y-value. The third number is the maximum difference between the means in percentage of maximum value of the row labels.

	t1	t2	t3	t4
t1	1.0, 1.0, 0.0 %	0.999, 0.943, 7.01 %	0.999, 0.932, 8.53 %	0.998, 0.995, 11.8 %
t2	0.999, 1.06, 7.5 %	1.0, 1.0, 0.0 %	1.0, 0.989, 2.79 %	0.997, 1.05, 15.8 %
t3	0.999, 1.07, 9.3 %	1.0, 1.01, 2.84 %	1.0, 1.0, 0.0 %	0.996, 1.06, 18.4 %
t4	0.998, 1.0, 11.8 %	0.997, 0.944, 14.7 %	0.996, 0.933, 16.8 %	1.0, 1.0, 0.0 %

(a) Correlation results of the means of the tests for large repulsive design.

	t1	t2	t3	t4
t1	1.0, 1.0, 0.0 %	0.996, 0.956, 15.1 %	0.998, 0.946, 9.44 %	0.996, 0.94, 14.5 %
t2	0.996, 1.04, 15.8 %	1.0, 1.0, 0.0 %	1.0, 0.987, 9.08 %	1.0, 0.982, 6.69 %
t3	0.998, 1.05, 10.0 %	1.0, 1.01, 9.18 %	1.0, 1.0, 0.0 %	1.0, 0.994, 8.82 %
t4	0.996, 1.06, 15.1 %	1.0, 1.02, 6.61 %	1.0, 1.0, 8.62 %	1.0, 1.0, 0.0 %

(b) Correlation results of the means of the tests for large attractive design.

Table 5: Correlation results of the means of the large tests. The first number is the correlation coefficient. The second is the first order polynomial of the regression line with the row labels as x-value, and the column labels as y-value. The third number is the maximum difference between the means in percentage of maximum value of the row labels.

The maximum errors do not all fall inside of the reassembly error. The maximum error percentages are 17 %, 14.8 %, 18.4 %, 15.8 % for small repulsive, small attractive, large repulsive, and large attractive respectively. Over half of the maximal errors that fall outside the reassembly error involve test 1.

8.4 Peak Torques

The RMSE's are shown in Table 6. The left column shows the RMSE between the simulation and the measured data. The right column shows the error that could result from the reassembly error.

	RMSE (Nm)	Allowed Error (Nm)
Small Repulsive	0.0166	0.0155
Small Attractive	0.0159	0.0155
Large Repulsive	0.0180	0.0267
Large Attractive	0.0165	0.0269

Table 6: Root Mean Square Error between the simulation and the measured data, and the allowed error using the reassembly error.

The torque values of the peaks of the measurement as well as the ANSYS simulation are shown in Figure 38. The values are shown per section type as a boxplot. The lower and upper border of the box indicate the 25th and 75th percentiles respectively of the data, the whiskers extend 1.5 times the box. The outliers that fall outside of the whisker range are not shown for clarity. Table 7 shows the number of data points that have been used in the boxplot and the number of outliers that have been left out.

8.5 Measurement and Simulation

Figure 39 shows the test means of the different measurement test and the simulation data from ANSYS. The graphs are symmetric in the zero torque point. Because the 90-degree turns are cut at the peaks instead of the zero torque points the graphs appear to be non-symmetrical.

The first thing to notice is the slight phase difference between the measured data and the simulation data for the small attractive and both the large designs.

The ANSYS simulation for the small designs also shows a higher torque than the measured data. In the large designs this difference does not occur. This is also indicated by the forces that the separate Halbach segments create (Table 8). These forces are recalculated from the torques that the designs produce. It shows

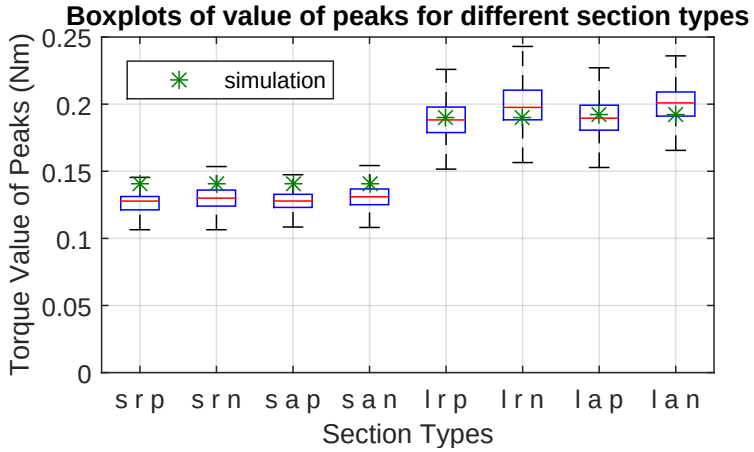

Figure 38: Torque values of the peaks and troughs of the different section types. The peaks of the simulation are shown as green stars. The x-axis shows the section types where the first letter indicates Small or Large design, the second letter Repulsive or Attractive type, and the third letter Positive or Negative actuation rotation. The box contains 50 % of the data, whiskers are 1.5 times the box size.

	# points	# outliers
s r p	1465	81
s r n	1421	47
s a p	1537	79
s a n	1421	42
l r p	1143	46
l r n	1075	31
l a p	1500	45
l a n	1315	54

Table 7: Number of peaks shown and number of outliers not shown in Figure 38.

that in the simulation, the forces created by the small design are higher than the forces in the large design. In the measured data, however, the forces in the small design are smaller that in the large design.

	Simulation (N)	Mean Data (N)
small repulsive	2.82	2.53
small attractive	2.82	2.57
large repulsive	2.72	2.74
large attractive	2.75	2.76

Table 8: Peak force generation of the separate Halbach segments in the different designs resulting from the ANSYS simulation and the measured data.

This error results in the RMSE of the small designs to fall just outside of the reassembly error of the measured data. For the large design it falls within the reassembly error.

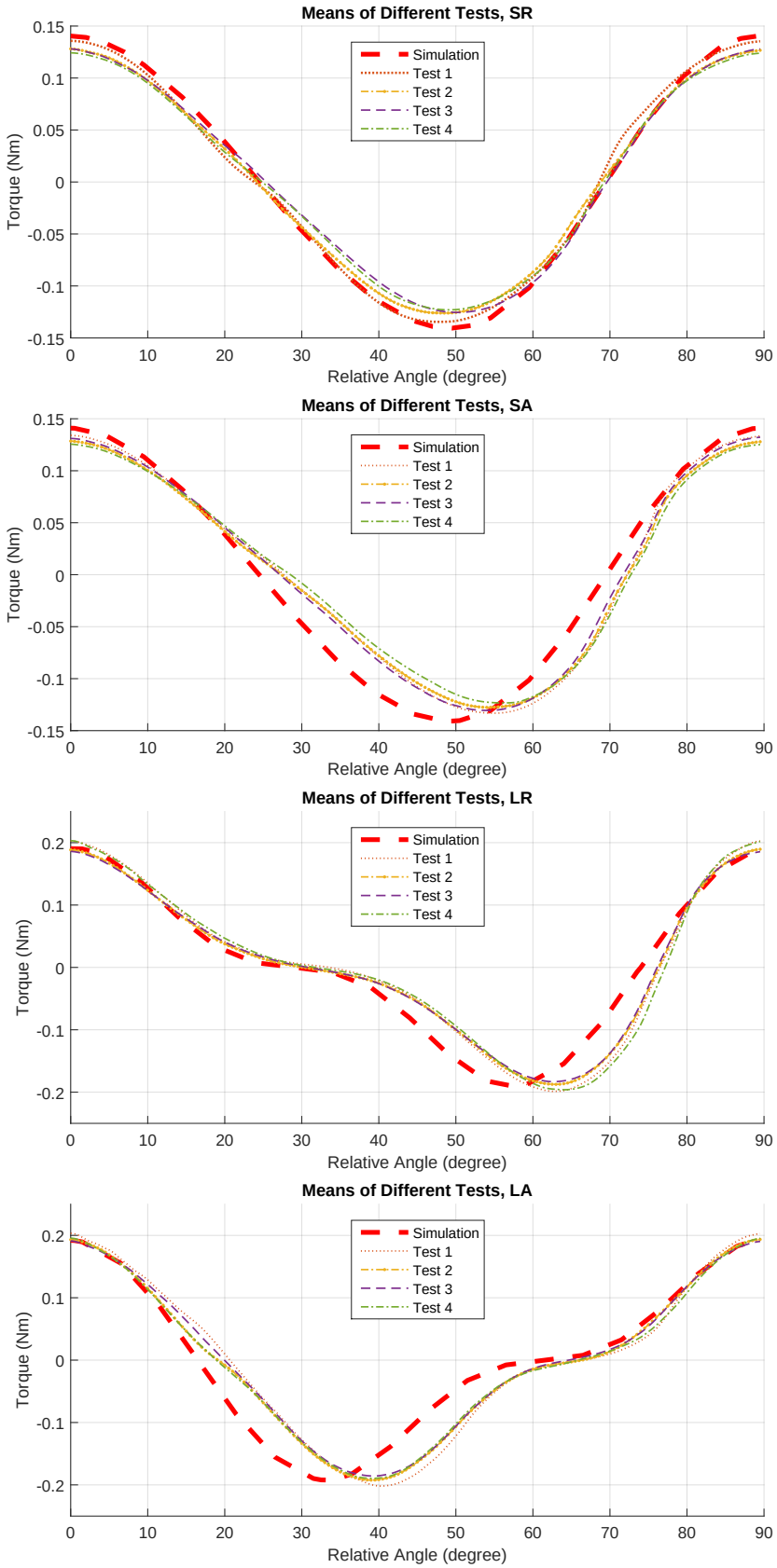

Figure 39: Means of different tests for different designs plotted together with the simulation data.

8.6 Axial Forces

The external part of the mechanism will create an axial force due to the repulsive and attractive forces on the external part. This force has no resultant on the external part because the two internal parts are generating the same force onto both sides of the external part thereby canceling each other (theoretically). The force will be highest when the torque is lowest since the inner and outer poles are directly aligned in this position. Figure 40 shows the axial forces as a function of the relative angle, with 0^o at the peak torque.

When looking at the peak forces, it is clear that the attractive designs create the highest values when aligned. The figure also shows that the large designs have a dip around the 30^o angle difference, which is the result of the gap between the magnets in the inner part of the mechanism.

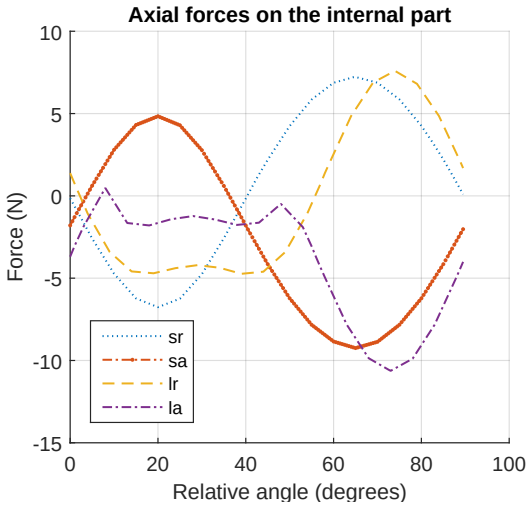

Figure 40: Axial forces of the internal part of the mechanism, simulated in ANSYS. The peak of the torque is at zero degrees so the relative angles are corresponding to the 90-degree turn data. Positive force is a repulsive force between the internal and external parts.

9 Discussion

The discussion follows the layout of the chapters of the report.

9.1 Requirements

The required torque has a distinct correlation to the fin ray angle. The torque needed for the motion was expected to be mostly the result of the drag of the water on the fin. This would express itself as a torque proportional to the square of the angular velocity of the fin $\dot{\theta}_f^2$. Interestingly, only the first fin ray shows a standard drag-based torque-position correlation. The following fin rays show a more parallelogram shaped position-torque graph where the highest torque is required during the start of the motion at the maximum amplitude of the fin ray (Fig 4). Even though the first fin ray has a different position-torque correlation than the other fin rays, the peak torques are not significantly different, so no increased torque requirement is needed.

An interesting find in the amplitude-force graph is that the torque runs from the peak torque at one maximum amplitude past zero torque to the opposite maximum. This indicates that the actuator has to actively slow down the motion of the fin ray. This result might be caused by the actuators back emf.

The torque of the individual fin rays are influenced by each other due to the fin material that connects them. This means that the fin rays will pull on each other when the material of the fin is pulled tight. This is possibly the cause of the slight variation of the data from the theoretical linear correlation between the amplitude and the torque.

The torque is calculated by multiplying the power use of the separate fin rays with the torque constant of the actuator and the efficiency of the gears. This means that the friction of the seal as well as drag and friction of the gears rotating in the water are not taken into account. The actual required torque might therefore be lower than is proposed in the requirements. The possible back emf is also not included in this result. These additional inefficiencies will only reduce the required maximum torque. The shape of the fin ray position-to-torque graph will remain similar.

9.2 Propulsive Mechanism Type Selection

Figure 41 shows the positions of the hull for the different mechanism types. The reluctance actuator is positioned the furthest towards the power source. This is misleading since the reluctance actuator does not have a transmission and would require a block diagram without it.

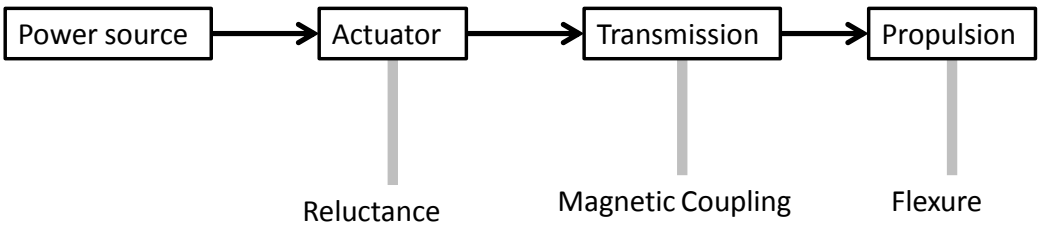

Figure 41: Block diagram of the powertrain of a bio-inspired UV with the different hull positions of the proposed mechanisms.

Type Specific Discussion

The reluctance actuator has the benefit over the transmission-type mechanisms that it is a stand-alone mechanism. There are no additional friction losses due to mechanical connections to an electric motor.

Since it does not require an additional actuator and gearing, the weight that is stated in the requirements is allowed to be higher compared to the transmission-type propulsive mechanisms.

The reluctance actuator requires an mmf that will be in the range of 5000 A-turns. This means that the bundle of windings from the coil will have a conductive surface of around 1000 mm^2. Since the allowable width of the mechanism size per fin is only 3 cm, this would complicate the fitting of this large coil. The large volume of the coil and the required paramagnetic material together also add around 500 g per fin ray to the vehicle, over three times the requirement of 150 g. Even without the mass of the actuators and gears that the transmission-type mechanisms require, the weight is still double that of the requirements. The reluctance actuator has no possibility to create a single drive system to reduce this weight, while both transmissions do. In comparison, the weight of the magnetic coupling and the flexure joint will be approximately 20 g and neglectable weight, respectively, with the weight of one actuator and gear per fin ray of139 g.

Instead of an electromagnet, the actuator could also be driven by sliding a permanent magnet through the paramagnetic path. The mmf that is created by a strong permanent magnet is much greater than a small electromagnet of the same size could deliver, which could also reduce the weight.

The calculations done for the reluctance actuator are estimates that assume perfect conditions. This is not the case in normal applications. This method is used because the largest complication was expected to be the strength of the electromagnet. If the strength of the electromagnet is insufficient under ideal circumstances, it will still be insufficient when inefficiencies are introduced.

The magnetic coupling design that is used to estimate the torque properties generates only 10 % of the required torque. This is due to the small magnet that is used in this example. Because the mmf that the magnet produces is linearly dependent on the length of the magnet, the magnetic field can be easily increased.

An analytical approach is used for the simulation of the magnetic coupling. The magnetic coupling design has, like the reluctance actuator, been simulated using perfect assumptions. The design of the coupling had to be simple to allow an analytical solution.

The rotational flexure joint calculations indicate that the flexure thickness, depending on the material, must be 20 to 20000 times larger than the length of the flexure. This is based on a maximum deflection of 10 % of the flexure length due to the pressure difference of 3 bar. This unrealistic result is caused by the equations that are combined. A large rotation of the fin ray while remaining below the fatigue strain and a small deflection due to the pressure difference is not possible with a homogeneous compliant material.

The translational flexure results show that the displacement of the fin ray and the deflection of the flexure due to pressure difference is quadratically related. This design can therefore also not be used for both fin deflection and pressure resistance.

The analytical method that is used again requires perfect assumptions. The analytical approach does create the possibility to investigate all dimensions of the flexure at once.

Both flexure joint designs fail to resist the pressure of the water when diving to the required depth. This is not surprising due to the high compliance that is needed to achieve the large rotation of the fin ray. A solution to this problem would be to eliminate the pressure difference by filling the hull with oil. If the environmental pressure increases, the pressure in the vehicle will also increase, resulting in equal pressure inside and outside the vehicle. This will allow the flexure material to be highly flexible which reduces the chance of fatigue failure. It does however increase the complexity of the fabrication and possibly drag on the internal mechanics of the vehicle. The vehicle will also not be able to carry pressure sensitive components.

Another way to eliminate the pressure difference would be to remain at the surface. This is not useful for the subject of this research, but would allow this solution to be applied elsewhere.

Comparison

Table 9 shows the three propulsive mechanism types that are investigated in Chapter 4. The mechanism types are graded on the objectives that are valued by importance. The total score is the sum of the individual score multiplied by the value of the objective.

Objective	Value	Reluctance	Magnetic	Flexure
Maintenance	3	5	5	5
Torque Production	3	3	5	5
Robustness	3	4	5	4
Pressure Resistance	2	5	5	3
Debris Collection	2	4	4	5
Ease of Fabrication	2	3	5	4
Energy Efficiency	2	4	5	4
Low Cost	1	3	5	5
Availability	1	3	4	4
Size and Weight	1	1	5	5
Total score	100	75	97	88

Table 9: Qualitative comparison of the designs.

The comparison table shows a number of interesting gradings that follow from Chapter 4. Grades lower than four will be discussed shortly.

The torque production of the reluctance actuator is too low. The only possibility to increase the torque is to enlarge the mechanism or use superconducting materials. Either solution is not considered manageable for this application.

The pressure resistance of the flexure has a value of three, due to it not being pressure resistant when using atmospheric pressure in the vehicle. If pressure would be allowed to increase internally, it can be made pressure resistant.

The fabrication of the reluctance actuator will cause difficulties. The shapes of the different designs are not complex, but integrating them in the hull while maintaining a small gap will create intricacies. In addition, the reluctance actuator requires specially fabricated parts made of paramagnetic material, which will increase cost. The reluctance mechanism therefore also scores low on both the low cost and the availability objectives.

The weight of the reluctance actuator is too high. Since this is over two times the requirement of 150 g (when excluding the actuator and gear), the reluctance actuator receives a one for the weight and mass objective.

For the most part, the magnetic coupling and the flexure joint are similar. Both would have similar internal mechanisms on actuating the fins, with the difference that the flexure design is connected directly to the fin and the magnetic coupling is connected via permanent magnets.

The important difference between the flexure and the magnetic coupling lies in where the failures may occur:

- The *magnetic coupling* is most likely to have a failing bearing that supports one of the fin rays. If this would cause a jam of the fin ray, the magnet coupling would slip and allow the actuator to continue its rotation. If the bearing failure would result in play of the fin ray, it could cause the fin ray to rub against the hull, possibly resulting in a leak.

- The *flexure joint* is most likely to fail due to fatigue or puncture of the material. The mechanism inside the vehicle could also cause wear to the flexure. These failures are difficult to predict and will likely cause a hull breach. Next to that, the blockage of one fin ray (due to the environment) would result in blockage of the fin ray actuator or to the entire fin (when using a single actuator for all fin rays). Blocking the actuator can cause damage.

The benefit that the flexure has over the magnetic coupling solution is the lack of crevices. This could however be copied onto the magnetic coupling by adding a membrane that allows water to pass through. If this membrane is chosen correct, it will filter the water entering the crevices of debris that could affect the workings of the mechanism.

The magnetic coupling is chosen due to its lack of material fatigue, the possibility of incorporating a rigid hull, and the potential torque transference.

9.3 Magnetic Coupling Design Selection

The simulations are done on specific designs, so the same design types with different dimensions would result in different results. The results are however interpreted with that possibility in mind.

The moment-arm design creates the largest transferable torque of the designs as presented here. This is however partly due to the larger arm that the moment arm uses on the fin ray. The face-to-face design has the advantage over the moment arm that the torque can be increased by increasing the radius of the coupling since the scaling properties are predictable. The radius of the coupling has a approximate linear relation to the torque, with only small magnetic interference differences. The torque development will remain similar when scaling which will not be the case with the moment arm.

The maximal transferable torques show that the coaxial designs create a very low torque compared to the other designs. This is as expected since the coaxial designs have a large gap between the inner and outer magnets and a small radius compared to the other designs. The large gap could be reduced by implementing specifically designed magnets. The torque could also be increased by either elongating the coupling or increasing the radius. Both options have their own issues. The elongation is limited because the requirements only allow for 3 cm length. The increase in radius will always result in a larger radius than the face-to-face designs to reach comparable torques.

The moment-arm designs were found to create a radial force on the external axle. This radial force has a magnitude comparable to the rotational forces (Fig.42). This could possibly be reduced by redesigning the coupling, but due to the unaligned axis of the internal and external part of the coupling, this radial force will always be present.

Figure 42: Moment arm produces radial force on the external part of the coupling. Resultant force exerted by the axle is shown in gray.

The face-to-face designs also create noncontributing forces, but these are forces in axial direction. These forces also act on the internal part of the mechanism if the mechanism is correctly positioned. This is preferred because this is a controlled environment and the induced friction is not a loss of the torque transferred through the coupling. The noncontributing forces of the moment arm will act on the external part.

The coaxial design results in the lowest noncontributing forces. The design is in full equilibrium if the parts are perfectly aligned, because all forces are symmetrical and guided through the part that is holding the magnets.

The misalignment constant k_{m} found in Table 3 for the face-to-face designs is higher than that of the moment arm. This is because the face-to-face coupling has a larger flux through the main magnets than the moment arm. The advantage that the face-to-face has over the moment arm is that if the complete external part is shifted, the force will act in axial direction in the axle, while the moment arm will create a moment over the axle bearing (Fig. 43). The external part of the moment arm will have to be designed with low drag as well as high stiffness in both directions.

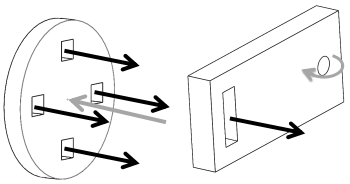

Figure 43: The face-to-face design will have a resultant force, while the moment arm will have a resultant moment as a result of misalignment. Resultant forces and moments exerted by the axle are shown in gray.

The moment arm has the smallest peak to peak play of the designs. This is however the result of the larger arm of the mechanism. Increasing the size of the other designs would allow for an increase in the number of magnets, which would also lower the play of these mechanisms.

The influence on the adjacent couplings will depend on the width of the couplings. Due to the Halbach-inspired orientation of the magnets, interference is greatly reduced. For the face-to-face and the moment arm, the influence on the adjacent couplings will act mostly on the internal part of the coupling since these are located next to each other. This will have low influence on the transferable torque since the external magnets are shielded by the internal magnets. The coaxial design will also have low interference due to the radial direction of the main magnetic field.

The results of the ANSYS simulation show that the face-to-face design has the most potential. The

coaxial design produces too little torque to reach the requirements without large mechanism diameters. Both the moment arm and the face-to-face design can generate enough torque, but they also create forces in noncontributing directions which will result in additional friction. The difference between the two is the direction and location of the noncontributing forces which are both favorable in the face-to-face design. The face-to-face design is therefore chosen to be used in the validation.

9.4 Validation

The intraclass correlation coefficients between the 90-degree turns of the different sessions were calculated to determine if the tests were reliable. The two lowest lower bounds of the 95 % confidence interval of all ICC's found are 0.79515 and 0.79736, all other lower bounds are above 0.9. Following the interpretation of Koo and Li 2016, two session data sets have 'good reliabilities' and all other session data have 'excellent reliability'. The intraclass correlation coefficients are shown in Appendix F.1 and determine that the tests done are reliable.

The reassembly error that follows from Figures 67 and 68 from Appendix F.2 indicates an error of up to 11 % for small, and up to 14 % for large designs. The larger outliers are the result of bad measurements, which are visible by the relatively large confidence interval of one session. These are disregarded for the determination of the reassembly error.

The reassembly errors are larger than expected. This is likely the result of the large number of actions required for reassembly which are prone to variation. Bolts can be fastened with different torque, the gears can be aligned different, or the load cell is positioned under varying stress. These errors can all be reduced by simplifying the assembly and increasing the design of the set-up.

The Pearson correlation coefficients are high, indicating a clear linear correlation.

The overall torques that are measured and compared using the regression line are all within the reassembly error. It is interesting that of all the overall torques, the largest difference is found in the small repulsive design. This is unexpected since this design has a centering force during peak torque and the small design has the lowest peak torque. A lower peak torque should reduce the stresses and strains in the set-up, causing less variations in the measurement. Since this large difference is caused by the first test, it is possible that the new parts are the cause of this. This is substantiated by the largest overall torques differences of the other designs, which all include the first test. It could easily be solved by running the set-up for a while when it is new.

The maximum difference between the means shows that the large attractive has the lowest differences compared to the other tests. This is interesting since during testing the large attractive design caused the most problems by jamming. The cause of this might be that the large attractive design has the lowest margin for error and requires a more precise reassembly to function correctly.

	RMSE (Nm)	**Allowed Error (Nm)**
Small Repulsive	0.0166	0.0155
Small Attractive	0.0159	0.0155
Large Repulsive	0.0180	0.0267
Large Attractive	0.0165	0.0269

Table 10: Root Mean Square Error between the simulation and the measured data, and the allowed error using the reassembly error.

The RMSEs between the simulation and measured data are close to the reassembly error for the small designs and well below the reassembly error for the large designs. The RMSEs are almost identical which indicates a more accurate simulation for the large than for the small designs. This is substantiated by the boxplot that displays the peak values. The simulation data of the small designs are all above the 50 percentile boxes, while the large design simulations fall within the 50 percentile boxes.

The plots of the simulated and mean data shown in Figure 39 show some interesting results. T

The phase difference between the troughs of the simulated and measured data is likely the result of the stepper motor skipping steps. When the mechanism approaches its peak transferable torque, the stepper motor also reaches its maximum. This results in the steppers skipping during the higher required torques.

Because the relative angle is directly reduced from the time data, a reduction in speed from the stepper results in an error in the angle. The small repulsive design does not show this error since the peak torques are lower. This should also be the case with the small attractive design, but the attractive forces likely cause extra friction requiring a higher driving torque by the stepper motor.

The saddle point in the torque graphs of the mean values is the result of the positions of the magnets and play in the set-up. The relative angle at which the saddle point occurs is always when the magnets of the external part pass the double pole of the secondary magnets in the internal part. This results in a change of torque direction. Because of the small play between the driving and the driven gear, the saddle point appears in the graph. This saddle point does not occur when the external magnets pass the main magnets, because at that point the change in direction is much more sudden. The saddle point in the large designs is more visible due to the lack of magnets between the Halbach segments.

The difference in torque between the large and small designs is not linear with respect to the difference in radius. This might be the result of the separation of the secondary magnets, which reduces interference. However, the ANSYS simulation shows the opposite effect. This might be the result of ANSYS having difficulty with this same-pole combination. It might also be the result of ANSYS not creating enough iterations to reduce the energy error. This would also explain why there is a difference in peak torques between the simulated and measured data of the small design.

Theoretically a difference between attractive and repulsive forces exists. This is due to the magnetic domains in the magnetic material slightly shifting. When attractive poles face each other, the magnetic fields of both magnets have a straightening force on the magnetic domains [23] (Fig. 44). If one of the magnets is turned so similar poles face, the orientation of the domains change slightly due to the repulsive force which reduces the magnetic forces acting on the two magnets.

The forces of the separate Halbach segments of the simulation are counterintuitive due to this theoretical difference between attractive and repulsive forces. It would be expected that the force creation of the small design would be lower than that of the large design, due to the interference of the closer same-pole magnets. The simulation shows the opposite of this. The forces created by the small design are higher than the large design. The measured data does show this as expected. This could be caused by ANSYS not being able to cope well with the close same-poles that are present in the small design. The flux change due to the changing orientation of the magnetic domains is possibly not integrated in ANSYS. The increase of force in the small design could then be the result of the double pole creating a higher field intensity. Since the large designs do not have the separate Halbach segments linked, this reduction is not present.

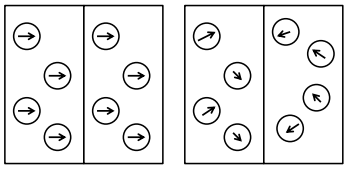

Figure 44: The orientation of the magnetic domains change when two magnets face with the same poles (exaggerated).

The differences that occurs between the simulation and the measured data of the small designs might be solved by using more iteration steps. The magnetic finite element method of ANSYS uses iteration steps to reduce the energy errors between the elements. Using more steps will reduce the error. During simulation of the designs, 40 steps were performed which reduced the energy error to approximately 1 %.

The axial forces of the small repulsive design show that at the peak torque all magnetic interactive force is used for torque (assuming perfect alignment). This could indicate that the continuous array of magnets increases efficiency of the coupling. A higher efficiency means that the transferable torque per Halbach segment would be higher. However, this is not the case in the measured data. The higher axial torque of the attractive designs during peak torque would cause an increase in friction, which could be the cause for skipping of the stepper motor.

The axial forces show the benefit of the repulsive designs. While the difference between the repulsive and attractive forces are not clear from only the torque, the axial forces show the higher friction inducing forces of the attractive designs. The attractive designs also induces friction on the external part of the mechanism due to the unstable equilibrium, while the repulsive creates a friction-reducing stable equilibrium force on the external part of the mechanism (Fig. 45).

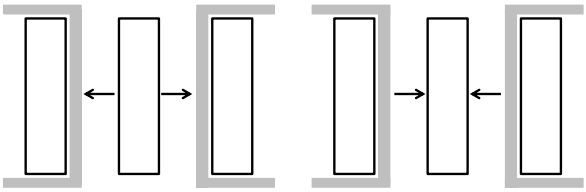

(a) Attractive forces create unstable equilibrium.

(b) Repulsive forces create stable equilibrium.

Figure 45: Forces on the external part of the mechanism (middle) during the peak torque transfer.

9.5 Future Work

The actual torque that each fin ray requires will be lower than stated in the requirements. The calculated force is an estimation based on the power usage and the properties of the motors and gears. This means that the losses due to back emf (occurring at the peak torque), seal friction, and additional gear friction is not measured. This could result in a lower torque requirement. The actual torque requirement could be determined using the magnetic coupling by measuring the angular difference.

When a vehicle is build, attention is needed for some parts of the design. First, the internal actuation mechanics must be chosen, either one actuator per fin ray or one actuator for an entire fin can be used. This will determine how the internal mechanics will be designed. Second, a change in power use of an actuator can be used as feedback to indicate possible damage to the fin or fin ray when knowing the regular power requirements. Third, the axial forces of the internal parts of the mechanism must be taken into account when designing the hull of the UV. These axial forces will occur in both directions along the axle, so must be supported in both directions. The radius of the coupling will allow this support around the axle. And finally, the radius of the coupling can be used to vary the hull thickness. By reducing the thickness of the hull only at the position of the magnets, the gap of the coupling can be decreased which will increase allowable torque.

A material that can filter debris will be required. The material will only need to stop the larger debris that might block the fin ray. The mesh size of the material must be chosen depending on the gap size between the external part and the hull. As long as the debris that passes through the membrane is smaller than the gap, it is unlikely to jam the fin ray. A durable fabric like denim could even be used.

9.6 Recommendations

A change in transferable torque of the magnetic coupling could be required depending on the application. The use of fin rays with different lengths, for example, would result in a different torque requirement. To accomplish this, a variation in radius is the best option. To increase the torque transfer, either an increase in radius of the mechanism or an increase of the magnetic field is possible. By increasing the magnetic field, either with larger magnets or by increasing the number of magnets, the axial forces will also increase. When increasing the radius of the coupling, the torque will increase while the noncontributing forces remain similar.

The repulsive designs create less friction between the internal and external parts of the mechanism in testing. During testing it was noticed that the attractive designs were more prone to jamming than the repulsive designs. This is most likely due to the increased friction that the attractive designs create during the peak torque it delivers. The repulsive designs create a centering force on the external part, thereby reducing the friction. Using spacers and bearings will reduce the chance of jamming and reduce the reassembly error.

Stronger steppers should have been used during the validation. The stepper motors started skipping steps during the validation, which caused the angular difference between the simulation and the measured data. This could have been prevented using stronger stepper motors or by measuring the angle of the internal part of the mechanism.

The test set-up should be more rigid. The test set-up was made to be used for both the small and the large designs. As a result the set-up required additional strengthening to increase the stiffness. Creating one set-up per mechanism size would simplify the reassembly and increase stiffness of the set-up.

Breakable fin rays could protect the main mechanics of the design. The magnetic coupling protects the mechanism and the mechanics in the motion plane of the fin ray. A force perpendicular to this motion could still cause damage to main parts of the vehicle. By using easily replaceable fin rays that bend or break during impacts perpendicular to the fin ray motion, possible repairs will be less costly.

10 Conclusion

This research indicates that to create a long-term-autonomous bio-inspired underwater vehicle, a magnetic coupling is a suitable solution to transfer kinetic energy through the hull. The standard practice of using dynamic seals to obstruct water from entering the hull will result in scheduled maintenance, limiting the duration for which the vehicle can operate autonomously. Other solutions investigated in this research are prone to fatigue or lack the ability to generate enough torque.

It is also concluded that a double-sided face-to-face magnetic coupling with Halbach-array-inspired magnet orientation creates the best transfer of torque. The increased magnetic field intensity that the Halbach-array-inspired magnet orientation induce allow for a stronger coupling through the hull. Using repulsive magnetic forces instead of attractive magnetic forces also reduces the friction of the external part of the magnetic coupling due to the centering forces.

11 Acknowledgment

With thanks to:

Dr. Ir. Chris Verhoeven for supplying the subject and his supervision of this research. Prof. Dr. Ir. Heike for her supervision of the research and aid in the report. Ir. Tim Vercruyssen for his input and supervision of this research. Dr. Jianning Dong and Dr. Davood Farhardi for their expert opinions.

12 Appendix

A Dynamic Seals

Dynamic seals are the used to obstruct fluids passing between two containers that are connected through an axle (Fig. 46). This appendix will present background information on the properties of dynamic seals. There are two main types of dynamic seals, friction and mechanical seals

Friction Seal

A friction seal is an elastomeric (most common, other materials are also possible) ring that is attached to the static part of a machine through which a shaft can turn or slide. The seal exerts pressure on the shaft to obstruct fluid from passing it and the resulting dynamic contact results in friction and wear. To reduce the amount of friction and wear, the seal can be lubricated. This is done by using either a lubricating grease or the medium that is obstructed by the seal.

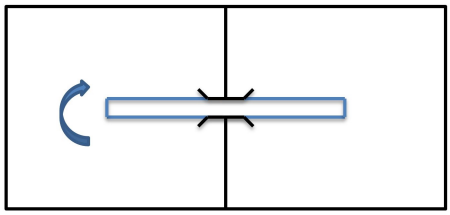

Figure 46: Schemetic representation of coupling between two containers using a dynamic seal.

Another common friction seal is packing, mainly used on ships and pumps. These packings consist of soft material compressed between a rotary shaft and the stationary housing. Because of the high friction and resulting heat production, these types of seals need intensive lubrication, which is achieved by leaking of the packing.

Friction seals will wear and as a result the machine will require maintenance. Friction seals rely on pressure exerted on the rotary shaft to obstruct fluid flow. The result is that when the pressure difference over the seal is increased, the force exerted on the shaft must also be increased, thereby increasing friction and wear of the seal.

Mechanical Seals

Mechanical seals have been designed as an alternative for packing. Mechanical seals consist of two seal faces, one is connected to the axle and the other to the stationary housing. The two components do not touch but allow a small fluid film to run between them. This fluid film is again either the fluid that is obstructed or a lubricant that is forced through.

To keep the leaking to a minimum, the fluid film must be very thin, requiring a high manufacturing and construction precision. The mechanical seal therefore does not allow misalignment of the shaft, and impacts on the axle could result in damage to the seal.

Overall Performance

The use of dynamic seals is useful since it is a cost-effective and simple option, that works if small leakages are acceptable. Small leakage is a property of dynamic seals that can not be overcome [1]. The use of seals in aquatic environments that contain debris and dust could result in abrasive effect due to buildup. If maintenance is possible the seals can be cleaned of replaced, but without maintenance it is prone to leaking.

This suggest that the use of seals in a long-term-autonomous underwater vehicle is undesirable, since maintenance is required as a result of the seals. A long-term-autonomous UV will not be able to be removed from the water to be dried, or it would defeat its purpose. Neither will it be possible to remove the seals for cleaning or replacement.

In order to get around the use of seals, the complete mechanism must be changed. The seals serve the purpose of closing a hole through which mechanical forces are transported from the inside of the UV to the outside of the UV. In order for these seals to be removed, the hole in the hull must also be removed, resulting in a closed, continuous hull.

B Swimming Modes

Body/Caudal Fin Swimming

The body/caudal fin (BCF) swimming mode is defined by the use of the body- and caudal fin of a fish to create thrust. This mode can generate the most speed and is therefore mostly encountered in fish that swim in open water or fish that require high speeds [2, 16].

The high speed and large acceleration that are possible are the main benefits of this swimming mode and distinguishes the BCF swimming type from other swimming modes. The mode also allows for agile swimming, provided that the fish has forward momentum.

Though BCF swimming has high performance in one direction, the swimming mode is unidirectional. Agility is high (depending on the extend at which the body can be used for steering) provided the fish has speed, but this mode cannot be used to swim backward.

Median/Paired Fin Swimming

The median/paired fin (MPF) swimming mode includes all swimming modes that use fins other than the caudal fin to create thrust. This mode is mostly found in fish that reside in environments that require high manoeuvrability instead of high speeds, like murky waters with obstacles or crevices in underwater rock formations [2, 16].

The result of this mode is indeed a high manoeuvrability and multi-directional swimming capabilities. Since only the fins move, there is also a reduction in the inertia of the motion relative to the BCF swimming mode. The undulating motion that is created by the fins is a result of simple oscillations by the fin rays composing the fins.

MPF swimming in nature is mostly slower than BCF swimming, although fish with more muscular fins like rays can reach high speeds. When looking at the biomimetic fish, there is no clear difference in speed between the BCF and the MPF swimming mode.

Jellyfish / Tentacle

Though jellyfish and squids (tentacles) are very different animals, their swimming technique is similar. Both animals have a slow relaxation stage that allows water to flow into its so called “bell”, after which a contraction stage produces a jet of water. Close examination shows that the squids tentacles have an inter-tentacle membrane at the body of the squid. Sfakiotakis et al. 2014 showed that this membrane has a large impact on the creation of the jet during contraction.

Once the bell shape is optimized, the swimming mode is very simplistic but efficient [41], which is possibly why a brainless animal like the jellyfish uses this swimming mode.

This propulsion technique has a downside which is that it is a one-directional propulsion. This can also be seen when looking at the biological users. The squid uses this propulsion as a defensive flight action [33] and jellyfish do not require a precise positioning swimming mechanism. The swimming type also has no reverse swimming capabilities.

Flapping Foil

The flapping foil propulsion uses an oscillating foil to create thrust, similar to a BCF swimmer when only the caudal fin is used (called thunniform swimming). The wing has a slight angle for each direction in order for the water to be displaced backwards and create vortices. The swimming mode can also be found in sea turtles which use their legs as flapping foils.

The motion is an oscillation of a foil, using tipping of the foil to create a directional lift and a water jet. The up and down motion could be used to actuate the tipping of the foil. This mechanism is found to create propulsive efficiencies of up to 70 % [8, 30].

The foil requires a coordinated tipping correlated to the up and down movement, which is essential for the thrust and efficiency [8]. This tipping could be a difficult task, since the tipping mechanism is exposed to the environment. The water flow around the vehicle might also interfere with the efficiency of the mechanism. To reduce this the foil must be extended which makes it more vulnerable.

Webbed Feet

Ducks and most other amphibian animals use webbed feet for their aquatic propulsion. The mechanism relies on the directional dependent drag of the feet. The feet are folded open (increasing drag) when pushing forward and folded in (reducing drag) during the returning phase.

Since this propulsion mechanism is a secondary function of the feet, it could be concluded that it is not highly efficient, though knowledge about this is insufficient. The lack of the water jet creation, which can be found in all previously mentioned swimming modes and which is characteristic for aquatic animals, also indicated a reduced performance.

B.1 Selection Criteria

In order to reduce the amount of propulsion choices, assessment criteria have been set. These are independence, availability, and performance. The possible modes will be assessed in this section based on functionality in biomimicry, not on functionality in biology.

Independence

This criterium is based on the likely-hood of this propulsion to require assistance from humans to persevere. This criterium can be applied to both the fins and the driving mechanism, but the reasons that attribute whether to pass this criterium are different. In the case of the fins for instance, it is important not get stuck, while for the mechanism it would mean that there is no refilling of a hydraulic fluid container needed. This section is dedicated to the swimming modes and will therefore only be assessed.

Availability

Not all designs of the propulsion principle shown here are known designs. Some have not been tested or created before, so there is no general knowledge about their propulsive performances. Therefore, the availability criterium has been introduced to test whether the mechanism is readily available to be implemented with comparable validated data.

Performance

The performance of the different swimming modes is important when choosing a design. A lack of speed could result in the vehicle being swept away with possible currents. A low efficiency will reduce the operating range of the vehicle.

Comparison

The clear difference that can be found in nature has, however, not been accomplished in the biomimetic or biomechanical creations. As can be concluded from literature, there is no clear distinction in between different forms of swimming on the basis of speed. This suggests that though the knowledge about the mechanics of fish locomotion is high, the ability to recreate efficient swimming is still lacking.

	Independence	Availability	Performance
BCF	+	+	+
MPF	+	+	+
Jellyfish / Tentacle	+	+	+
Flapping Foil	0	+	+
Duck Feet	+	0	-

Table 11: Comparison of different swimming modes.

When looking at the basic principles of the swimming modes, all biological modes can be reduced to an oscillating motion. Looking closely at the mechanics of biological fish, even the complex modes like

BCF swimming is a chain of oscillating vertebra. This means that when an actuation mechanism will work for one of these swimming modes, it could, with adaptations, be implemented in all swimming modes.

From the Table 11 it is clear that the swimming modes BCF, MPF, and Jellyfish/Tentacle have the same score. MPF swimming allows for a steady, large platform to place mechanics, sensors and batteries. Adding to that, that within the TU Delft there is expertise on the MPF swimming mode, specifically cuttlefish (Rajiform) swimming, this is the obvious choice.

C Other Solutions

C.1 Soft Hydraulics

Only “soft” hydraulics will be assessed in this research, since “hard” hydraulics still involves the use of seals to keep the hydraulic fluid inside the system and under pressure. Soft hydraulics use flexible material with chambers that can be filled with hydraulic fluid to create strain [12] (Fig. 47a).

The largest benefit of soft robotics, which is that they have a compliant interaction with their environment [27], is not useful in this application. The fins do not have to be soft since the motion of the fin will not be touching or grabbing any fragile materials or will not have the force to do more than nudge anything it will hit.

Leaking is a large downside of using soft hydraulics [22]. Soft hydraulics is actuated as a result of the creation of stresses in the material, which will result in fatigue. This fatigue can be reduced by reducing the stress on the material during the motions. The reduction of stress in the material will mean that the volume difference must be reduced, allowing smaller chambers and resulting in a larger friction of the fluid flow. The larger friction will result in a slower motion [22].

A hydraulic system relies on pressure differences, meaning that diving will influence the performance of the vehicle. The pressure difference between the inside of the hydraulic system and the environment is what creates the movement of an hydraulic actuator. If the environmental pressure increases, the hydraulic pressure must also increase to create the same order of extension. This requires a more powerful pump that increases pressure in the order of the environmental pressure increase.

C.2 Stator-Rotor

The Stator-Rotor mechanism uses the gap between the rotor and the stator of a brushless rotational electric motor to position the hull (Fig. 47b). The stator, which includes the coils of the motor, will be positioned within the hull and the rotor will be subjected to the environment and connected to the fin.

The difficulty with this type of hull penetration is that the torque production of an electric motor is highly dependent on the distance between the stator and the rotor [24]. Implementing a hull would increase the distance and lower the torque. Combining this with the small volume requirement results in low output torque and the need for a gearing between the motor and the fin. Since the hull will be constructed between the stator and rotor, the gearing will be subjected to the environment.

Using a motor with a high enough torque would violate the mechanisms size requirement and would also increase the cost of each vehicle significantly.

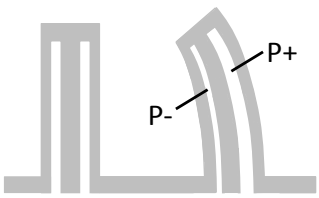

(a) Schematic representation of the soft hydraulics solution. A pressure difference in between the two chambers will cause the compliant material to turn deform.

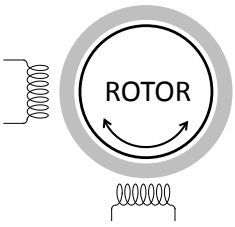

(b) Schematic representation of the stator-rotor solution. The rotor will rotate in the external environment, the coils are positioned inside the vehicle.

Figure 47: Simplified examples of the different mechanisms, the hull position is represented in gray.

D Drawings

D.1 Magnetic Coupling

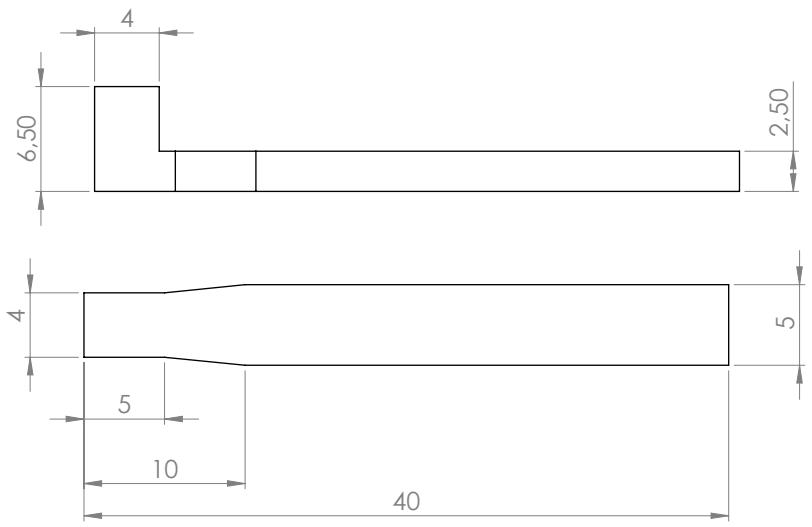

Figure 48: Dimensions of the flux guidance connected to the magnet from Figure 10a. Dimensions in mm.

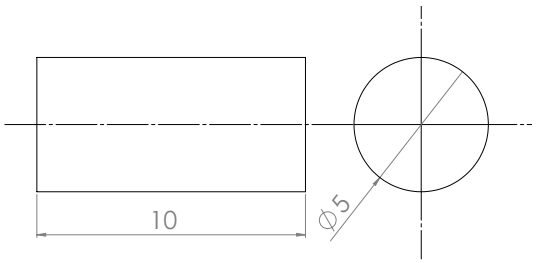

Figure 49: Dimensions of the flux guidance connected to the fin ray from Figure 10a. Dimensions in mm.

D.2 Experimental Set-up

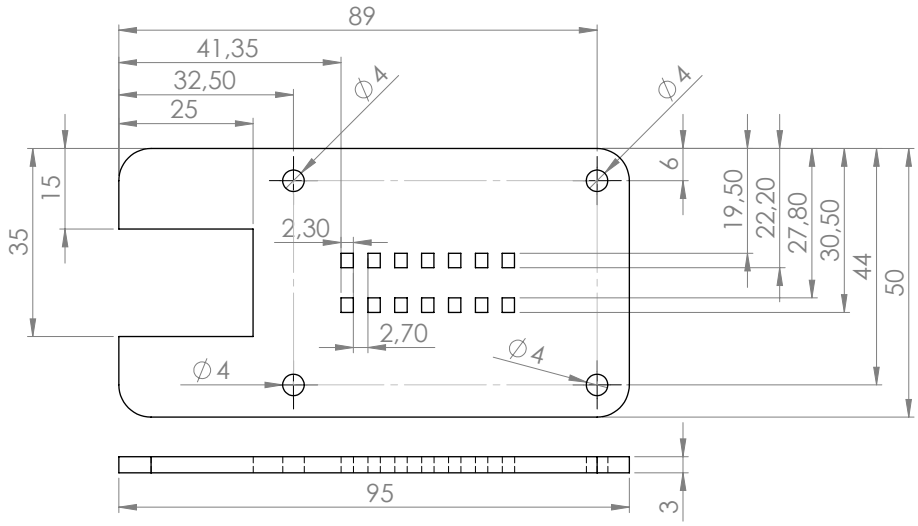

Figure 50: Dimensions of the top and bottom plate of the parameter estimation set-up from Figure 18. Hole dimensions in the centre are repetitive. Dimensions in mm.

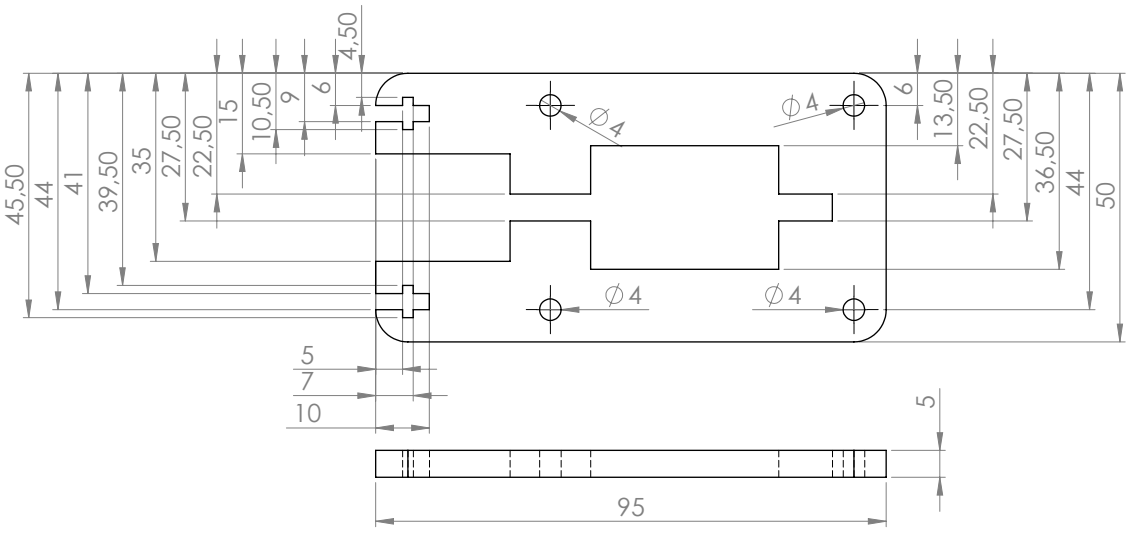

Figure 51: Dimensions of the middle plate of the parameter estimation set-up from Figure 18. Dimensions in mm.

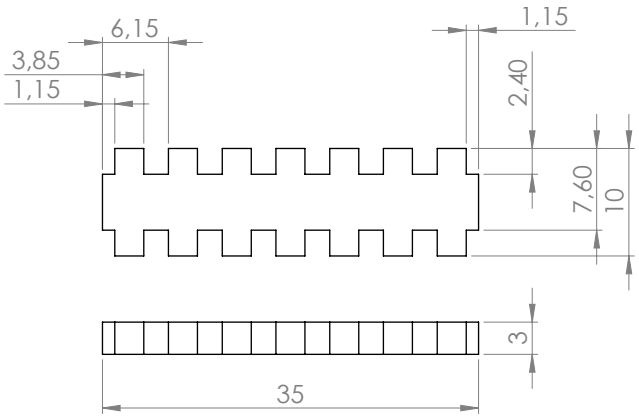

Figure 52: Dimensions of the magnet guiding wall of the parameter estimation set-up from Figure 18. Teeth dimensions are repetitive. Dimensions in mm.

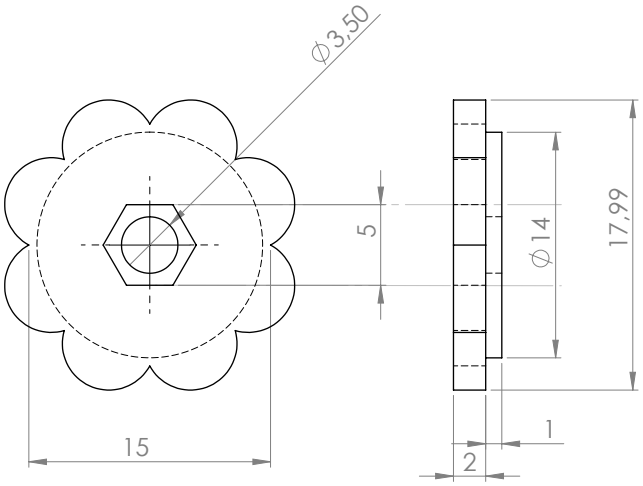

Figure 53: Dimensions of the turning knob of the parameter estimation set-up from Figure 18. Dimensions in mm.

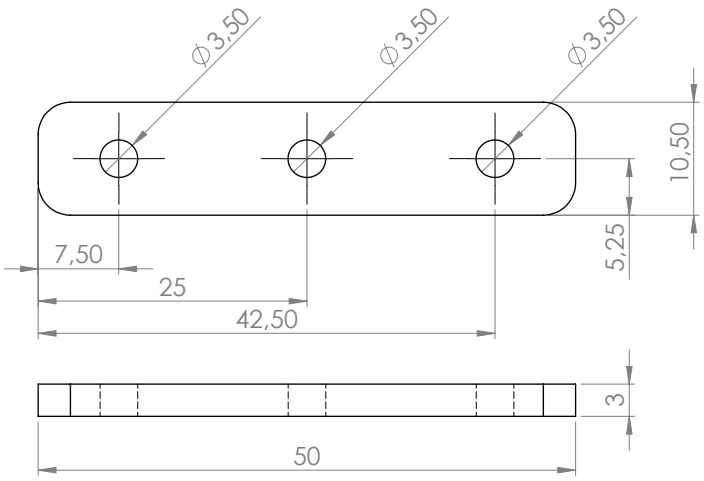

Figure 54: Dimensions of the tension bar of the parameter estimation set-up from Figure 18. Dimensions in mm.

D.3 Magnetic Coupling Designs

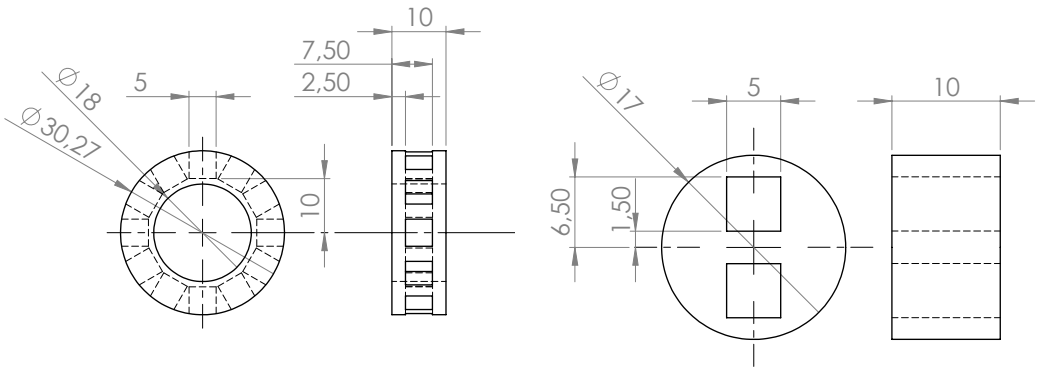

(a) Dimensions of the external part of both coaxial designs. Dimensions in mm.

(b) Dimensions of the internal part of both coaxial designs. Dimensions in mm.

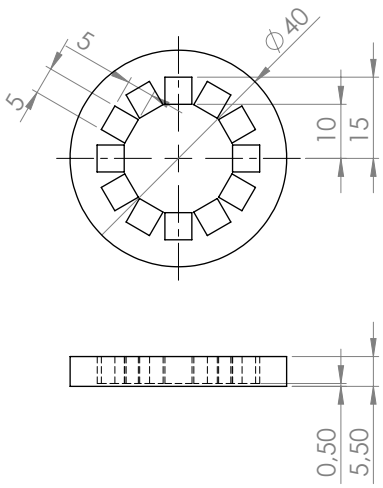

(a) Dimensions of the internal part of both face-to-face designs. Dimensions in mm.

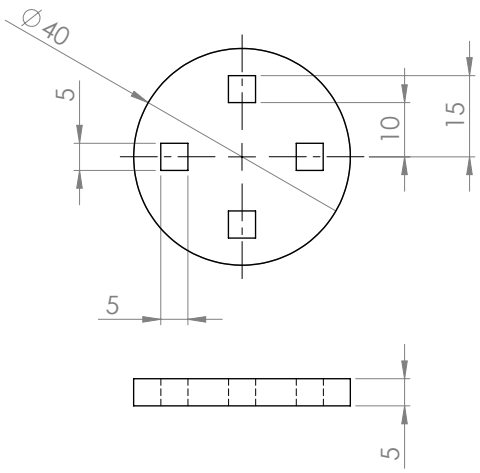

(b) Dimensions of the external part of both face-to-face designs. Dimensions in mm.

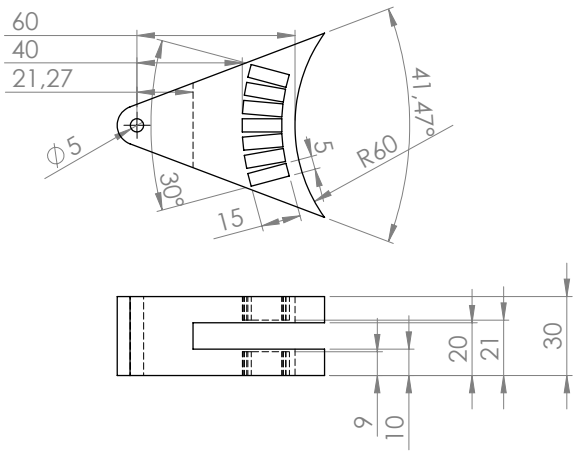

Figure 57: Dimensions of the internal part of attractive moment-arm design. Dimensions in mm.

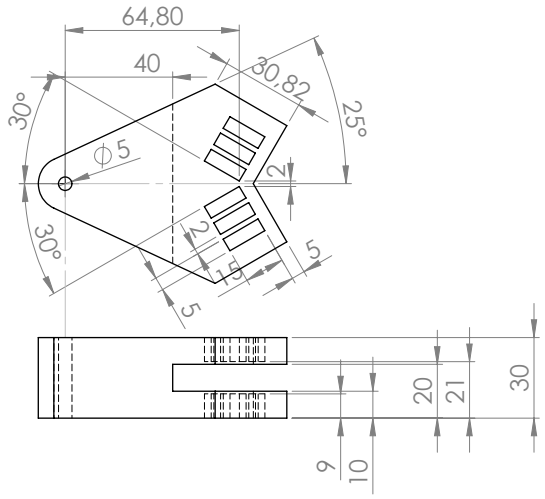

Figure 58: Dimensions of the internal part of repulsive moment-arm design. Dimensions in mm.

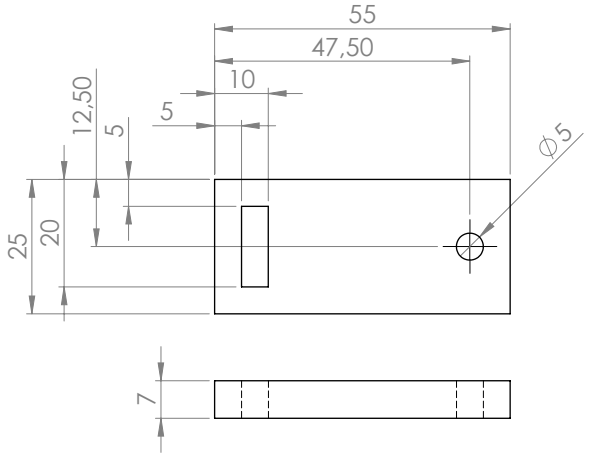

Figure 59: Dimensions of the external arm for both moment-arm designs. Dimensions in mm.

D.4 Design Validation

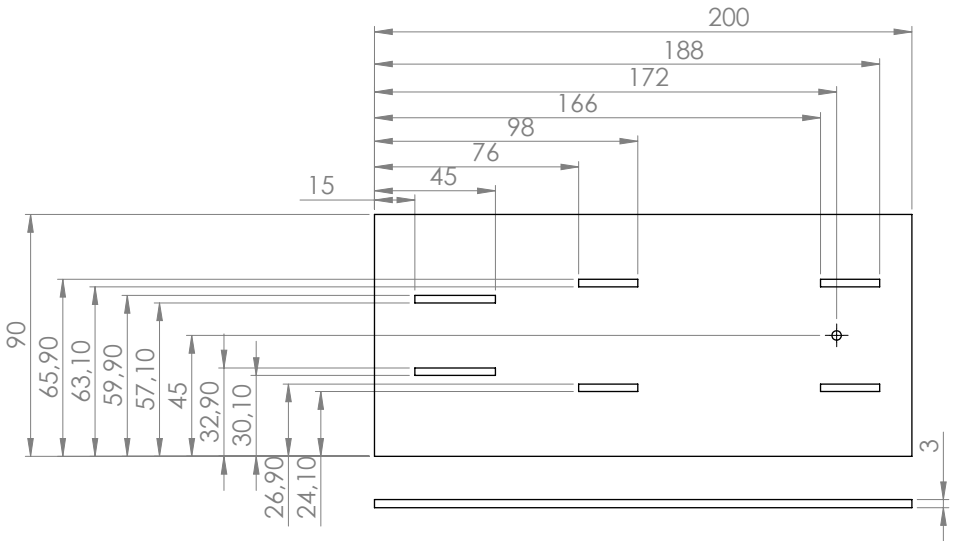

Figure 60: Dimensions of the base of the validation set-up from Figure 34. Dimensions in mm.

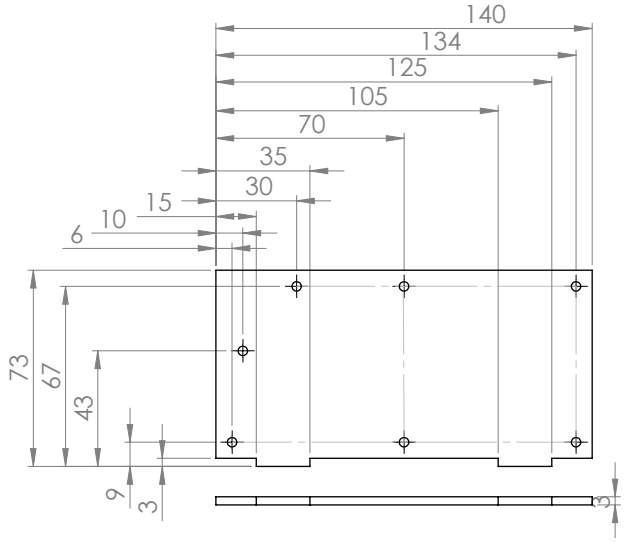

Figure 61: Dimensions of the side wall of the validation set-up from Figure 34, two are required. Dimensions in mm.

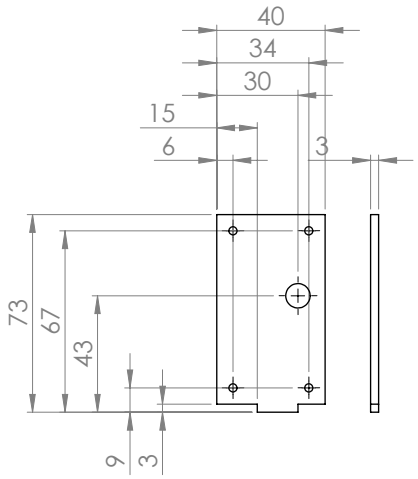

(a) Dimensions of the side wall on which the stepper motors are mounted of the validation set-up from Figure 34, two are required. Dimensions in mm.

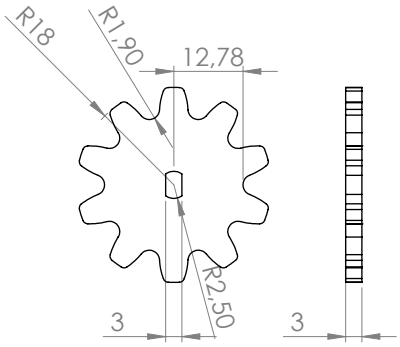

(b) Dimensions of the driving gear positioned on the stepper motors from Figure 34, two are required. Dimensions in mm.

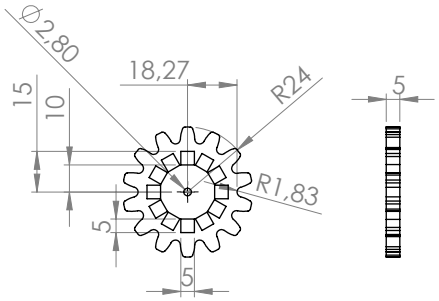

(a) Dimensions of the small internal part of the validation set-up from Figure 34, two are required. Dimensions in mm.

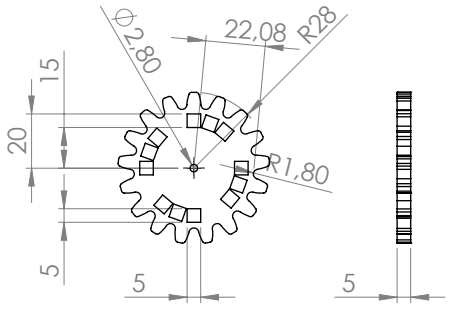

(b) Dimensions of the large internal part of the validation set-up from Figure 34, two are required. Dimensions in mm.

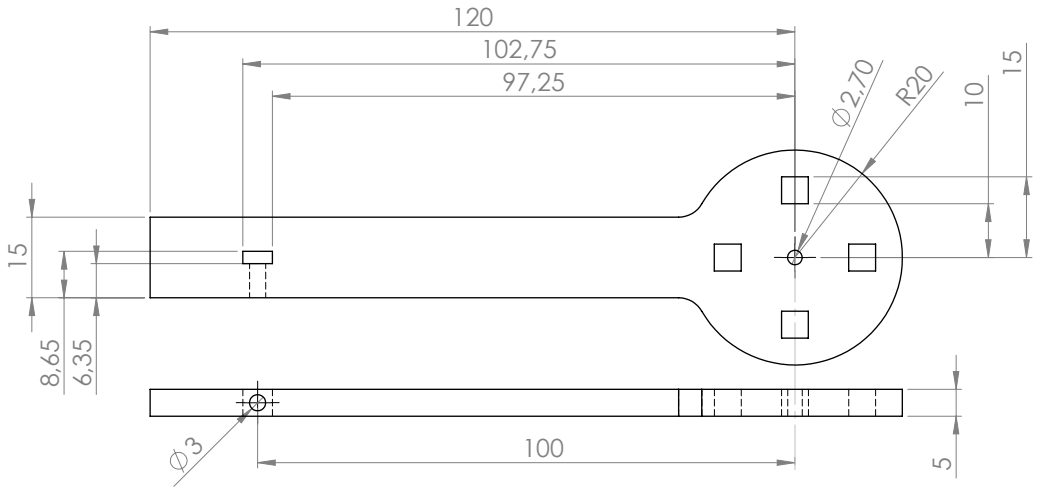

Figure 64: Dimensions of the small external part of the validation set-up from Figure 34. Dimensions in mm.

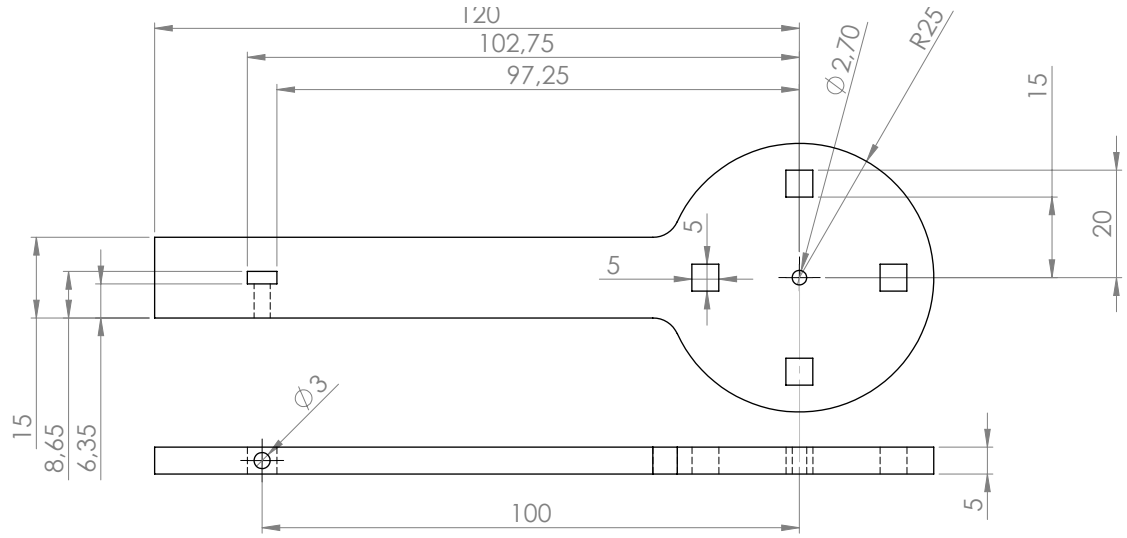

Figure 65: Dimensions of the large internal part of the validation set-up from Figure 34. Dimensions in mm.

E Arduino

E.1 Arduino code

```
/*      Stepper controller for validation test
*
*      controls two stepper motors using 3 switches
*      one switch turns both stepper motors, the two other switches turn the two steppers individually in order for lining up the driving gears
*
*/




// defines pins numbers
const int XstepPin = 2;
const int YstepPin = 3;
const int XdirPin = 5;
const int YdirPin = 6;
const int enablePin2 = 7;
const int enablePin1 = 8;
const int Push1 = 9;
const int Push2 = 10;
const int Push3 = 11;

volatile boolean Push1in;
volatile boolean Push2in;
volatile boolean Push3in;

long Push1time = 0;
long Push2time = 0;
long Push3time = 0;
long debounce = 20;   // the debounce for differentiating noise and pin push

long loopstart;
long wait;
int pulse = 1;

const double turns = 2.5;     // # of turns of the coupling
const double driven = 17;     // teeth ratio of testing  large
//const double driven = 14;     // teeth ratio of testing  small
const double drive = 10;     // teeth ratio of testing small

const double timeout = 3000;
int delaytime;

void setup() {
  Serial.begin(9600);       // open the serial port at 9600 bps:

  // Sets the two pins as Outputs
  pinMode(XstepPin,OUTPUT);
```

```
48   pinMode(YstepPin,OUTPUT);
49   pinMode(XdirPin,OUTPUT);
50   pinMode(YdirPin,OUTPUT);
51   pinMode(enablePin1,OUTPUT);
52   pinMode(enablePin2,OUTPUT);
53   pinMode(Push1,INPUT);
54   pinMode(Push2,INPUT);
55   pinMode(Push3,INPUT);
56
57   digitalWrite(XdirPin,HIGH);
58   digitalWrite(YdirPin,HIGH);
59
60   digitalWrite(enablePin1,HIGH);
61   digitalWrite(enablePin2,HIGH);
62 }
63
64 void loop() {
65   loopstart = millis();
66
67
68  // check double button press
69   if (digitalRead(Push3) == LOW){
70     if (millis()-Push3time > debounce && !Push3in){
71       digitalWrite(enablePin1,LOW);
72       digitalWrite(enablePin2,LOW);
73       if (pulse<2048/drive*driven*turns){
74         pulse += 1;
75       }
76       else{
77         pulse = 1;
78         delay(1500);
79         if (digitalRead(XdirPin) == HIGH){          //change direction
               of actuation
80          digitalWrite(XdirPin,LOW);
81          digitalWrite(YdirPin,LOW);
82         }
83         else{
84           digitalWrite(XdirPin,HIGH);
85           digitalWrite(YdirPin,HIGH);
86         }
87       }
88     }
89   }
90   else{
91     Push3time = millis();
92     Push3in = false;
93   }
94
95
96   // check single button press
97     if (digitalRead(Push1) == LOW){
98       if (millis()-Push1time > debounce && !Push1in){
99         digitalWrite(enablePin1,LOW);
100        digitalWrite(enablePin2,HIGH);
```

```
101       }
102     }
103     else {
104       Push1time = millis();
105       Push1in = false;
106     }
107
108
109   // check single button press
110     if (digitalRead(Push2) == LOW){
111       if (millis()-Push2time > debounce && !Push2in){
112         digitalWrite(enablePin2,LOW);
113         digitalWrite(enablePin1,HIGH);
114       }
115     }
116     else {
117       Push2time = millis();
118       Push2in = false;
119     }
120
121        digitalWrite(XstepPin,HIGH);
122        digitalWrite(YstepPin,HIGH);
123        delayMicroseconds(100);
124        digitalWrite(XstepPin,LOW);
125        digitalWrite(YstepPin,LOW);
126        delayMicroseconds(timeout);
127
128   digitalWrite(enablePin1,HIGH);
129   digitalWrite(enablePin2,HIGH);
130
131 }
```

E.2 Connection Diagram

The numbers in the scheme correspond to the numbered Arduino I/O pins. Closing the switch connected to pin 9 will turn the upper stepper motor, closing the switch connected to pin 10 will turn the lower stepper motor, and closing the switch connected to pin 11 will turn both stepper motors

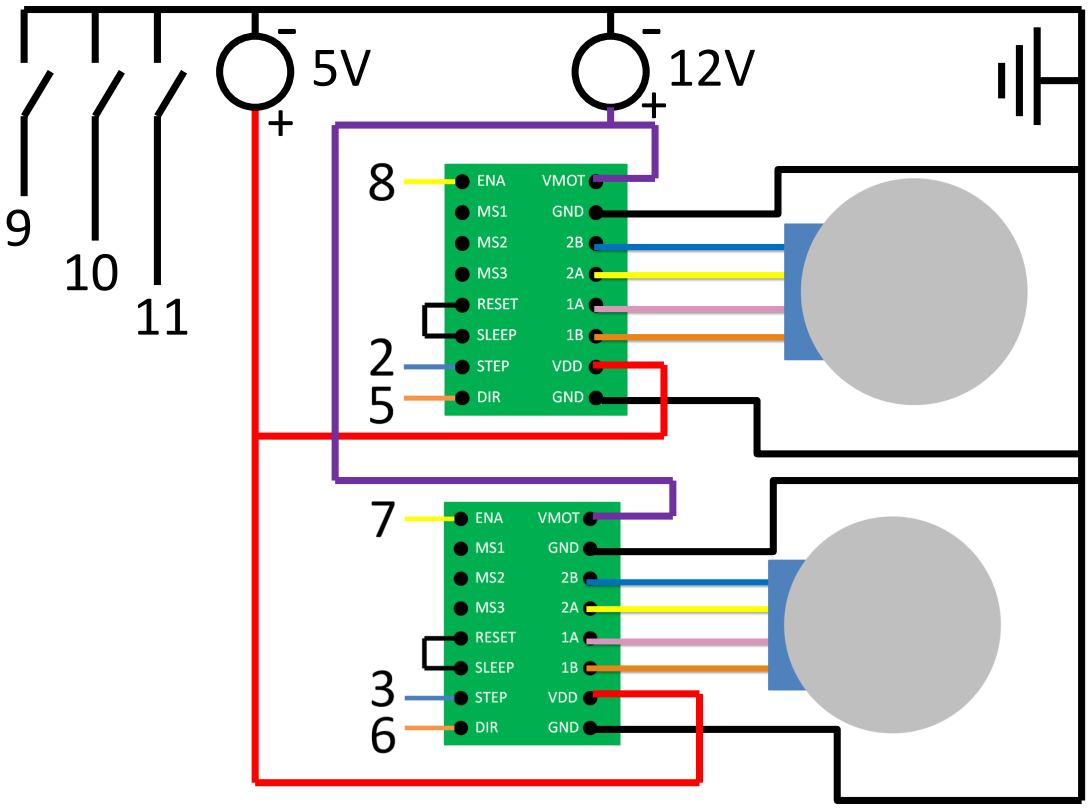

Figure 66: Connection scheme for connecting the stepper motors and switches to the Arduino. Numbers in the scheme are the numbers of the output pins of the Arduino.

F Detailed Validation Results

F.1 Intraclass Correlation Coefficient

	r	LB	UB	F	df1	df2	p	#
test1 large attractive session1	0.95773	0.94878	0.96587	635.4026	179	4860	0	28
test1 large attractive session2	0.96891	0.96235	0.9749	2307.5431	179	13140	0	74
test1 large repulsive session1	0.97759	0.97267	0.982	829.6752	179	3240	0	19
test1 large repulsive session2	0.94433	0.93288	0.95486	883.0683	179	9180	0	52
test1 large repulsive session3	0.96702	0.95992	0.97345	646.1689	179	3780	0	22
test1 small attractive session1	0.97745	0.97263	0.98183	2905.5585	179	11880	0	67
test1 small repulsive session1	0.99294	0.99139	0.99434	4926.9065	179	6120	0	35
test1 small repulsive session2	0.99206	0.99033	0.99363	5500.4696	179	7740	0	44
test2 large attractive session1	0.96791	0.9607	0.97431	302.5889	179	1620	0	10
test2 large attractive session2	0.97664	0.97163	0.98118	1965.9068	179	8280	0	47
test2 large attractive session3	0.98185	0.97792	0.9854	2002.352	179	6480	0	37
test2 large attractive session4	0.99217	0.99043	0.99372	3040.3864	179	4140	0	24
test2 large attractive session5	0.99003	0.98786	0.99198	6353.9243	179	11340	0	64
test2 large repulsive session1	0.97951	0.97512	0.98349	2964.8071	179	10980	0	62
test2 large repulsive session2	0.92111	0.90518	0.93583	351.2744	179	5220	0	30
test2 large repulsive session3	0.99026	0.98812	0.99218	3151.5814	179	5400	0	31
test2 large repulsive session4	0.97766	0.9729	0.98198	4596.0647	179	18720	0	105
test2 small attractive session1	0.98421	0.98074	0.98732	1434.3719	179	3960	0	23
test2 small attractive session2	0.97221	0.96626	0.97761	1225.5046	179	6120	0	35
test2 small attractive session3	0.98404	0.98062	0.98715	7832.9978	179	22680	0	127
test2 small attractive session4	0.98274	0.97905	0.98609	11158.4341	179	35100	0	196
test2 small repulsive session1	0.95396	0.94438	0.96272	1223.3631	179	10440	0	59
test2 small repulsive session2	0.98899	0.98661	0.99114	9521.1672	179	18900	0	106
test2 small repulsive session3	0.98396	0.98052	0.98708	7423.0611	179	21600	0	121
test3 large attractive session1	0.99266	0.99106	0.9941	10413.9259	179	13680	0	77
test3 large attractive session2	0.95513	0.94565	0.96375	575.692	179	4680	0	27
test3 large attractive session3	0.94021	0.92769	0.95163	315.4846	179	3420	0	20
test3 large attractive session4	0.92993	0.9155	0.94318	292.9899	179	3780	0	22
test3 large attractive session5	0.9486	0.93805	0.9583	2400.0803	179	23220	0	130
test3 large repulsive session1	0.98944	0.98712	0.99152	2810.83	179	5220	0	30
test3 large repulsive session2	0.95593	0.94679	0.96431	2170.0419	179	17820	0	100
test3 large repulsive session3	0.96805	0.96131	0.9742	2273.6412	179	13320	0	75
test3 small attractive session1	0.98338	0.9798	0.98662	3965.3378	179	11880	0	67
test3 small attractive session2	0.96825	0.96147	0.9744	1007.3807	179	5760	0	33
test3 small attractive session3	0.96653	0.9595	0.97294	3581.4792	179	22140	0	124
test3 small attractive session4	0.98145	0.97747	0.98506	4128.1205	179	13860	0	78
test3 small repulsive session1	0.99381	0.99247	0.99502	22320.5009	179	24840	0	139
test3 small repulsive session2	0.946	0.93496	0.95617	2383.6585	179	24300	0	136
test3 small repulsive session3	0.95261	0.94282	0.9616	1930.9283	179	17100	0	96
test4 large attractive session1	0.82639	0.79515	0.8563	110.4841	179	3960	0	23
test4 large attractive session2	0.93656	0.92369	0.94845	1093.4452	179	13140	0	74
test4 large attractive session3	0.95639	0.94734	0.96468	2259.7171	179	18360	0	103
test4 large attractive session4	0.93567	0.92263	0.94771	1062.7229	179	12960	0	73
test4 large repulsive session1	0.96863	0.96202	0.97466	3057.7985	179	17640	0	99
test4 large repulsive session2	0.9267	0.91192	0.94037	582.538	179	8100	0	46
test4 large repulsive session3	0.82825	0.79736	0.85783	121.5617	179	4320	0	25
test4 small attractive session1	0.95677	0.9473	0.96526	266.5601	179	1980	0	12
test4 small attractive session2	0.97677	0.97174	0.98131	1220.3279	179	5040	0	29
test4 small attractive session3	0.97152	0.96545	0.97703	1706.3514	179	8820	0	50
test4 small attractive session4	0.98514	0.98191	0.98805	2719.1157	179	7200	0	41
test4 small attractive session5	0.97938	0.97493	0.9834	1901.0298	179	7020	0	40
test4 small attractive session6	0.96569	0.95846	0.97229	1717.9582	179	10800	0	61
test4 small repulsive session1	0.98146	0.97749	0.98506	4870.8928	179	16380	0	92
test4 small repulsive session2	0.97106	0.96492	0.97665	1980.7563	179	10440	0	59
test4 small repulsive session3	0.98238	0.97856	0.98583	2008.2778	179	6300	0	36
test4 small repulsive session4	0.98859	0.98612	0.99082	7192.6142	179	14760	0	83

Table 12: Intraclass correlation coefficients for the 90-degree turns of the different sessions. The direction of actuation is negative and positive combined. Absolute agreement, single measures.

F.2 Reassembly Error

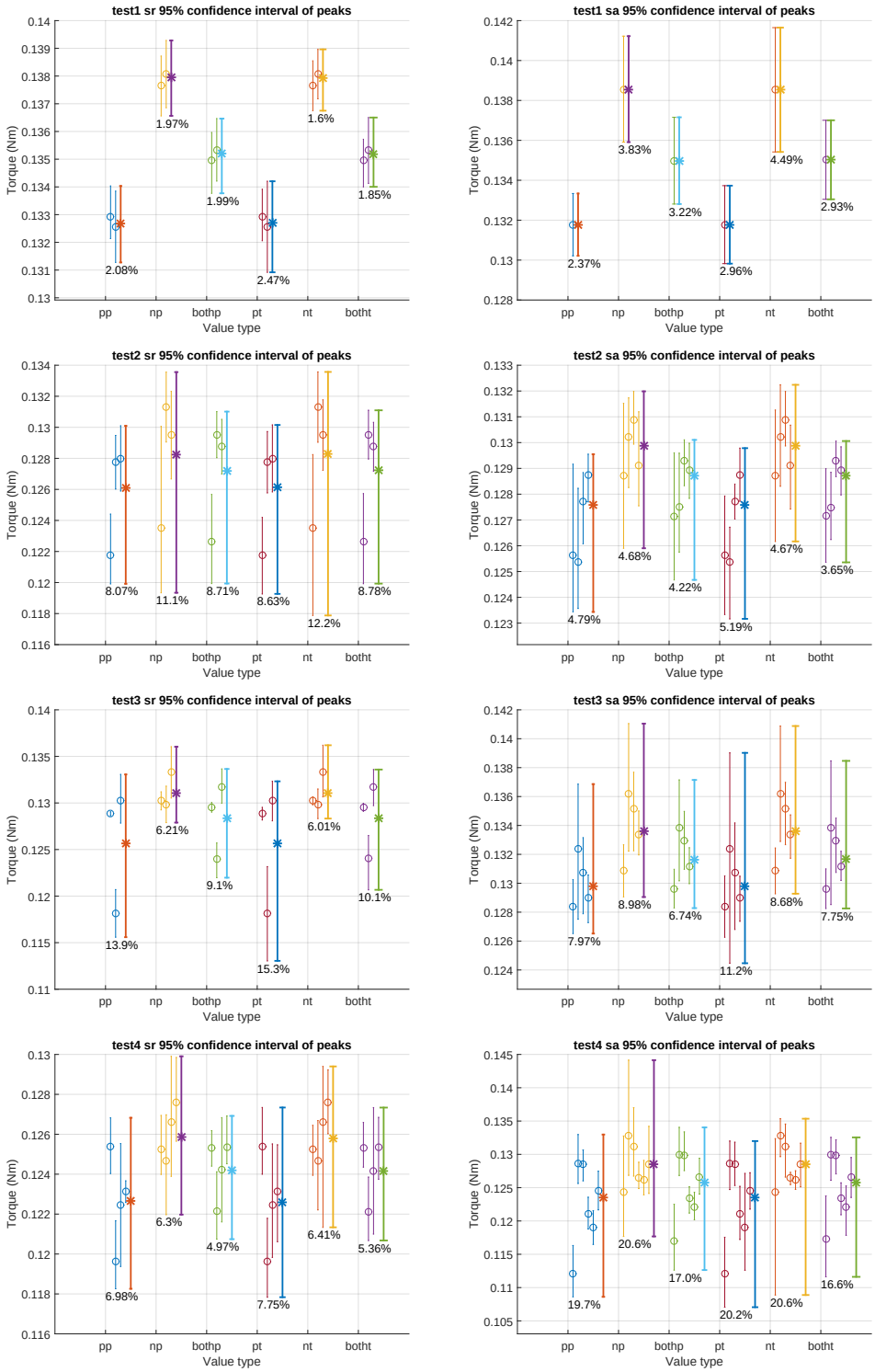

Figure 67: 95 % confidence interval of the mean for small designs. The number in the graph shows the percentage difference between the highest and smallest bound of the Confidence intervals. Middle dot or star is the mean of the data.

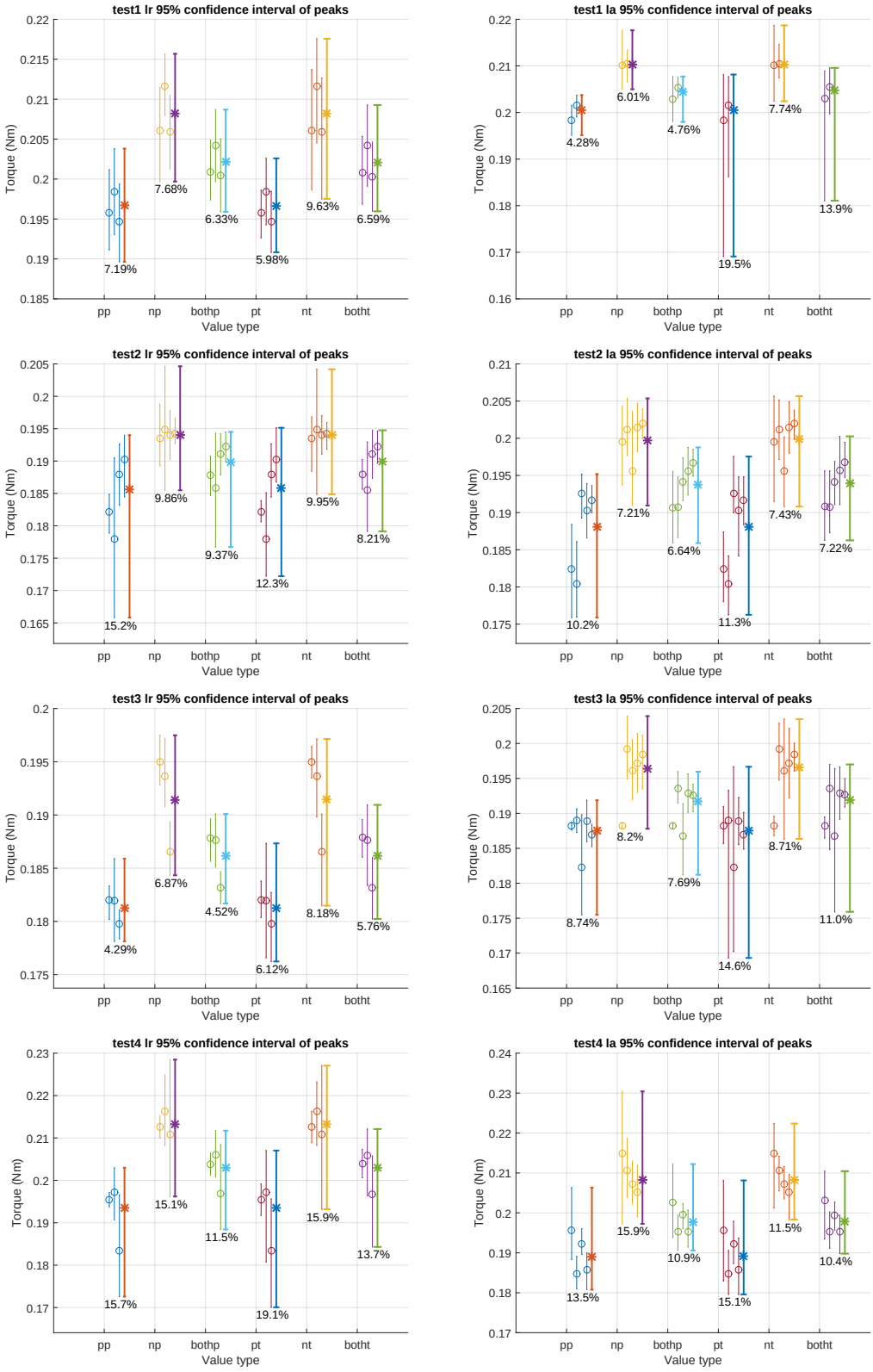

Figure 68: 95 % confidence interval of the mean for large designs. The number in the graph shows the percentage difference between the highest and smallest bound of the Confidence intervals. Middle dot or star is the mean of the data.

References

[1] M A Ahad and S M Ahmad. Study of non-contact power transmission mechanism for unmanned underwater vehicle applications. In *Proceedings of 2016 13th International Bhurban Conference on Applied Sciences and Technology, IBCAST 2016*, pages 541–546, 2016. ISBN 9781467391276. doi: 10.1109/IBCAST.2016.7429931. URL https://ieeexplore.ieee.org/document/7429931.

[2] Rahul Bale, Izaak D Neveln, Amneet Pal Singh Bhalla, Malcolm A MacIver, and Neelesh A Patankar. Convergent Evolution of Mechanically Optimal Locomotion in Aquatic Invertebrates and Vertebrates. *PLoS biology*, 13(4):e1002123, 2015. ISSN 1545-7885. doi: 10.1371/journal.pbio.1002123. URL http://journals.plos.org/plosbiology/article?id=10.1371/journal.pbio.1002123.

[3] Jean-frederic Charpentier and Guy Lemarquand. A study of Permanent magnet couplings with Progressive magnetization using analytical exact formulation. *IEEE Transactions on Magnetics, Institute of Electrical and Electronics Engineers*, 35(5):4206–4217, 1999. URL https://ieeexplore.ieee.org/abstract/document/799069.

[4] Jianning Dong. Interview, Februari 2017. Faculty of Electrical Engineering, Mathematics & Computer Science, Delft University of Technology.

[5] I. R. Harris and G. W. Jewell. Rare-earth magnets: Properties, processing and applications. *Functional Materials for Sustainable Energy Applications*, pages 600–639, 2012. ISSN 2044-9364. doi: 10.1533/9780857096371.4.600. URL https://www.sciencedirect.com/science/article/pii/B9780857090591500191.

[6] *Haveninfrastructuur*. Havenbedrijf Rotterdam, . URL https://www.portofrotterdam.com/nl/de-haven/haven-feiten-en-cijfers/haveninfrastructuur. Accessed: 12-06-2018.

[7] *Het havengebied*. Havenbedrijf Rotterdam, . URL https://jaarverslag2017.portofrotterdam.com/haven-en-havenbedrijf-rotterdam/over-de-haven-van-rotterdam/het-havengebied. Accessed: 12-06-2018.

[8] F. S. Hover, O. Haugsdal, and M. S. Triantafyllou. Effect of angle of attack profiles in flapping foil propulsion. *Journal of Fluids and Structures*, 19(1):37–47, 2004. ISSN 08899746. doi: 10.1016/j.jfluidstructs.2003.10.003. URL https://www.sciencedirect.com/science/article/pii/S0889974603001749.

[9] Linni Jian, Student Member, K T Chau, and Senior Member. A Coaxial Magnetic Gear With Halbach Permanent-Magnet Arrays. *IEEE Transactions on Energy Conversion*, 25(2):319–328, 2010. URL https://hub.hku.hk/handle/10722/129185.

[10] Matthew Joordens and Benjamin Champion. Underwater swarm robotics: Challenges and opportunities. In *Handbook of Research on Design, Control, and Modeling of Swarm Robotics*, pages 718–740. IGI Global, 2016.

[11] Byoung Hun Kang, John Ting-yung Wen, Nicholas G Dagalakis, and Jason J Gorman. Analysis and Design of Parallel MechanismsWith Flexure Joints. *IEEE Transactions on Robotics*, 21(6):1179–1185, 2005. URL https://ieeexplore.ieee.org/abstract/document/1549944/.

[12] R.K. Katzschmann, A. De Maille, D.L. Dorhout, and D. Rus. Cyclic hydraulic actuation for soft robotic devices. *IEEE International Conference on Intelligent Robots and Systems*, 9(14):3048–3055, 2016. ISSN 21530866. doi: 10.1109/IROS.2016.7759472. URL https://ieeexplore.ieee.org/abstract/document/7759472.

[13] Terry K. Koo and Mae Y. Li. A Guideline of Selecting and Reporting Intraclass Correlation Coefficients for Reliability Research. *Journal of Chiropractic Medicine*, 15(2):155–163, 2016. ISSN 15563707. doi: 10.1016/j.jcm.2016.02.012. URL http://dx.doi.org/10.1016/j.jcm.2016.02.012.

[14] Michael Krieg and Kamran Mohseni. Thrust characterization of a bioinspired vortex ring thruster for locomotion of underwater robots. *IEEE Journal of Oceanic Engineering*, 33(2):123–132, 2008. ISSN 03649059. doi: 10.1109/JOE.2008.920171. URL https://ieeexplore.ieee.org/abstract/document/4623834.

[15] Steven Kuipers. Actuator choice for long-term autonomous bio-inspired swimming robots: Review, 2018. Available upon request through stevenkuipers@hotmail.com.

[16] CC Lindsey. Form, function, and locomotory habits in fish. *Fish physiology*, 7(Locomotion), 1979.

[17] R.D. Lorenz, L.P. Haines, Wisconsin Electric Machines, and Power Electronic Consortium. *Understanding Modern Power Conversion: Robert D. Lorenz and Lance P. Haines*. 2000. URL https://books.google.nl/books?id=HYfSGwAACAAJ.

[18] D Farhadi Machekposhti, N Tolou, and J L Herder. A Review on Compliant Joints and Rigid-Body Constant Velocity Universal Joints Toward the Design of Compliant Homokinetic Couplings. *Journal of Mechanical Design*, 137(March 2015):1–12, 2015. doi: 10.1115/1.4029318. URL http://mechanicaldesign.asmedigitalcollection.asme.org/article.aspx?articleid=2022464.

[19] *RE-max 24 mm, Graphite Brushes, 11 Watt*. Maxon Motors, . URL https://www.maxonmotor.com/maxon/view/product/motor/dcmotor/remax/remax24/222053?etcc_cu=onsite&etcc_med=Header%20Suche&etcc_cmp=mit%20Ergebnis&etcc_ctv=Layer&query=222053. Accessed: 22-07-2017.

[20] *Planetary Gearhead GP 22 mm, 0.5 - 2.0 Nm*. Maxon Motors, . URL https://www.maxonmotor.com/maxon/view/product/gear/planetary/gp22/143980?etcc_cu=onsite&etcc_med=Header%20Suche&etcc_cmp=mit%20Ergebnis&etcc_ctv=Layer&query=143980. Accessed: 22-07-2017.

[21] GA McCoy. Premium efficiency motor selection and application guide - A handbook for industry. *U.S. Department of Energy - Energ*, pages 10–15, 2014. URL https://www.osti.gov/scitech/biblio/1220835.

[22] Bobak Mosadegh, Panagiotis Polygerinos, Christoph Keplinger, Sophia Wennstedt, Robert F Shepherd, Unmukt Gupta, Jongmin Shim, Katia Bertoldi, Conor J Walsh, and George M Whitesides. Pneumatic networks for soft robotics that actuate rapidly. *Advanced Functional Materials*, 24(15):2163–2170, 2014. ISSN 16163028. doi: 10.1002/adfm.201303288. URL https://onlinelibrary.wiley.com/doi/abs/10.1002/adfm.201303288.

[23] M Muschenbroek. Of Magnetical Powers. *The Philosophical Transactions Of The Royal Society of London*, Vol VII:105–109, 1809. URL https://books.google.nl/books?id=Tz9KAAAAYAAJ.

[24] Yoshinobu Nakamura, Motoyasu Mochizuki, and Fuminori Ishibashi. Brushless dc Motor with Large Air Gap. *Electrical Engineering in Japan*, 125(3):67–74, 1998. URL https://onlinelibrary.wiley.com/doi/abs/10.1002/(SICI)1520-6416(19981130)125:3{%}3C67::AID-EEJ8{%}3E3.0.CO;2-{%}23.

[25] Galatea Project. Galatea. URL http://www.galatea-project.nl/. Accessed: 01-02-2018.

[26] R Rabinovici. Eddy current losses of permanent magnet motors. *IEE Proceedings-Electric Power Applications*, 141(1):7–11, 1994. URL https://digital-library.theiet.org/content/journals/10.1049/ip-epa{_}19949775.

[27] T. Ranzani, G. Gerboni, M. Cianchetti, and A. Menciassi. A bioinspired soft manipulator for minimally invasive surgery. *Bioinspiration and Biomimetics*, 10(3), 2015. ISSN 17483190. doi: 10.1088/1748-3190/10/3/035008. URL https://iopscience.iop.org/article/10.1088/1748-3190/10/3/035008/meta.

[28] Erol Sahin. Swarm Robotics: From Source to Inspiration to Domains of Application. *Special Issue, Autonomous Robots*, 3342:10–20, 2005. ISSN 0302-9743. doi: 10.1007/b105069. URL http://citeseerx.ist.psu.edu/viewdoc/summary?doi=10.1.1.161.6393{%}5Cnhttp://link.springer.com/10.1007/b105069.

[29] Arash Salarian. Intraclass correlation coefficient (icc), 2008. URL https://nl.mathworks.com/matlabcentral/fileexchange/22099-intraclass-correlation-coefficient-icc. Accessed: 13-09-2018.

[30] Lionel Schouveiler, F. S. Hover, and M. S. Triantafyllou. Performance of flapping foil propulsion. *Journal of Fluids and Structures*, 20(7 SPEC. ISS.):949–959, 2005. ISSN 08899746. doi: 10.1016/j.jfluidstructs.2005.05.009. URL http://www.sciencedirect.com/science/article/pii/S0889974605000770.

[31] Michael Sfakiotakis, Asimina Kazakidi, Avgousta Chatzidaki, Theodoros Evdaimon, and Dimitris P. Tsakiris. Multi-arm robotic swimming with octopus-inspired compliant web. *IEEE International Conference on Intelligent Robots and Systems*, (Iros):302–308, 2014. ISSN 21530866. doi: 10.1109/IROS.2014.6942576.

[32] Debarupa Som, Kang Li, Joshua Kadel, Jason Wright, Sina Modaresahmadi, Jonathan Z. Bird, and W. William. Analysis and Testing of a Coaxial Magnetic Gearbox with Flux Concentration Halbach Rotors. *IEEE Transactions on Magnetics*, 53(11), 2017. ISSN 00189464. doi: 10.1109/TMAG.2017.2715799. URL https://ieeexplore.ieee.org/abstract/document/7949068.

[33] Michelle D. Staudinger, Roger T. Hanlon, and Francis Juanes. Primary and secondary defences of squid to cruising and ambush fish predators: Variable tactics and their survival value. *Animal Behaviour*, 81(3):585–594, 2011. ISSN 00033472. doi: 10.1016/j.anbehav.2010.12.002. URL http://dx.doi.org/10.1016/j.anbehav.2010.12.002.

[34] *Technical Specifications*. supermagnete.nl. URL https://www.supermagnete.nl/data_sheet_W-04-N.pdf. Accessed: 18-05-2017.

[35] *Neodymium-Iron-Boron Magnets*. TDK. URL https://www.tdk.co.jp/tefe02/e331.pdf. Accessed: 16-01-2018.

[36] Teapeat. Field lines around a halbach array. URL https://commons.wikimedia.org/wiki/File:Halbach_array_field.jpg. Accessed: 14-12-2018.

[37] Brian P Trease, Yong-Mo Moon, and Sridhar Kota. Design of Large-Displacement Compliant Joints. *Journal of Mechanical Design*, 127(4):788, 2005. ISSN 10500472. doi: 10.1115/1.1900149. URL http://mechanicaldesign.asmedigitalcollection.asme.org/article.aspx?articleid=1448601.

[38] David L Trumper, Mark E Williams, and Tiep H Nguyen. Magnet Arrays for Synchronous Machines. *Electrical Engineering*, pages 9–18, 1993. ISSN 01608592. doi: 10.1109/IAS.1993.298897. URL https://ieeexplore.ieee.org/abstract/document/298897/.

[39] *Technical Specifications*. Vacuum Schmelze. URL https://www.vacuumschmelze.com/en/products/materials-parts/soft-magnetic/cobalt-iron/vacoflux/vacoflux-physical-properties.html. Accessed: 09-02-2019.

[40] Tim Vercruyssen. Email conversation, September 2018.

[41] Alex Villanueva, Colin Smith, and Shashank Priya. A biomimetic robotic jellyfish (Robojelly) actuated by shape memory alloy composite actuators. *Bioinspiration and Biomimetics*, 6(3), 2011. ISSN 17483182. doi: 10.1088/1748-3182/6/3/036004. URL https://iopscience.iop.org/article/10.1088/1748-3182/6/3/036004/meta.

[42] Z.Q. Zhu and D. Howe. Halbach permanent magnet machines and applications: a review. *IEE Proceedings - Electric Power Applications*, 148(4):299, 2001. ISSN 13502352. doi: 10.1049/ip-epa:20010479. URL https://digital-library.theiet.org/content/journals/10.1049/ip-epa{_}20010479.